University of Zurich[UZH]

Multi-sensor observations for snow cover detection and vegetation onset in the Swiss Alps

GEO 511 Master's Thesis

Author
Andrea Rebba
16-918-989

Supervised by
Dr. Claudia Röösli
Flurina Schnider (flurina.schnider@geoformer.ch)

Faculty representative
Prof. Dr. Alexander Damm

30.01.2024
Department of Geography, University of Zurich

Abstract

Despite the decrease of their occurrence caused by global warming, avalanches remain a main component of Alpine environment, resulting in the necessity for protection and prevention strategies. The characterization of snow cover extent and melt patterns is a crucial part of avalanche protection, both in the case of artificial solutions, such as snow nets, and natural ones, as for instance trees. Currently, snow presence is mainly assessed using the Normalized Difference Snow Index (NDSI), which is tied to a low spatial resolution, not suited for smaller, more complex areas. This Thesis covers the use of high-resolution Normalized Difference Vegetation Index (NDVI) time series to determine Phenology metrics and use them as a mean to estimate melt-out timing. The performance of snow cover and melt maps is also tested for products based solely on NDVI and on RGB/Multispectral drones. The chosen sensors for the research are Sentinel-2 and PlanetScope SuperDove. All the results are then compared to each other to determine the advantages and disadvantages of each method.

It is found that both the Start of Season maps calculated in the phenology analysis and the NDVI maps highlighted the same areas as early and late melting, with the former producing more accurate, continuous results, which better relate to topography. This is especially visible when using SuperDove, which, contrarily to Sentinel-2 can better characterize small scale snow dynamics. Both the satellite NDVI and RGB drone snow melt maps showed a high dependency on the availability of images, resulting in imprecise melt-out day estimations.

In the case of the Phenology based approach, the advantages identified are the precision of estimates, large area coverage, continuous values of the estimates and not being influenced by missing images, while the disadvantages are the high number of images needed and the longer data preparation and processing. The advantages of the NDVI method rely on the low number of required images and workflow simplicity, while the drawbacks are tied to more inaccurate estimations and susceptibility to missing images. Similarly, the RGB drone maps showed a low accuracy considering the extremely high spatial resolution, while also being subject to the same disadvantages of the NDVI melt map, with the addition of the need to travel to the study area.

It is concluded that the choice of method should reflect the scope of the analysis, as the advantages and disadvantages can be enhanced or mitigated depending on the objective and study area.

Acknowledgments

Sincere thanks to my supervisor Dr. Claudia Röösli for guiding me throughout the whole Thesis and for always providing constructive feedback, encouraging critical thinking and for supporting me during the difficult parts of the research.

I would also like to extend my thanks to Flurina Schnider and the people at Geoformer for their assistance during the field days and for granting me access to their data.

Table of Contents

Abbreviations

AOI:	Area of Interest
APEX:	Airborne Prism Experiment
CL:	Confidence Level
CWL:	Central Wavelength
DN:	Digital Number
DOY:	Day of the year
DSM:	Digital Surface Model
DTM:	Digital Terrain Model
GCP:	Ground Control Point
GNSS:	Global Navigation Satellite System
GSD:	Ground Sampling Distance
Ha:	Hectare
InSAR:	Interferometric SAR
L8:	Landsat-8
L9:	Landsat-9
LSP:	Land Surface Phenology
LWIR:	Long-wave Infrared
m.a.s.l.:	meters above sea level
NA:	Not Applicable
NDSI:	Normalized Difference Snow Index
NDVI:	Normalized Difference Vegetation Index
NIR:	Near Infra-Red
OLI:	Operational Land Imager
PolSAR:	Polarimetric SAR
PPK:	Post-processing Kinematic
PSB.SD:	PlanetScope SuperDove
QA:	Quality Assurance
RE:	Red-Edge
RGB:	Red Green Blue
RTK:	Real Time Kinematic
S2:	Sentinel-2
SAR:	Synthetic Aperture Radar

SCL:	Scene Classification Layer
Sen2Cor:	Sentinel-2 atmospheric correction
SNR:	Signal-to-noise ratio
SWIR:	Shortwave Infrared
TOA:	Top of Atmosphere
UAV:	Unmanned Aerial Vehicle
UDM:	Usable Data Mask
VI:	Vegetation Index
VIS:	Visible

1. Introduction

Although the worldwide shrinking of the cryosphere and the relative decrease in both snowfall and avalanches occurrence (Giacona et al., 2021), the latter still represent a major natural threat in the Swiss Alps region (Hervás, 2003). It is therefore crucial to have a well-developed system for avalanche prevention, which usually takes the form of man-made structures such as snow nets or more natural approaches as for instance trees (Teich et al., 2014). Contrarily to snow nets however, trees are not immediately ready and require time to develop enough to represent a protection strategy. In the meantime, they are characterized by a high mortality rate mainly tied to wind-blown snow (Jones, 1999), especially in the earlier stages of their life cycle (Van Valen, 1975). The spatial patterns of tree mortality have been proven to be highly correlated with the date of snow disappearance (Barbeito et al., 2012), meaning that an early snow melt usually corresponds to a higher survival rate of trees, and therefore that the areas where snow melts first are optimal for planting trees which will serve for avalanche protection.

Currently, melt dynamics are characterized using the Normalized Difference Snow Index (NDSI), based on the Green and Shortwave Infrared (SWIR) wavelengths (Wang et al., 2022), or with Synthetic Aperture Radars (SAR), which exploit the interaction between the snowpack and microwaves (Tsai et al., 2019). However, in the case of publicly available satellite data, NDSI is limited by the low spatial resolution of the SWIR channel (Vaiopoulos and Karantzalos, 2016), while, in the case of Sentinel-1, SAR data is delivered with a low temporal and spatial resolution (Inglada et al., 2016). This results in both methods not being particularly suited for high resolution snow melt and vegetation dynamics assessment in high alpine regions.

This Thesis seeks to explore the use of phenology metrics as a potential mean to estimate the melting patterns of snow in a high alpine environment. This will be done using high (10m) and very high (3m) spatial resolution imagery provided by Sentinel-2 and SuperDove.

The snow cover extent and melt dynamics will also be assessed using NDVI from the two previously mentioned satellites, testing if the vegetation index can represent a substitute for NDSI when the SWIR band is not available or when its low spatial resolution is not suited for the size or complexity of the study area.

A snow depth map will also be derived from the difference between two DSMs, one snow covered, the other snow free, generated from the images captured with a multispectral UAV. In addition, there will be an assessment of the accuracy of snow melt maps created using a drone operating in the visible spectrum.

Finally, the performance of each method and sensor will be assessed, with the goal of answering the following questions:

- How do multi-year satellite-based melt-out timing estimations perform compared to ground-based observations?
- What are the advantages and disadvantages of different remote sensing methods (Satellite images, optical and multispectral UAVs) to detect early spring vegetation season start and snow melt in a high alpine region in terms of both applicability and reliability?

2. Research background

2.1. Land Surface Phenology and snow cover assessment

Different remote sensing techniques have been used since the 1960s to produce snow cover maps at a high temporal and spatial resolution (Dietz et al., 2012). The first, widely used method for snow detection and characterization is the Normalized Difference Snow Index (NDSI), which is based on the reflectance properties of snow in the green and short-wave infrared (SWIR) wavelengths (Hall and Riggs, 2011). However, the spatial resolution of the SWIR band for Sentinel, Landsat, and MODIS, i.e., satellites which provide free images access, is 20, 30 and 500m respectively (Notti et al., 2018), meaning that the reflectance features associated to the smaller elements of the study area will not be properly detected (Woodcock and Strahler, 1987).

Another approach to estimating snow cover extent is the use of synthetic aperture radars (SAR), which provide the advantage of acquiring images independently from illumination and cloud cover, both limiting factors in the case of optical-based sensors (Tsai et al., 2019). The use of classical SAR however, is limited by the ability to only detect wet snow cover, and the proposed machine learning technique to combine it with dry-snow-sensitive InSAR and PolSAR data (Tsai et al., 2019) would result in a deviation from the scope of the thesis. Therefore, at the moment it is difficult to find a high spatial and temporal resolution, low-cost remote sensing technique to characterize snow cover and its relative melting (Awasthi and Varade, 2021).

A possible solution can be found based on the relationship between vegetation and snow cover, which is characterized by inactivity in winter under snow (Kappen, 1993). In cold, high latitude areas the day of vegetation activation coincides with the last day of snow cover (Zeng and Jia, 2013), meaning that by knowing the moment at which vegetation starts growing, i.e., the start of the season (Qi et al., 2021), it is possible to determine the first snow free days of the year.

Vegetation phenology is the study of periodic events in plant cycle, namely dormancy, active growth, and senescence and it consists of three parameters: the previously mentioned start of growing season (SOS), the end of growing season (EOS) and the length of growing season (LOS) (Qi et al., 2021). The estimation of these metrics usually happens through a curve fitting of an NDVI time series using a chosen function, followed by the identification of critical thresholds which will define where SOS and the other parameters are located (Wang et al., 2014). The most recognized method for fitting a time series and creating a daily NDVI curve is the double logistic regression, as it can effectively characterize the plateaus in NDVI values corresponding to the extended photosynthesis peak period, and the ones related to the dormancy phase in the first and last months of the year (Julien and Sobrino, 2009). The phenological metrics are then extracted from the fitted curve. The most popular technique is the midpoint method, which sets SOS and EOS at the points where the NDVI is equal to half of the amplitude of the fitted NDVI time series (Qiao et al., 2021). This method however tends to overestimate the Start of Season (Ren et al., 2017), which results in being suboptimal for estimating a SOS as close as possible to the last day of snow cover. To this matter, the use of the third derivate of the fitted NDVI time series has been recognized as being able to extract the phenological metrics more precisely (Busetto et al., 2010), as it sets the Start of Season slightly before the spike in the fitted curve, which is associated to an

increase in plant activity. Due to the relationship between snow melt and vegetation onset (Revuelto et al., 2022), the calculated SOS can be considered in concurrence with the last day of snow cover.

2.2. NDVI for snow cover detection

NDVI has also been used as a source of complementary information to NDSI-based snow cover mapping (Bashir and Rasul, 2010), or as a component in the analysis of the relationship between phenology and snow cover (Asam et al., 2018).

The negative correlation between winter NDVI values and snow cover extent (Kaufmann et al., 2003) serves as a theoretical base for the creation of snow cover maps.

2.3. Snow depth map

Similarly to the estimation of snow cover, the assessment of snow depth through remote sensing is usually performed using a few, well-established techniques. A LiDAR (Light Detection and Ranging) is used to create a point cloud of the study area, from which a Digital Terrain Model (DTM) and Digital Surface Model (DSM) can be extracted (Yunfei et al., 2008). Then, snow depth is calculated by subtracting a DTM of a snow-free area from DSM of a snow-covered one (Deems et al., 2013). Another method relies on microwave radiometry (Che et al., 2008), and more specifically on the different radiation of snowpack and terrain measured at various frequencies (Kern and Ozsoy-Çiçek, 2016).

The use of small, easily accessible UAVs for the estimation of snow depth is based on the difference between DSMs (Harder et al., 2016), which are created through photogrammetry and successive generation of a georeferenced point cloud (Lendzioch et al., 2019).

3. Study Area and climate

The study area is known as “Chalberweid” and is located on the Simplonpass, in Canton Valais. The zone spans from a minimum elevation of 1’950 meters above sea level (m.a.s.l.) to a maximum of 2’060 m.a.s.l., covering a surface of about 3’870 m^2.

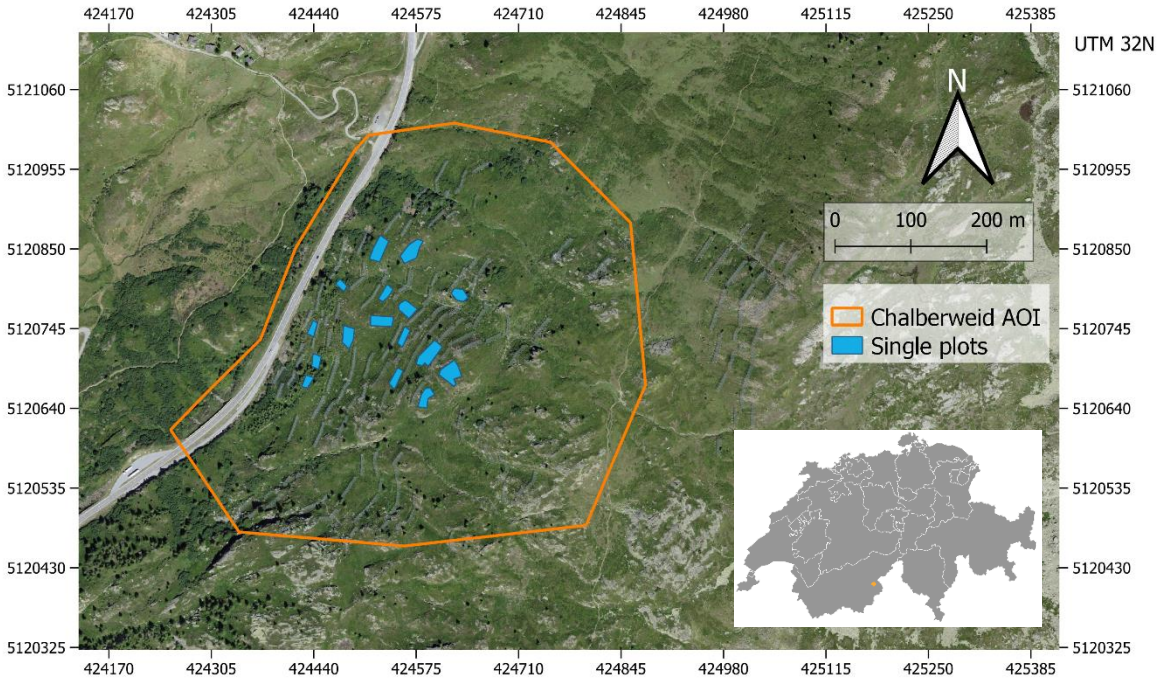

Figure 1: Location of the Chalberweid study area. The main region of interest is highlighted in orange while the light blue polygons indicate the single plots where the survival rate of tress is assessed.

The area includes different structures for avalanche protection such as metal nets and “Dreibeinböcke”, i.e., tripods made of wood which reduce snow gliding. The area covered by both the satellite images and the drone flight is larger than the one visible in Figure 1.

Since 2014, the Chalberweid area has been theater of the reforestation project “Aufforstung Chalberweid”, mandated by the “Bundesamt für Strassen ASTRA” and carried out by “Geoformer igp AG”, an engineering studio based in Brig. The goal of the project is to monitor snow melting and tree survival rate over winter. Therefore, inside the area of interest (see orange polygon in Figure 1) there are 16 smaller plots which are the focus of the reforestation started in 2014 with Swiss pines (*pinus cembra*) and Larches (*larix*).

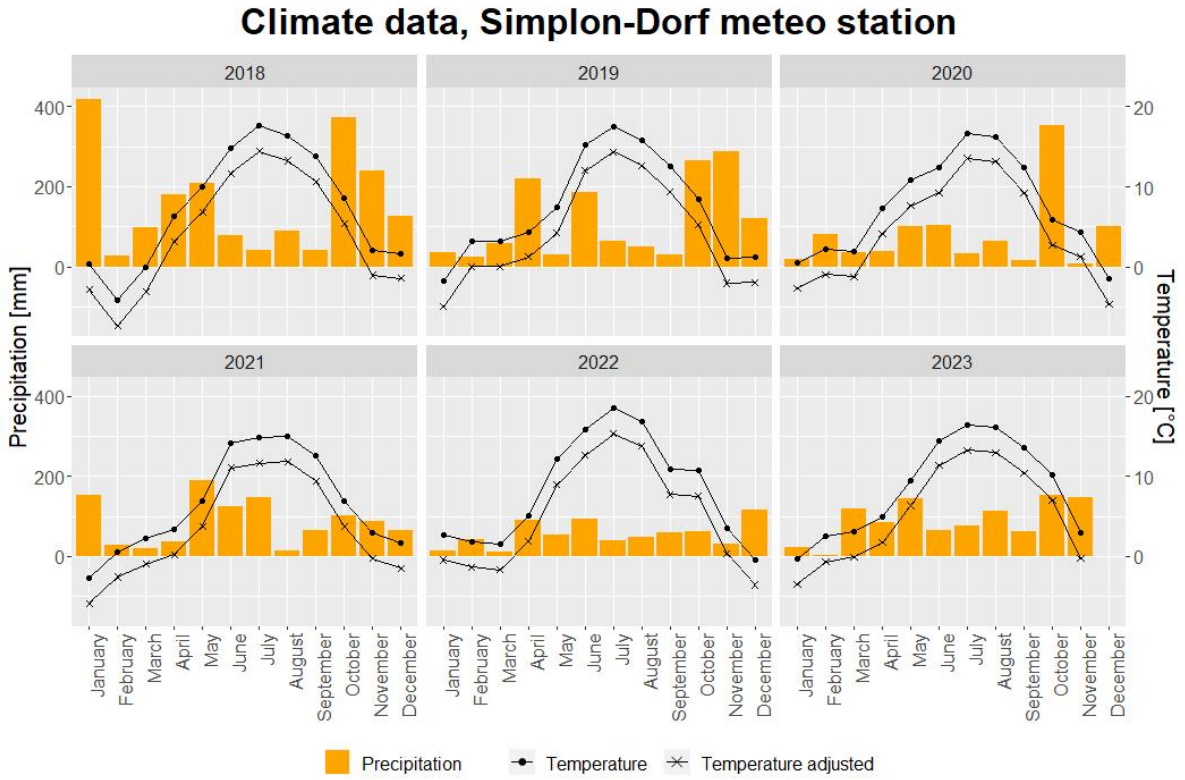

Figure 2: Temperature and Precipitation data measured by the Simplon-Dorf weather station from the year 2018 to 2023. The line with cross points is the calculated adjusted temperature for the Chalberweid area.

Figure 2 shows the plots of temperature and precipitation for the years 2018 to 2023, registered by the weather station Simplon-Dorf (1465 m.a.s.l.), located 5 km south of Chalberweid. As the center of the study area is located at an altitude of 1990 m.a.s.l. and the weather data is not available for that location, the temperature has calculated based on the height difference using a gradient of 0.6°C/100m. Therefore, the adjusted temperature for the Chalberweid is on average 3.15°C lower than the one registered by the Simplon-Dorf station. Calculating the adjusted temperatures allows the estimation of snowfall, which was determined to be taking place starting from 2°C.

The temperature line follows a similar pattern every year, i.e., lower values in the first three months of the year, a steady increase until June, a peak in July (2021 is the only year where the peak is in August) and finally a steady decrease until November/December. It must be noted that during the Winters between 2019-2020 and 2021-2022 the mean monthly temperature measured by the weather station did not reach negative values, contrarily to what happened in all the other cases. At the Chalberweid altitude the calculated winter temperatures were always under 0°C, still, during the winters mentioned above they were visibly higher than for the other years.

The lowest average temperature was registered in February 2018, with -4.2°C (-7.35°C adjusted) while the highest temperature was reached in July 2022 with 18.5°C (15.35°C).

Precipitation on the other hand, does not follow any particular pattern. The highest amount of precipitation was measured during January 2018, with 419.1 mm, while the lowest one in February 2023 with only 2.8 mm.

In yearly terms, 2018 was the wettest one, with a total of 1920.4 mm deposited, while 2022 was the driest one, with just 657.2 mm. Based on the temperature estimates and precipitation measurements, snow deposits were more prominent during the winters between 2017-2018 (due to the amount of precipitation during January 2018), 2018-2019 and 2019-2020. The high temperatures and low precipitation which characterized both the winters 2021-2022 and 2022-2023 likely led to reduced snow deposits.

4. The Geoformer project

As mentioned before, the project is mandated by the "Bundesamt für Strassen ASTRA" and has the goal of analyzing plant activity and survivability to be able to gain the knowledge necessary for planning future high-altitude afforestation projects. It has a planned duration of 10 years (2014-2024) and focuses on creating high resolution snow cover and snow melt maps, as well as a yearly assessment of the number of planted trees which survived the winter.

While the survival rate is checked directly on site, the method of choice for creating the different snow maps is the use of the DJI Phantom 4, a UAV with a camera operating in the visible spectrum. The exact methodology used is covered in the next chapter.

The interest of Geoformer for this Thesis is to determine whether there are advantages in using other remote sensing techniques for characterizing snow cover dynamics, especially the Planet products and the use of a drone with an added Infrared band instead of just an optical one.

4.1. Creation of snow cover maps

The eventual presence of snow is determined by the reflectance values of the single pixels of a drone generated RGB image, which is a number included between 0 and 255 (Digital Number). Whether snow is still covering an area or not is established by a threshold value, indicated by the blue line in Figure 3. However, since the threshold value for snow categorization is not predetermined but varies with each field survey, there is a strong potential for misclassification. This is visible when observing Figure 3, which shows the snow cover in two of the sixteen subplots on April 15th, 2022 (two images on the left) and on April 22nd, 2022 (on the right).

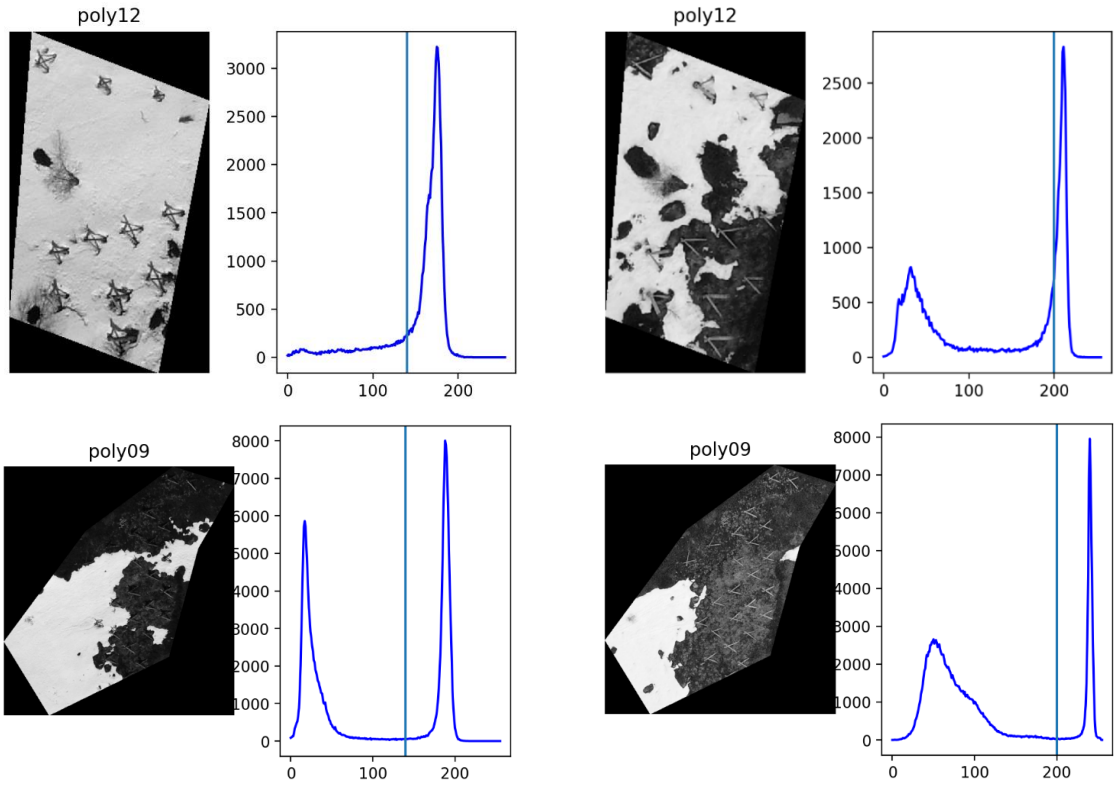

Figure 3 from top left to bottom right: image and relative histogram of polygon 12 during the flight of April 15th, image and histogram for polygon 12 on April 22nd, polygon 09 on April 15th, polygon 09 on April 22nd.

The chosen DN associated with snow must be constant within every field day, this value however can vary between surveys depending on the different time of year or climate conditions, which ultimately influence surface reflectance. For example, during the flight of April 15th, the value for snow identification was set at 139, while on April 22nd, the threshold was at 200.

However, the chosen threshold can perform accurately in one area and at the same time misclassify another. This mainly happens where the reflectance histogram displays a longer growing phase rather than an abrupt spike. This effect can be seen in the images above. If the area has clear, distinguishable features (e.g., lower right, poly09), then bright pixels will be easily identifiable in the histogram, resulting in an accurate classification. If, however, the different elements are less identifiable, then the selected threshold will inevitably lead to misclassification, as it is often the case with shadows and other low reflecting features (e.g., upper right, poly12. Here the threshold value is set where the frequency of bright pixels has already started increasing, thus classifying some snow pixels as "not-snow").

Figure 4 shows three single day snow cover maps created using the RGB approach. For each field day a snow cover map is created, indicating where snow can be found (represented by a 1, white) and where it has already melted (0, black). In 2022, 8 surveys have been conducted, the first the 24th of March and the last the 14th of May.

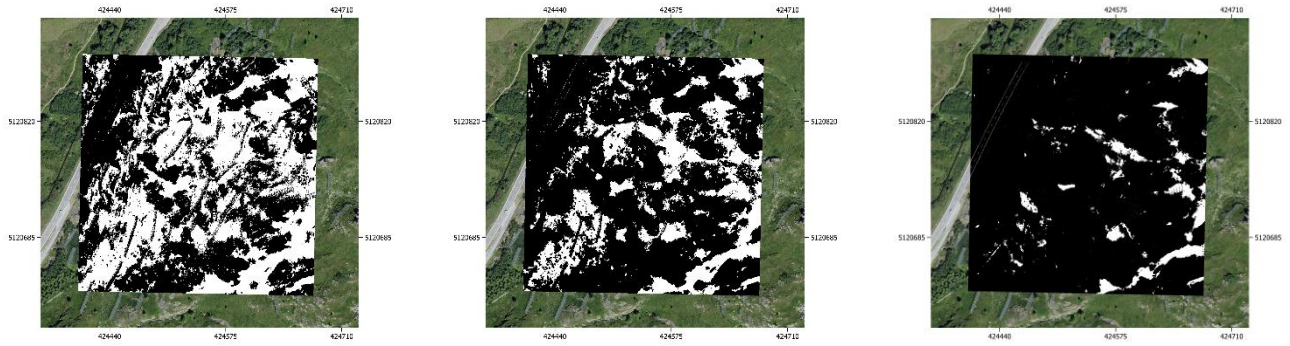

Figure 4, from left to right: optical-drone-derived single day snow cover maps of April 15th, April 22nd, and May 9th. The white pixels represent snow cover at the moment of the survey while black ones are associated to every other "not-snow" feature.

By combining the extent of snow cover measured during the different field days it is possible to create a map displaying the moment at which snow is no longer present. Therefore, all the binary maps are summed, and the final image displays the snow's melting patterns (Figure 5). Each pixel in the image is associated to a number and a corresponding shade of grey associated with snow cover, going from black (number 0) representing snow-free surfaces on the first field day, to white (highest number) indicating snow cover still present at the moment of the last survey. For the analysis, the values of the snowmelt map were converted to day of the year (doy), so that they could be compared to the other methods.

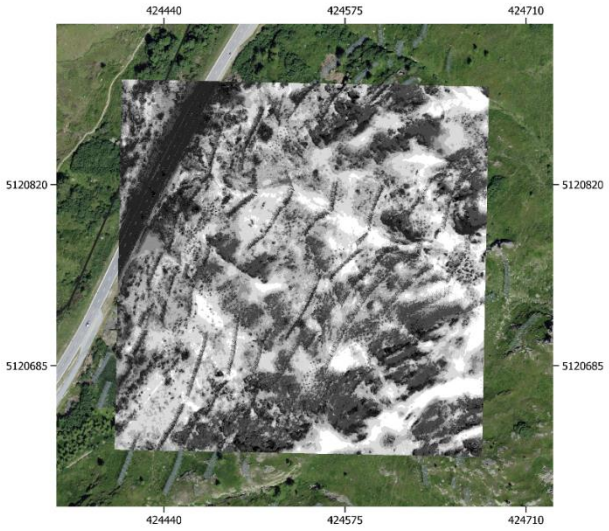

Figure 5: Map displaying the pattern of snowmelt for the year 2022 created using the optical drone. Darker colors represent an early melt while with areas are associated with a late one.

5. Platforms

5.1. Satellites

The chosen satellites for this Thesis are Landsat 8, Landsat 9, Sentinel 2, and PlanetScope SuperDove. The first three were selected because of their image accessibility, medium spatial resolution and medium-high temporal resolution when paired together. The Planet product was chosen to compare its higher spatial and temporal resolution to the ones of other satellites. The analysis should lead to determining how Planet data compares to Sentinel and Landsat and whether it can be a valid substitute or not.

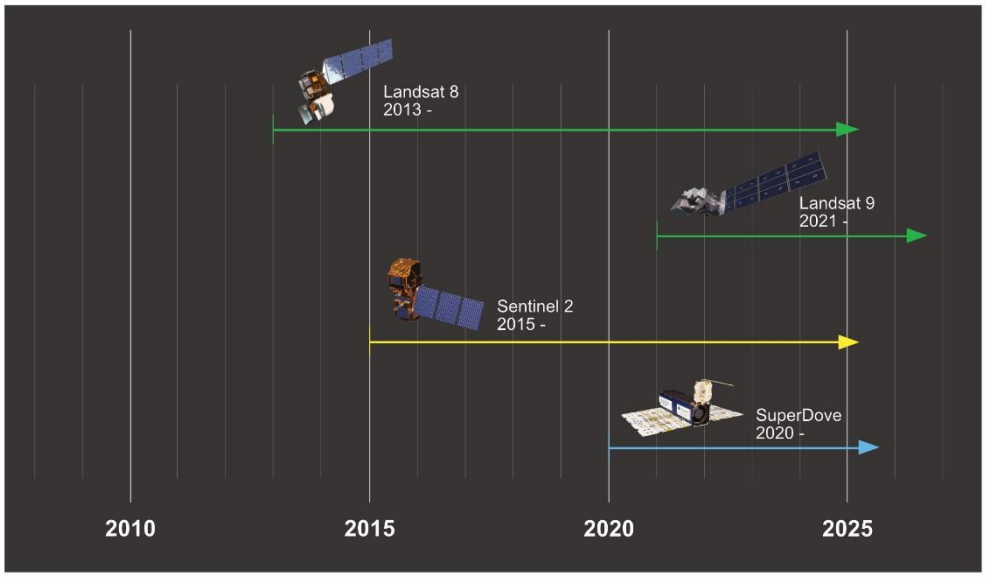

Figure 6: Launch date of Landsat-8, Landsat-9, Sentinel-2 and SuperDove.

Table 1 summarizes the main characteristics of each one of the chosen sensors, illustrating the launch date, the spatial resolution, the temporal resolution, and the number of the available bands. Each sensor is described more in depth in the following four sub-chapters.

Table 1: List of Launch date, available bands, temporal and spatial resolution of Sentinel-2, Landsat-8/9 and SuperDove.

	Sentinel 2	**Landsat 8**	**Landsat 9**	**SuperDove**
Launch	June 2015	February 2013	September 2021	March 2020
Spatial Resolution	10m (20m / 60m)	30m (15m / 100m)	30m (15m / 100m)	3m
Temporal Resolution	2-3 days (S2A + S2B)	16 days	16 days	daily
Bands	13	9 + 2	9 + 2	8

5.1.1. Sentinel-2

Sentinel-2 was launched in June of 2015 with the primary objective of providing high resolution satellite images for land cover monitoring while complementing other missions such as Landsat (Phiri et al., 2020). Its bands can be divided into three categories depending on their spatial resolution: Blue, Green, Red and Near Infrared (NIR) have a resolution of 10 m; the four Red-Edge and two Shortwave-Infrared (SWIR) a resolution of 20 m; Coastal aerosol, water vapor and SWIR Cirrus a resolution of 60 m.

In addition, being intended for monitoring vegetation, soil, and water cover (Wang et al., 2016), Sentinel-2 images are accompanied by a Scene Classification Layer (SCL), which provides information of the surface type of each pixel (Main-Knorn et al., 2017). The layer is delivered as a normal band, has a 20 m spatial resolution and contains 12 classes (1 to indicate missing data, 9 surface cover types and 2 for cloud probability). The different categories are indicated in Table 2 and can be used during data preparation to include or exclude specific land cover types from the analysis.

Table 2: List of the single classes in Sentinel-2's Scene Classification Layer with the corresponding Label and Color.

Label	Classification	Color
0	No Data	
1	Saturated or Defective pixel	
2	Topographic casted shadows (former "Dark features/Shadows")	
3	Cloud Shadows	
4	Vegetation	
5	Not-vegetated	
6	Water	
7	Unclassified	
8	Cloud medium probability	
9	Cloud high probability	
10	Thin cirrus	
11	Snow or ice	

Figure 7 shows an example of how an image is flagged in the Scene Classification Layer. In this case the majority of the area was cloud covered (white and light grey pixels), with some areas being either vegetation (green) or not-vegetated (yellow) and the rest classified as snow or ice (pink).

Figure 7: SCL band of Sentinel-2 for the Chalberweid area captured on the 24th of April 2023. White and grey correspond to high and medium cloud probability, pink to snow or ice, yellow to not-vegetated, green to vegetation and black to No Data.

5.1.1.1. The WorldCover mask

The Worldcover dataset is based on Sentinel-1 and Sentinel-2 data and consists in a raster where land cover is divided into 11 different classes: Tree cover, Shrubland, Grassland, Cropland, Built-up, Bare/sparse vegetation, Snow and ice, Permanent water bodies, Herbaceous wetland, Mangroves, and lastly Moss and lichen (Zanaga et al., 2022). It serves the purpose of determining which surface cover types are to be included in the analysis and which ones are not. Figure 8 shows the mask derived from the Worldcover dataset used in the analysis to mask out built-up areas (white pixels) and keep all other surface types (black pixels).

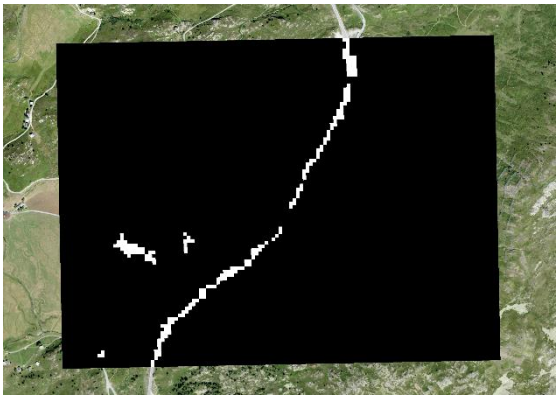

Figure 8: Mask obtained from the Worldcover raster indicating areas of built-up (in white) from other surface features (in black).

5.1.2. Landsat-8

Landsat-8 was launched in February 2013 as part of the Landsat program first started in 1972 (Acharya and Yang, 2015). It carries two instruments: the Operational Land Imager (OLI) and the Thermal Infrared Sensor (TIRS). The first one collects data in the visible, Near Infrared and Shortwave Infrared with an addition of a Panchromatic band operating between 0.500 and 0.680 μm. Every band has a spatial resolution of 30 m, with the exception of the Panchromatic one being 15 m. On the other hand, the Thermal sensor capture images in the Long-wave Infrared (LWIR) with a spatial resolution of 100 m (Acharya and Yang, 2015). Landsat-8 has a revisit time of 16 days, which is reduced to 8 days when paired to other Landsat satellites.

Similarly to Sentinel-2, Landsat-8 scenes are delivered with a band used to categorize pixels and flag images. The Quality Assurance (QA) band is included to indicate the presence of terrain shadows, data artifacts, clouds and other surface elements not belonging to the focus of the analysis (USGS, 2013). It serves a similar purpose to Sentinel-2's SCL described in chapter 5.1.1, with the difference on being the result of a binary classification based on different surface types and probability rather than on a simple numerical categorization.

5.1.3. Landsat-9

Landsat-9 was launched in September 2021 with the goal of replacing Landsat-7, which was operational since 1999, as the paired satellite to Landsat-8 (Masek et al., 2020). It was conceived as a near copy of L8 with some improvements regarding signal-to-noise-ratio (SNR) for darker targets and increased radiometric accuracy and geolocation of the TIRS instrument ((Masek et al., 2020). Even though the instruments have been improved, L9 has the same characteristics as L8 in terms of spatial, temporal, and spectral resolution. Since it orbits with a revisit time shifted 8 days from L8, the interval between Landsat scenes is reduced from 16 to 8 days.
As the launch took place at the end of 2021, L9 complemented L8 images only for 2022 and 2023.

5.1.4. SuperDove

The first flock of Planet's Dove satellites was launched in 2014 and over the years the PlanetScope constellation reached an approximate total of 130 satellites. The sensors are 3U[1] CubeSats measuring 10 cm x 10 cm x 30 cm and weighing 5.8 kg. They orbit at an altitude between 450 km and 580 km, operating with a spatial resolution of 3 m and with a revisit time of one day.

Figure 9: On of the SuperDove satellites part of the PlanetScope Constellation. Image credit: Planet Labs.

Through Planet Explorer it is also possible to have access to High Resolution (< 1 m), Medium Resolution (3-7 m) and Non-Planet Datasets (>10 m), which are Sentinel-2 and Landsat-8. High-Res SkySat images are only available in predetermined locations, which do not include the Chalberweid area. The access to these products can only happen upon request and requires a paid plan. Medium Resolution images are originated either using RapidEye, which however was dismissed by Planet in 2020 and has therefore limited utility in this Thesis, or using PlanetScope Sensors, i.e., three cohorts of satellites with IDs PS2 (Dove-C), PS2.SD (Dove-R) and PSB.SD (SuperDove). PS2 has four bands: Blue (455-515 nm), Green (500-590 nm), Red (590-670 nm) and NIR (780-860 nm). Dove-R is a four-bands imager with a butcher-block filter providing Blue (431-452 nm), Green (547-585 nm), Red (650-682 nm) and NIR (846-888 nm) stripes. SuperDove is an eight-band imager with a butcher-block filter supplying Band 1: Coastal Blue (431-452 nm), 2: Blue (461-515 nm), 3: Green I (513-549 nm), 4: Green II (547-583 nm), 5: Yellow (600-620 nm), 6: Red (650-680 nm), 7: Red-edge (697-713 nm) and 8: NIR (845-885 nm) stripes. For this Thesis the data was provided by SuperDove, as it showed an improved radiometric quality compared to Dove-C and Dove-R (Wicaksono et al., 2023), which are

[1] A standard IU is a 10 cm cube, 10 cm x 10 cm x 10 cm (Poghosyan and Golkar, 2017)

characterized by a lack in separation between the spectral response of the RGB bands for Dove-C, and an overall worse radiometric accuracy in the case of Dove-R (Frazier and Hemingway, 2021). One advantage of using Planet data is the interoperability with Sentinel-2, as the Bands Coastal Blue, Blue, Green II, Red, Red-edge and NIR share the same Central Wavelength (CWL).

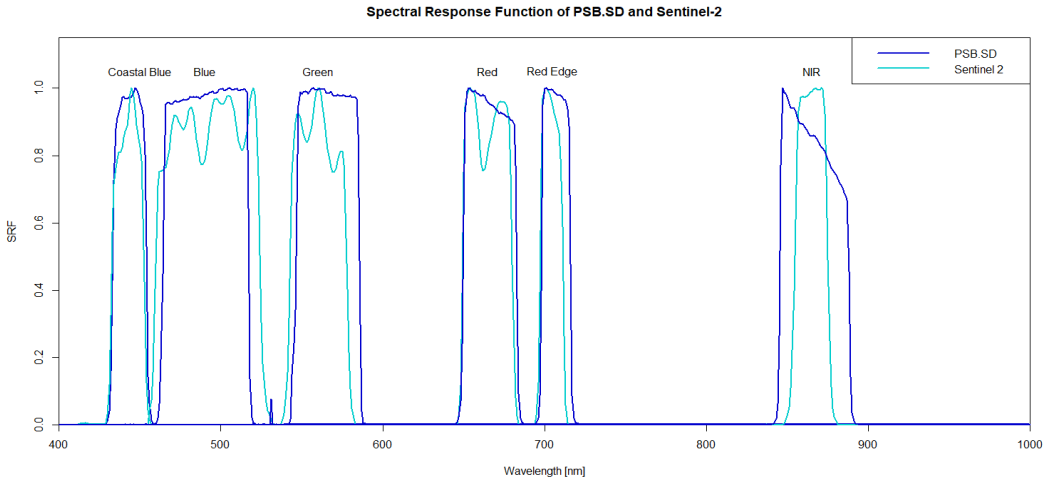

Figure 10: Spectral Response Functions of SuperDove (blue) and Sentinel-2 (light cyan).

5.1.4.1. The Planet product

The access to Planet images is granted through different types of subscriptions. The Education and Research Program has two tiers of licenses, namely the Basic and the Campus. The Basic plan grants download of up to 5'000 km^2 of PlanetScope aerial images each month, is free of charge and must be renewed annually. There is however a minimal charge of 100 km^2 per image, therefore, the amount of monthly downloadable images is limited to 50, independently of the size of the selected area. This means that even though the chosen Chalberweid area covers only 0.846 km^2, it is still counted as 100 km^2. The Campus License is aimed at usage by both students and research staff of entire Universities, provides access to a maximum of 2'000 users. It grants download to a maximum of 100 million km^2 of PlanetScope and RapidEye Imagery, 200'000 km^2 of SkySat Archive Imagery, has a license duration of 12 months and is priced at 35'000 USD. For this Thesis, the download of images was tied to the Basic license. The scenes download is done through the explorer page of the Planet website. The first step consists in choosing the Area of Interest (AOI), which can be either previously created and uploaded or directly drawn in the webpage. The second step is filtering the results by date, sensor type and cloud cover. Once all the images meeting the selected criteria are displayed, the suitable ones are selected, and the order is submitted. Planet also provides a Usable Data Mask (UDM), a raster of the same extent of the selected images, which follows the same principle as Sentinel-2's SCL. The UDM layer proves to be useful if the download of images takes place in bulk, as it can be used to eliminate from the analysis pixels which are not relevant to a phenological analysis. For this Thesis however, this feature is not exploited, as due to the limited amount of monthly downloadable scenes set by the Educational and Research plan, the images are manually selected.

5.2. Multispectral drone

The chosen drone for the analysis is the DJI Mavic 3M, a multispectral UAV equipped with one 20MP RGB camera and four 5MP multispectral cameras operating in the Green (560 ± 16 nm), Red (650 ± 16 nm), Red Edge (730 ± 16 nm), and Near Infrared (860 ± 26 nm) spectrum. In addition, the Mavic 3M offers the possibility of processing and storing NDVI images. This function was not used as NDVI was calculated from the single channels.

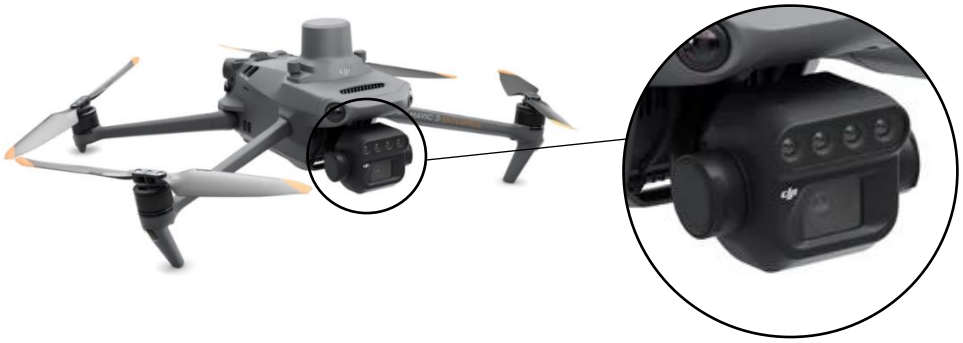

Figure 11: DJI Mavic 3M with a closeup on the equipped sensor. The four cameras on top from left to right are sensitive to NIR, Red edge, Red and Green, while the one below is an RGB.

5.2.1. NIR channel advantages and image referencing

The main advantages of drones over full-size aircraft and satellites are the high spatial resolution (which is directly dependent on the chosen flight altitude, but it is usually between 3 and 5 cm), control over the surveyed area, possibility of choosing the acquisition time and relatively low operational costs (Mahajan and Bundel, 2016). As previously mentioned, the drone used for the analysis is the DJI Mavic 3M, which, besides an optical sensor, is equipped with a multispectral camera. The first advantage of a multispectral UAV over an RGB one is the possibility of using together images captured under different light conditions, as even when conditions switch from direct to diffuse radiation or vice versa, there are not problems regarding missing of incompatible data (Fawcett et al., 2021). The advantage becomes particularly relevant considering the approach used by Geoformer. Since the method relies on the brightness of an RGB image, and the study area is located in an alpine region (where weather changes quickly and clouds can accumulate and cover the sun in a matter of minutes), the use of multispectral images shows a significant advantage over optical imagery in this particular research. The second advantage relies on the NIR channel, which offers an added perspective on vegetation, which is not the case for optical images.

For what concerns referencing the acquired images, there are two main methods which allow to have georeferenced data: using Ground Control Points (GCPs) or Real Time Kinematic (RTK). The first one consists in placing on the ground objects that are easily distinguishable (usually a black and white circle or a checkered square) and marking the coordinates. Then, during processing, these points and their known locations are used to reference the rest of the image. The number of needed GCPs is not fixed and depends on the study area. Yu et al., set the number at 12 for areas between 7 and 39 ha, category into which would fall

the Chalberweid drone area, covering 24.43 ha. This method however requires to manually place and then remove the points alongside the perimeter of the study area (Martínez-Carricondo et al., 2018), thus increasing the time needed for the survey and rendering the measurement of GCPs coordinates the most time-consuming on-site operation of an UAV survey (Forlani et al., 2018).

To this matter, using RTK negates the need for CGPs. This methods functions using a base station with known coordinates, a drone mounted with an RTK module and a Global Navigation Satellite System (GNSS). Firstly, the real time position is determined by the GNSS for both the drone and the station. Then, the position of the drone is corrected according to the known, constant position of the station (Orengo et al., 2021). Throughout the whole survey time, the UAV system (drone and remote) needs to be connected to the Internet, otherwise the determination of position is not possible.

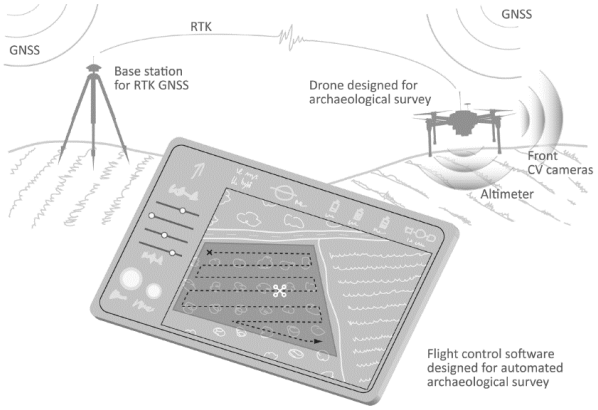

Figure 12: Schema representing the components used in an RTK based UAV flight (Orengo et al., 2021).

As a result, each time an image is captured, the 3D position of the camera is registered, thus resulting in georeferenced images without the need to climb to the study area. This aspect becomes particularly relevant when working in large areas or inaccessible and hazardous sites. Using RTK does not only come with advantages, there are also some drawbacks. The first one is the initial cost of the system when compared to a standard drone, which however is counterbalanced by the time saved for not setting up the GCPs grid and the relative increase in productivity (i.e., possibility of surveying multiple different areas in the same day) (Taddia et al., 2019). The second disadvantage resides in possible connection issues. Since the drone constantly communicates with the station, a loss of internet signal can lead to a lack of referencing. Similarly, it is possible to experience the loss of GPS signal, which also results in unreferenced images (Um et al., 2020).

Overall, both methods have advantages and drawbacks. GCPs are more secure as they rely on physical objects, however, they require hands-on work to be placed, which in certain situations is not feasible. On the other hand, RTK offers a more practical approach, yet it is also subject to referencing errors.

5.2.2. Flight planning and image processing

Mission planning was done using Drone Harmony and the Advanced terrain Hillscan mode. This function proves to be particularly useful in sloped and complex areas, as the camera orients itself perpendicular to the surface every time it acquires a scene, resulting in a constant Ground Sampling Distance (GSD) and a uniform image overlap. The final flight plan is displayed in Figure 13, which shows the area covered in each one of the three flights performed and the path followed by the drone during each survey.

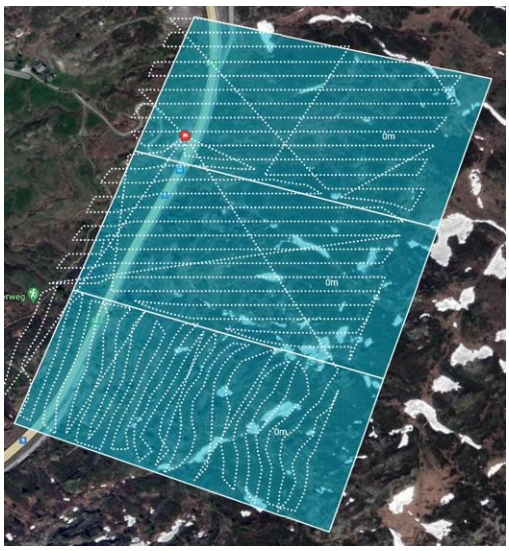

Figure 13: Flight plan visualized in the Drone Harmony interface. Each blue rectangle corresponds to a single flight while the white lines trace the path followed by the drone.

The complete area covers a surface of 244'322 m^2, which, originally, was split into 2 equal parts. However, after evaluating the number of waypoints and flight time in each of the two halves, the plan was split into 3 parts, as it would not have been possible to cover the whole surface without interrupting the flight. The first sector is 77'606 m^2, the second 82'412 m^2 and the third 84'304 m^2. The number of waypoints in each sector is 198, 247 and 231. The number of captures is greater in the second and third sectors because of the bigger area covered and the manual addition of measuring points, which was done mostly along the border lines between the sectors to fill the gaps between the different paths.

However, it was not possible to choose the path followed by the drone, as this is done autonomously by Drone Harmony. This leads to the difference in trajectory between the first two plans, which follow a linear flight, and the third one, which is characterized by a more erratic trajectory. The reason behind the different paths is the goal to use as little energy as possible and therefore to maximize flight time. Since the chosen mission is based on terrain, the program follows the complex topography and tries to avoid hovering (as this consumes the most energy), resulting in the drone not flying on straight lines.

Both frontal and side overlap are 75%, following both pix4D guidelines and other researchers' approach (Jiménez-Jiménez et al., 2021). Increasing the overlap would not bring any benefits, as the limited increase in

overlapping accuracy would not justify the higher number of images needed to cover the same area. Moreover, it has be shown how choosing an extremely high overlap value (90%) does not offer an advantage in accuracy, as it causes a higher height error and deformations at the edges of the model (Rosnell and Honkavaara, 2012). The maximum flight height was set at 120 m. This value was chosen both as this is the maximum altitude allowed in the open category and because of the already high accuracy of Digital Elevation Models (DEMs) of complex terrain generated at a flight altitude of less than 150 m (Nguyen et al., 2020). A lower flight height means a smaller GSD and therefore a higher resolution, however, having a smaller pixel size was not one of the goals. After processing, the obtained average GSD was 4.45 cm for the first flight, 4.47 cm for the second and 4.46 cm for the third one.

All image processing was done in Pix4D using the 3D Maps workflow, which, using a collection of aerial pictures recorded following a flight plan, creates an Orthophoto, a Point Cloud and a Digital Surface Model (DSM).

6. Algorithms

The following section covers the algorithms and the relative components for each one of the methods used.

6.1. Snow cover detection through Land Surface Phenology

The term Land Surface Phenology (LSP) refers to the study of annually recurring sequence of plant developmental stages (Piao et al., 2019) using satellite-derived vegetation indices (VI) which serve as proxy for vegetative vigor and amount (Caparros-Santiago et al., 2021). The principles of the chosen LSP model, better explored in chapter 6.1.2, are based on the relationship between vegetation indices time series, start of vegetation activity and snow cover. The model is developed with the goal of using fitted Normalized Difference Vegetation Index (NDVI) time series to determine the timestamp at which vegetation activity starts and to tie the extracted day of the year (DOY) to the moment at which snow has melted from the area.

6.1.1. Principle of NDVI

The Normalized Difference Vegetation Index was chosen as it is one of the earliest remote sensing metrics used to simplify complex multispectral images and to characterize vegetation health and activity. Due to its long history, simplicity, and reliance on easily obtainable bands, NDVI is now established as the most used index for vegetation assessment (Huang et al., 2021).

Its physical principle is based on the interaction between solar radiation and the different components of vegetation. The radiation in the visible spectral region (VIS) is used as a source of energy during photosynthesis by live green plants and is identifiable by an increased red-light absorption caused by chlorophyll (Horler et al., 1983). At the same time, the light emitted in the near-infrared (NIR) spectral region is reflected or transmitted by leaves due to high internal scattering (D'allestro and Parente, 2015). This spectral contrast forms the basis, besides for NDVI, for many other vegetation indices (Henebry and De Beurs, 2013). As can be seen in Figure 14 the reflectance spectrum of vegetation has a particular shape that does not resemble the ones of

other surface types, which show a more constant increase or decrease. This difference results in being able to easily separate healthy and active vegetation from bare soil and water.

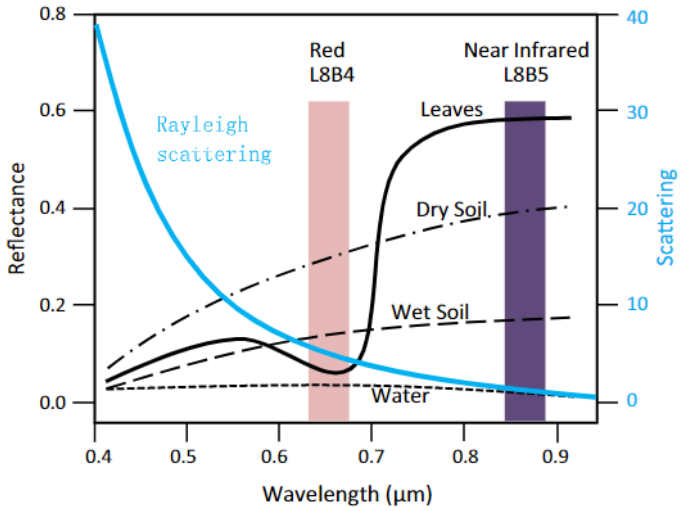

Figure 14: Spectral response curves of different surface cover types, the pink bar represents the Red portion of the spectrum while the purple one corresponds to the Near Infrared interval. In light blue is the wavelength dependent scattering (Huang et al., 2021).

Mathematically, NDVI is calculated as follows:

$$NDVI = \frac{\text{NIR} - \text{RED}}{\text{NIR} + \text{RED}} \qquad \text{Eq. (1)}$$

The index is obtained by dividing the difference between the Near Infrared band (NIR) and the Red band (RED) and their sum. The resulting value is dimensionless and goes from a minimum of -1 to a maximum of 1. Healthy vegetation usually is characterized by higher NDVI values (>0.6). The table below indicates a general interpretation of the values (Alex et al., 2017), these however are not fixed and can vary depending on the vegetation type (Meneses-Tovar, 2011).

Table 3: General interpretation of NDVI values (Alex, Hari and Ramesh, 2017).

Land Cover Type	NDVI Value
Water, Snow, Cloud	-1 < X < 0
Bare soil, Built-up, rocks	0 < X > 0.2
Vegetation	0.2 > X < 1

Therefore, different NDVI time series of both Sentinel and Planet were analyzed to extract phenological metrics. The start of the growing season was then set as the first snow free day of the year, so that it was possible to assess snow cover dynamics without the need for snow specific indices such as the Normalized

Difference Snow Index (NDSI). The latter was not used due to the low spatial resolution of the SWIR channel (needed for the calculation of the index) in both Sentinel-2 (20 m) and the two Landsat instruments (30 m), which would result in consistently failing to identify the different snow patches. Moreover, since the Super Dove does not have a band operating in the shortwave infrared, it would not have been possible to compare the Planet results to the ones obtained from Sentinel and Landsat.

6.1.2. LSP Workflow

The first step consists in generating the files necessary to create and characterize the Area of Interest (AOI). These include a text file that describes the encoding used to create the shapefile, a text file indicating the chosen coordinate system and projection and a file containing shape, location, and attributes of the geographical features. These files were created in QGIS, and the chosen area was the same for Sentinel, Landsat, and Planet images. As previously mentioned, the area chosen for the satellite images is much larger than the actual Chalberweid area and was clipped during the analysis. The following step is the download of images for the selected years. In the case of Sentinel-2, Landsat-8, Landsat-9 and WorldCover the download of images is done through a Python script and Google Earth Engine, while for PSB.SD the download is carried directly through the Planet website. As previously mentioned, both Sentinel and Landsat data have a band used for flagging pixels containing features not relevant to the analysis. Therefore, in the case of Sentinel-2 the red channel is flagged using the SCL layer, meaning that if a pixel in the red channel corresponds to a chosen flag in the SCL layer, its value gets converted to NA. Through this flagging process, land cover types that are not relative to the research are excluded. For Sentinel-2 the chosen flags are the following: 0 (no data), 1 (Saturated or defective), 2 (dark area pixels), 3 (cloud shadows), 6 (not vegetated), 8 (cloud medium probability), 9 (cloud high probability), 10 (thin cirrus). The included flags are 4 (vegetation), 7 (unclassified) and 11 (snow). The flagging of L8 follows a similar principle but instead of an SCL, a Quality Assurance (QA) band is provided. It is based on binary numbers, which reflect the characteristics of a given pixel, i.e., the Pixel Value is the result of the binary number created using the values of each flag.

Next, NDVI gets calculated both with the flagged and the unflagged red channel. Figure 15 (a) and Figure 15 (b) show the final result of the flagging process.

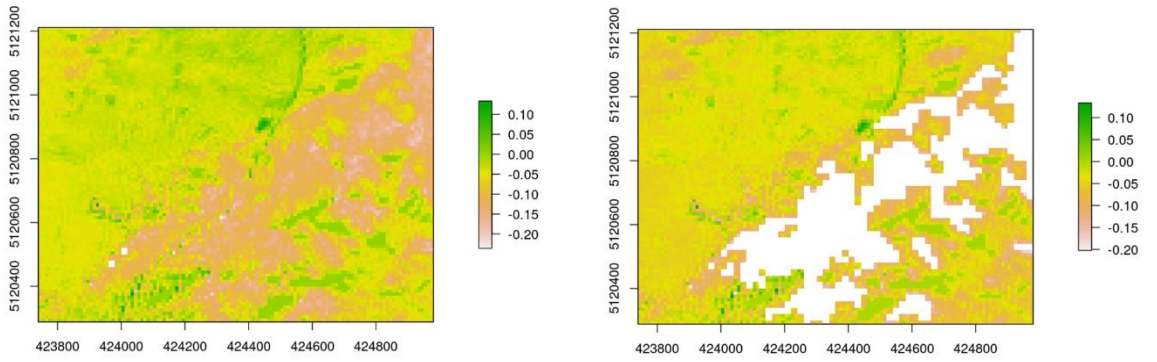

Figure 15 (a) and (b): Unflagged Sentinel-2 NDVI image of the Chalberweid area captured on January 7th, 2019, versus its flagged counterpart using Sentinel-2's Scene Classification Layer (SCL).

The image on the left represents the NDVI values during the third acquisition of 2019, while the one on the right is the same image with the selected pixels flagged out. The areas of lower NDVI in the image on the left correspond to dark features and shadows and therefore will not be included in the phenology analysis.
Then, using the WorldCover image shown in Figure 8, mask out every surface element that corresponds to man-made features, in the case of Chalberweid these are the road and the Barralhaus.
After that, the actual High Resolution Phenology workflow can start. Firstly, a set of functions to fit the time series and to identify peaks in the NDVI plot is created. Then, the pixel loop is started so that for each pixel of each available image the same operations are carried out. At this point each time series undergoes a double logistic fit, which offers the advantage of creating a continuous set of NDVI values without the need of data pre-smoothing or user-defined thresholds (Zhang et al., 2002).

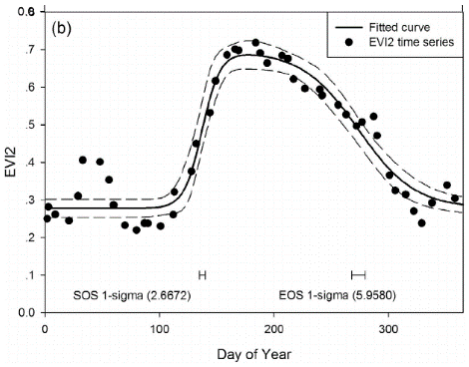

Figure 16: Example of a time series fitted using a double-logistic function (Yang et al.*, 2012).*

Even though the double logistic approach does not provide the overall most accurate fit (Vorobiova and Chernov, 2017), it is more indicated for NDVI time series of high alpine regions, as the resulting curve can better follow the abrupt and brief increase and decrease of NDVI values.
After the curve fitting, the pixels are flagged and excluded from the analysis if they meet one or more of the following conditions: 1 → there are less than 7 observations, 2 → the mean NDVI is smaller than 0.2, 3 → The amplitude of the curve is smaller than 0.1, 4 → there is no phenological curve, 5 → the dormancy phase does not exist, 6 → there are less than 66% valid observations left after fit, 7 → the value of the F-test is greater than 0.05. All these flags serve the purpose of eliminating from the analysis pixels where vegetation is not predominant or where plant activity is not significant enough, which would otherwise negatively influence the estimation of phenological metrics.
Next, based on the fitted curve, the 3rd derivative is calculated, thus determining the turning points (green up and senescence), extract the timestamps of said points, and get the RMSE for sections of the phenological curve. Figure 17 shows how the local maximum of the 3rd derivative corresponds to the beginning of the green up phase (Tan et al., 2011). The day of the year marked by the local maximum was set as the Start of Deflection of vegetation activity and was determined to be equivalent to the moment of snowmelt.

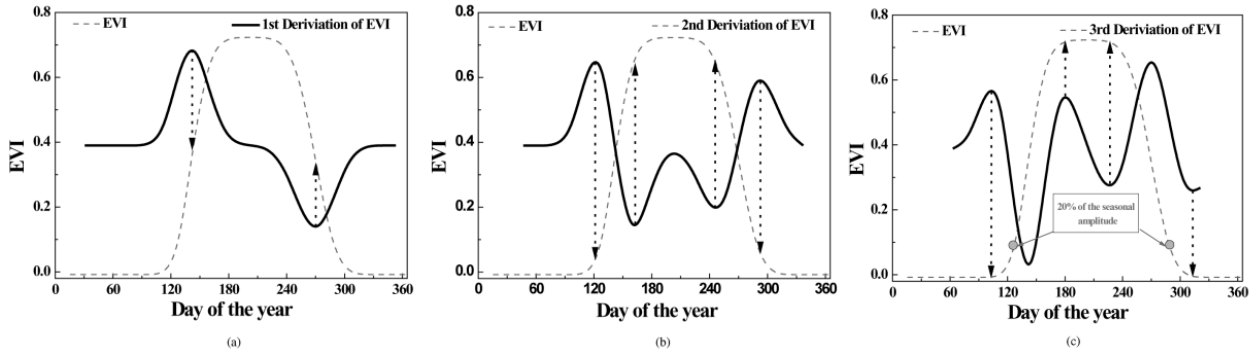

Figure 17 (a), (b) and (c): Example of deflection points extracted from the 3rd derivative on an Enhanced Vegetation Index (EVI) time series (Tan et al., 2011).

Figure 18 shows a fitted Planet NDVI time series of a single pixel. Each one of the single green circles represents a Planet image acquired during the year. The purple rhombus indicates the Start of Deflection and has a value of 102.5 days. Besides the deflection points, the LSP model also calculates the Start (SOS) and End of Season (EOS) using the midpoint method. However, since the midpoint method does not offer a connection to snow melting as strong as the Start of Deflection does, it has been considered irrelevant for this research.

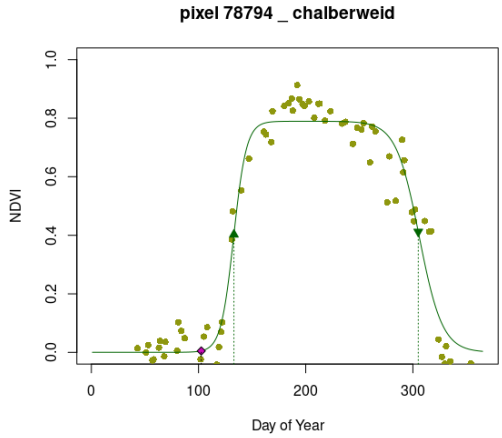

Figure 18: Example of the extraction of the phenological metrics of a pixel in a SuperDove scene. The purple rhombus indicates the Start of Deflection determined by the 3rd derivative of the fitted NDVI time series.

The process of time series fitting, flagging and phenological metrics extraction is then repeated for every pixel available so that in the end there would be a data frame containing the statistical and phenological metrics at pixel level for the entire area.

The LSP workflow was designed to complement Sentinel-2 images with Landsat-8. Following its launch in September 2021, Landat-9 images were used alongside S2 and L8. As the images were available only from end of October 2021, they were usable only for 2022 and 2023. In the case of Planet data, the script was adapted to work with the different image parameters denomination and the absence of a flagging system.

6.2. Using NDVI to create snow cover and snow melt maps

The principle behind the realization of snow cover and snow melt maps is the same as the one described in chapter 4.1, i.e., create single day snow cover maps by choosing a threshold value to apply to the single pixels and determine which areas are snow covered and which are not. Then, if there are enough snow cover maps available during the melting phase, it is possible to create a snow melt map identifying where snow melts first and where last. The instruments used for this approach are the DJI Mavic 3M, Sentinel-2 and SuperDove. In the case of the UAV however, not enough surveys were performed, resulting in only being possible to create two single day snow cover maps and one completely snow free orthophoto.

As previously mentioned, the Mavic 3M is not limited to a camera operating just in the visible spectrum but is equipped with a multispectral sensor with bands in the Green, Red, Red-Edge and NIR wavelengths. While the Green channel has no specific use in this thesis, the other bands can be used to calculate NDVI, following the same principle presented in chapter 6.1.1. Contrarily to the optical approach, using NDVI does not require choosing a threshold reflectance value, as the classification in "snow" or "not-snow" is done exclusively through NDVI. In addition, the Red-Edge (RE) band can replace Red in the calculation of NDVI. RE is defined as the spectral region between 680 and 750 nm where there is a sharp change in the vegetation reflectance (Horler et al., 1983) and should offer an advantage over classic NDVI in regions of perennial herbaceous plants and meadow (Schuster et al., 2012) such as the Chalberweid one.

The principle is the same as the one for the Drone generated snow cover maps, i.e., for each image an NDVI threshold value is selected, thus allowing the identification of snow cover. In this case however, due to the high temporal resolution of Planet images, it is possible to combine numerous snow cover maps to create a melt-out map which can identify the different melting patterns. The single day NDVI snow cover maps were converted to a binary classification, so that snow covered pixels were associated to the number 1, while snow free ones were converted to 0. As a result, after summing all the binary snow cover maps, it was possible to identify which surfaces were still snow covered later in the year (greater values) and which ones are freed sooner (lower values). The resulting numbers can then be converted into day of the year, so that they can be better compared to both other NDVI melt maps and Start of Deflection images.

6.3. Multispectral-drone-derived snow depth map

As mentioned in chapter 5.2.2, besides orthophotos and point clouds, the images acquired by the Mavic 3M can be used to create a DSM of the study area. This is generated in Pix4D by combining the single images and creating a point cloud, from which then the DSM is derived (Shoab et al., 2022). The accuracy of the DSM strongly depends on the chosen flight parameters, as a lower flight altitude and a higher degree of image overlapping would result in a denser point cloud, which ultimately would produce a more accurate DSM (Chaudhry et al., 2021). However, since the chosen flight height was 120 m, which is below the indicated minimum altitude of 150 m required for an accurate DSM (Nguyen et al., 2020), the quality of the DSM was deemed sufficient for creating a snow depth map. The principle of creating such a map lies in the different snow presence during the different surveys. Since during the first flight the whole area was almost completely snow covered, and during the third one there was no snow left, the difference between the two DSMs should reflect the snow height at the moment of the first survey. This method follows the one presented by Forlani et al., who, in 2018 investigated the accuracy and repeatability of DSM generation by calculating the elevation difference between different surface models. Figure 19 illustrates how a snow map is derived from the difference between two DSMs, the green figure represents the terrain while light blue corresponds to the height of the snow deposit during the first survey.

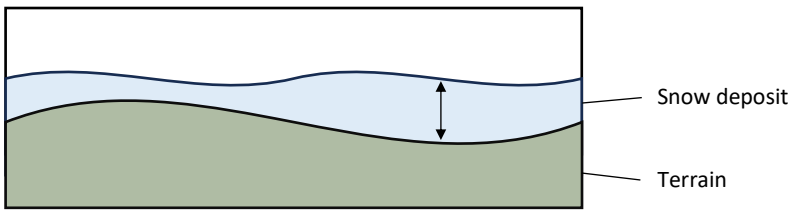

Figure 19: Drawing of the principle behind the creation of a snow map using two DSMs. The green area represents the terrain, while the light blue one corresponds to a snow deposit.

7. Comparison between yearly and average results

Two types of comparison have been performed, the first one focused on the difference between methods for the single years, while the second between the average performance of each approach over the course of the same period. The first comparison had the goal of investigating the single year difference to identify any particular performance discrepancies tied to the weather experienced during the year, while the second one had the objective of highlighting any discrepancies in identifying patterns related to topography or surface features. Table 4 gives an overview on which products have been compared, the lower left part is grey colored to avoid redundancy.

Table 4: Overview of the comparisons performed during the analysis, the blue colored squares indicate which methods have been compared. "Defl." corresponds to the Start of Deflection, "Melt." to the snow melt maps and "Cover" to the single day snow cover maps.

			Sentinel-2				**SuperDove**				**RGB UAV**			**MS UAV**
			Defl.		Melt.		Defl.		Melt.		Cover	Melt.		Cover
			Y.	Avg	Y.	Avg	Y.	Avg	Y.	Avg	Day	Y.	Avg	Day
Sentinel-2	Defl.	Year	-											
		Avg		-										
	Melt.	Year			-									
		Avg				-								
SuperDove	Defl.	Year					-							
		Avg						-						
	Melt.	Year							-					
		Avg								-				
RGB UAV	Cover	Day									-			
	Melt.	Year										-		
		Avg											-	
MS UAV	Cover	Day												-

7.1. Data pre-processing

7.1.1. Resampling

In order to be compared to one another, the raster with the higher spatial resolution was always resampled to match the lower resolution raster, following a similar approach to the one used by Helfenstein et al., who resampled 2m APEX data to match the spatial resolution of Sentinel 2. This means that 3 m SuperDove images were resampled to 10 m to match Sentinel data and 5 cm optical drone products to 3 m and 10 m respectively. Six different resampling methods have been tested: Nearest Neighbor, Bilinear, Cubic, Lanczos, Mean and Median. The selected one was Mean, as Nearest Neighbor, Bilinear and Cubic produced where the value difference between neighboring pixels was far too big, Lanczos wrongly increased the frequency of smaller values and Median oversimplified the image.

7.1.2. Normalization

If the comparison between the different years only requires matching spatial resolution, investigating average Deflection and snow melt values also involves data normalization.

The importance of this step is highlighted by Figure 20, which shows the distributions of the Start of Deflection values calculated using the combination of Sentinel-2 and Landsat-8/9 for the years 2021 (Band 1, in red in Figure 20 (a)), 2022 (Band 2, green colored) and 2023 (Band 3, blue), and the histogram of the same bands after normalization (Figure 20 (b)). On the histogram on the left the value ranges of the three Bands are not consistent, meaning that the Start of Deflection does not take place every year during the same period. While this kind of difference is the base of single years comparisons, it can distort the assessment of average patterns, as a year with extreme values will have a stronger influence on the average than one with more moderate measurements (Singh and Singh, 2020).

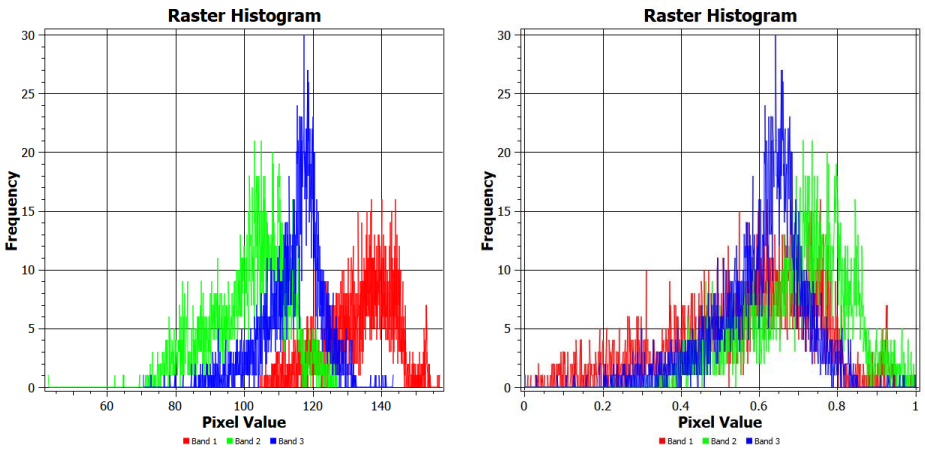

Figure 20 (a) and (b): histograms of S2 Start of Deflection raster of 2021 (Band 1, in red), 2022 (Band 2, green) and 2023 (Band 3, blue) in day of the year and same 3 raster but normalized.

To this matter, the normalization technique allows the recasting of the data to a specific range, for example between 0 and 1, thus mitigating the differences in the original Start of Deflection values (Peshawa & Rezhna,

2014). The mix-max scaling was used as the normalization technique, allowing the rescaling of values to a determined range, leaving the original data distribution untouched (Singh and Singh, 2022).
Data normalization formula (min-max scaling):

$$x' = \frac{\mathrm{x} - \min}{\max - \min} \qquad \text{Eq. (2)}$$

In the end, when using normalized data, it is possible to have a comparable metric to identify possible melting patterns between different years, having reduced the influence of extreme years.

7.1.2.1. Calculation of average pattern

As previously mentioned, using normalized data allows the identification of possible Start of Deflection or melting patterns. The first step in such an analysis is creating a normalized raster of the selected data for each one of the available years. In the case of the Start of Deflection, this translates in converting the raster from "day of the year" to a value between 0 and 1, so that instead of a number indicating at what time the Start of Deflection takes place, the pixel values denote in which areas the Deflection starts early or late. After having normalized all the available raster, for each one a binary mask is created, consisting of 0 and 1, where 0 indicates a pixel that is not associated with a Deflection value and 1 a pixel that does. This mask consists of a raster which has the same spatial resolution and extent as the original normalized image and will be used when calculating the average normalized Start of Deflection.
Afterwards, each raster has to get its NA values replaced with a real number, otherwise, it becomes impossible to calculate an average Deflection value. This step has to be performed as it is sufficient that one pixel between all years does not have a value, and the respective pixel of the final map gets converted to NA. In this case the NA pixels were converted to 0, so that they won't have any influence when calculating the mean value.
The final step consists in dividing the sum of the normalized Start of Deflection raster by the sum of the binary masks, resulting in a raster displaying the average normalized Deflection values, where it should be possible to notice any particular pattern of vegetation activity.

8. Results

8.1. Sentinel-2 Start of Deflection

Sentinel-2 and Landsat-8 were downloaded for the years 2018-2023 so that it was possible to compare the Start of Deflection maps both between in each other and to climate factors such as temperature and precipitation. Figure 21 shows the different Start of Deflection raster from 2018 (top left corner) to 2023 (bottom right) with their respective histogram indicating the distributions of deflection values. The colors help to identify the eventual Start of Deflection patterns, as darker shades of blue correspond to an early start, green to an average one and light green to yellow a late one. Contrarily to the color schema, the interval of the different histogram is not consistent.

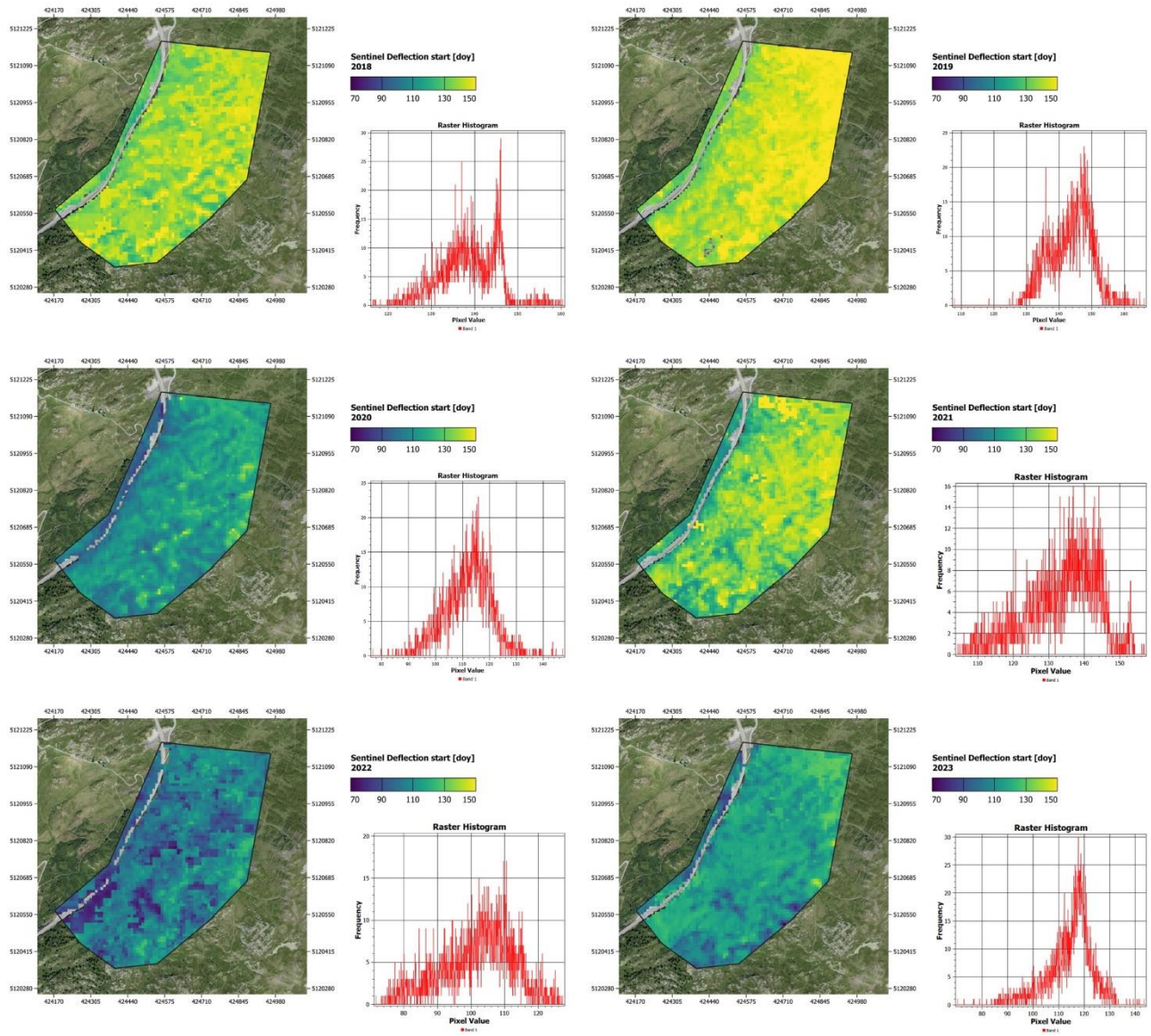

Figure 21 (a), (b), (c), (d), (e) and (f): Start of Deflection maps calculated using Sentinel-2 and Landsat-8/9 images from 2018 (top left) to 2023 (bottom right). Dark shades of blue indicate an early Start of Deflection, while light green and yellow correspond to a late one.

The Deflection started at the earliest in 2022, with a mean value of 102.09 days, followed by 2020 with 112.26, 2023 with 114.63, 2018 with 116.38, 2021 with 134, and lastly 2019 with 143.52. Based both on appearance and value distribution, the years can be divided into different categories based on their Deflection values. 2018, 2019 and 2021 belong to the late starting years, with 2019 being the most extreme case, while 2020, 2022 and 2023 to early starting, with 2022 as the earliest one.

Both the maps of 2021 and 2022 show some areas with great differences in Deflection values between adjacent pixels, which are clearly visible in the upper left and central part of the 2021 image (yellow pixels among green ones) and in lower left portion of the image of 2022 (dark blue between green). These discrepancies are tied to the NDVI values of the single pixels and to the relative curve fitting. Figure 22 shows the time series of two pixels close to each other, the one on the left (number 8478) has a Deflection value of 78.26 days while the one on the right (number 8493) 103.86. The two weeks difference is related to the shapes of the two curves, as the first one has a less steep increase than the second one, resulting in the Start of Deflection timestamp to be set earlier than in the case of pixels with differently shaped time series.

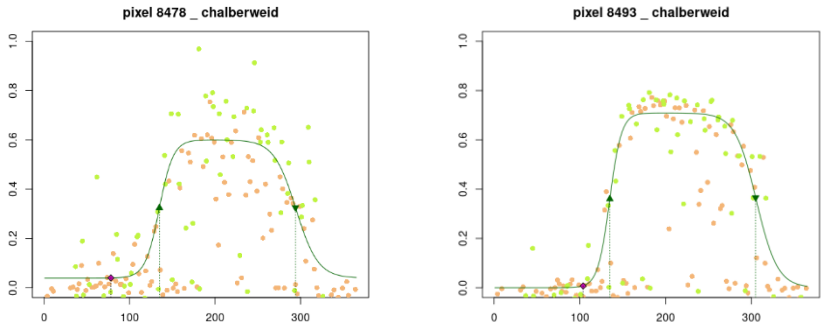

Figure 22 (a) and (b): Fitted NDVI time series of two pixels of the 2022 Start of Deflection map. The pixel in Figure (a) has a much smaller Deflection value than the one shown in Figure (b), despite being relatively close to each other.

For the years 2020, 2022 and 2023 the histograms are left skewed with one peak, meaning that there are no distinct areas where the Deflection takes place in a second moment. There are cases in which the histogram presents a second peak varying in magnitude, such as in 2018, 2019 and 2021. A second peak is related to pixels where the Start of Deflection took place particularly early or late in contrast to the rest of the area. This is visible for example in 2019, where the second sharp and narrow peak indicates areas where the Deflection started later (bright yellow pixels are in contrast with the majority of green colored ones). It must be noted that the second peak visible in the 2021 histogram is related to the different adjacent pixels mentioned above, and therefore the Deflection value is tied more to the chosen methodology and fitting process rather than to a late snowmelt.

A similar situation is observable in 2019, where the smaller peak is located before the main one, highlighting areas where the Deflection started earlier.

In the next chapter the different Start of Deflection are compared to the weather plots previously shown, to highlight possible relationships between climate factors and vegetation activity.

8.1.1. Relation between climate and Start of Deflection estimations

As mentioned in chapter 3, 2022 was the most extreme year in terms of both precipitation (only 657.2 mm) and temperatures (warm winter and summer). The low precipitations registered during the last months of 2021 and beginning of 2022, combined with an average winter temperature that never reached extremely negative values, resulted in an early activation of vegetation (Richardson et al., 2013), which ultimately lead to the small Start of Deflection values. This is also visible for 2020, which was also characterized by relatively high temperatures during the winter and a low amount of precipitation over the course of the first three months. In the case of 2020 both temperature and precipitation did not reach extreme positive and negative values, therefore the Start of Deflection did not happen as early as it did in 2022. 2023 belongs to the same late starting category as 2020 and 2022, however, since the magnitude of extreme temperatures and low precipitation is not as noticeable as it was in the case of the other two years, the Start of Deflection does not take place as early.

On the other hand, the Deflection started at the latest in 2019, a year which was characterized by low winter temperatures, and which was preceded by high precipitation during the final 3 months of 2018. This combination allowed for high snow deposits during the winter, which were then well conserved thanks to the low temperatures and precipitation of the following months. Similar conditions were also observed to a lesser degree for 2018 and 2021, resulting in late starting years.

In general, the conditions needed for a late Start of Deflection are high precipitation during the final months of the previous year, followed by a period of c.a. three months with little precipitation and low temperatures. A combination of both these two aspects is needed, as just one of the two (such as it is case of 2020, where precipitation was high during the end of 2020, but the average temperatures stayed quite high throughout the whole winter) is not enough to guarantee a late Start. On the other hand, a dry winter combined with a warm start of the year will result in an early Start of Deflection.

8.2. SuperDove Start of Deflection

Contrarily to Sentinel-2 and Landsat-8/9, SuperDove images were only available starting from 2021, resulting in the creation of only three Start of Deflection maps. These are 2021 in the top left corner of Figure 23, 2022 in the top right one and 2023 in the bottom left one.

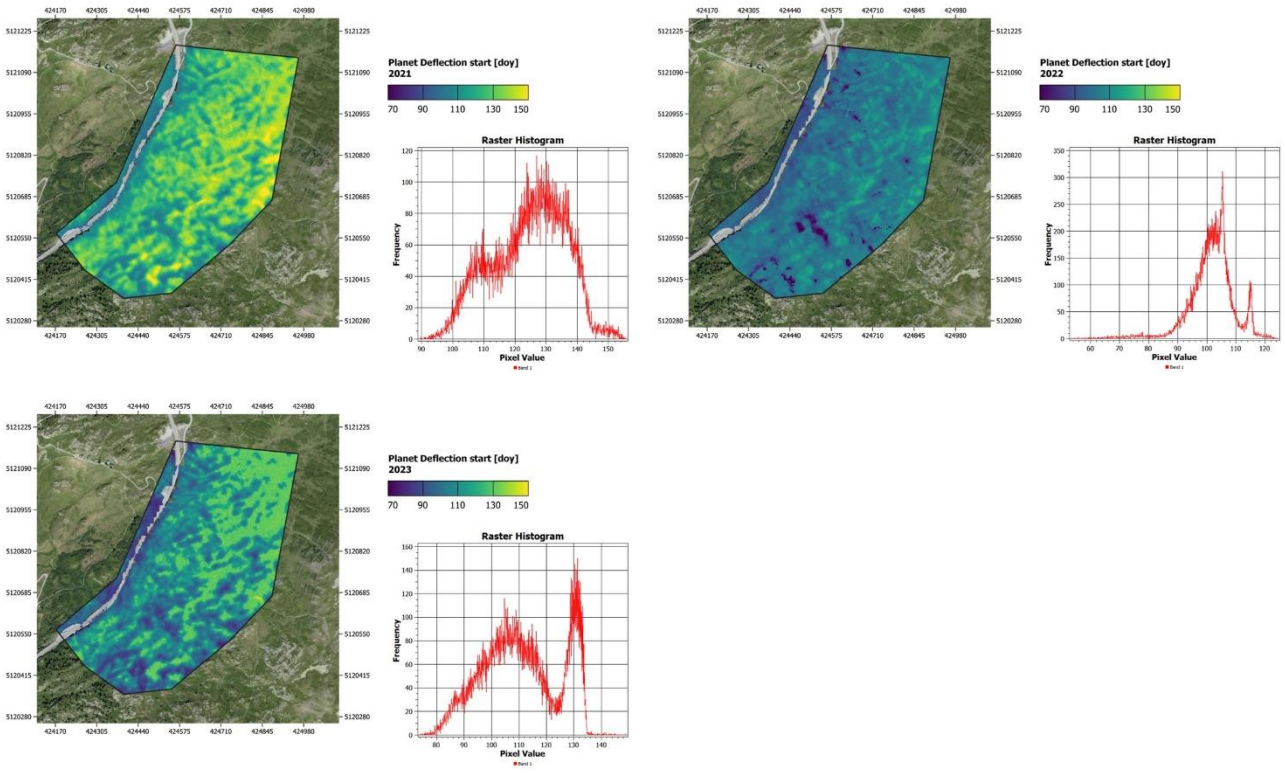

Figure 23 (a), (b) and (c): Start of Deflection maps calculated using SuperDove images from 2021 (top left) to 2023 (bottom left). Dark shades of blue indicate an early Start of Deflection, while light green and yellow correspond to a late one.

The color scheme and value interval used for the SuperDove maps is the same as the Sentinel one, meaning that a dark blue color indicates an early start while yellow or light green correspond to a late one.

2021 can be categorized as a late starting year, having a prevalence of dark yellow pixels (which translates to a Start of Deflection of approximately 130 days) with light blue being the second most frequent color (110 days). This prevalence is also visible in the histogram, which shows a principal peak at 130 days and a second, smaller one (that resembles more a deflection rather than a peak) at 110 days. The shape of the value distribution is a rather wide bell, meaning that the Start of Deflection did not take place in a short amount of time but on the contrary, the period of snow melt was prolonged. This particular behavior can be associated to late starting year, characterized by high precipitation and low winter temperatures, as was the case in 2021 (see chapter 3 and 8.1.1).

On the other hand, the map of 2022 is almost exclusively dark blue colored, with some green exceptions indicating later starting pixels. This corresponds to a particularly early Start of Deflection year, also highlighted by the histogram peak being located between 102 and 104 days, considerably earlier than what was observed in 2021. Contrarily to 2021, the shape of the histogram is much narrower, with a clear and smaller second peak

at day 115, meaning that in the majority of pixels the Deflection started within a similar interval, with some exception for a handful of later starting areas. As a result, the image appears more homogeneous, thus rendering the distinction between early and late start more difficult than in the case of a year with a more spread out Start of Deflection interval. The 2022 SuperDove map showed similarity to the Sentinel one, meaning that also in the case of Planet, the Start of Deflection raster directly reflects the weather experienced in the months preceding snow melt, which in 2022 was low precipitation and high temperatures.

Lastly, 2023 is characterized by both early and late starting areas, as the majority of pixels are either blue or green colored, associated with a Deflection value of 108 and 130 days respectively. This separation is also visible in the histogram, which shows a first, wider, bell shaped peak, followed by a second one, more pronounced but also within a shorter interval. This indicates that the Start of Deflection mainly took place at two distinct moments, the first one was more prolonged while the second one more abrupt, which means it was tied a rapid increase in temperatures which lead to the melting of the last patches of snow and relative activation of vegetation. Even in the case of 2023, the Start of Deflection timestamp is dependent on the weather experienced during winter. As seen in chapter 3, both precipitation and temperature registered low values, meaning that even though snow cover was not particularly high, the low temperatures prevented its melting, resulting in areas characterized by high snow deposits (such as small valleys) to experience a late Start of Deflection.

Overall, the SuperDove maps show the same relation between Start of Deflection and Climate as the one created using Sentinel-2/Landsat-8/9. In the case of Planet however, the higher spatial resolution allows for a better distinction between early and late starting areas, which is visible in both the appearance of the images and in the shape of the histograms.

8.3. Comparison between Start of Deflection results

The next sections cover the differences between the Start of Deflection maps for Sentinel and Planet by comparing each year individually. As an addition, the snow melt maps created by Geoformer using the optical drone are also added to the comparison, even though the method does not correspond to the one used for the Deflection maps. Afterwards, the average normalized snow melt maps for the three methods are analyzed, with the goal of determining if the areas highlighted as early and late starting/melting are consistent.

8.3.1. Yearly differences

Table 5 shows the statistic values of the 9 difference raster created, i.e., difference between the Start of Deflection of Sentinel and Planet with the addition of the relationship between Satellite and optical UAV. Each one of the three Planet available years (2021, 2022 and 2023) is analyzed using minimum raster value, maximum, mean and standard deviation, all expressed in days.

Table 5: Minimum, maximum, mean and standard deviation value for the yearly maps showing the differences between Sentinel and Planet Deflection and between the two satellites Deflection and Geoformer's snow melt maps.

		2021	2022	2023
Sentinel - Planet	Minimum	-9.79	-31.20	-20.51
	Maximum	48.41	38.49	39.78
	Mean	9.30	0.32	3.23
	Standard dev.	5.85	9.48	8.29
Sentinel - Geoformer	Minimum	-24.25	-44.19	-25.66
	Maximum	29.67	17.79	34.34
	Mean	-8.23	-10.96	-6.55
	Standard dev.	6.86	10.64	8.43
Planet - Geoformer	Minimum	-42.89	-40.15	-39.19
	Maximum	10.57	23.92	29.96
	Mean	-18.54	-10.25	-11.82
	Standard dev.	6.66	11.76	8.52

8.3.1.1. Sentinel-2 - SuperDove

Overall, the difference between Sentinel and Planet Start of Deflection maps always shows a positive mean value, meaning that in general Sentinel tends to set the Start of Deflection slightly later in the year than Planet. The difference is maximum in 2021 with a value of 9.30 and minimal in 2022 with 0.32.

Figure 24 shows the three maps displaying the difference in Start of Deflection values between Sentinel and Planet. All three images have the same value range and color schema, with red indicating a negative difference (meaning that the Deflection value of Planet was greater than the one of Sentinel), white a perfect match between the two sensors estimations and blue a positive difference (Sentinel set the Deflection later than Planet).

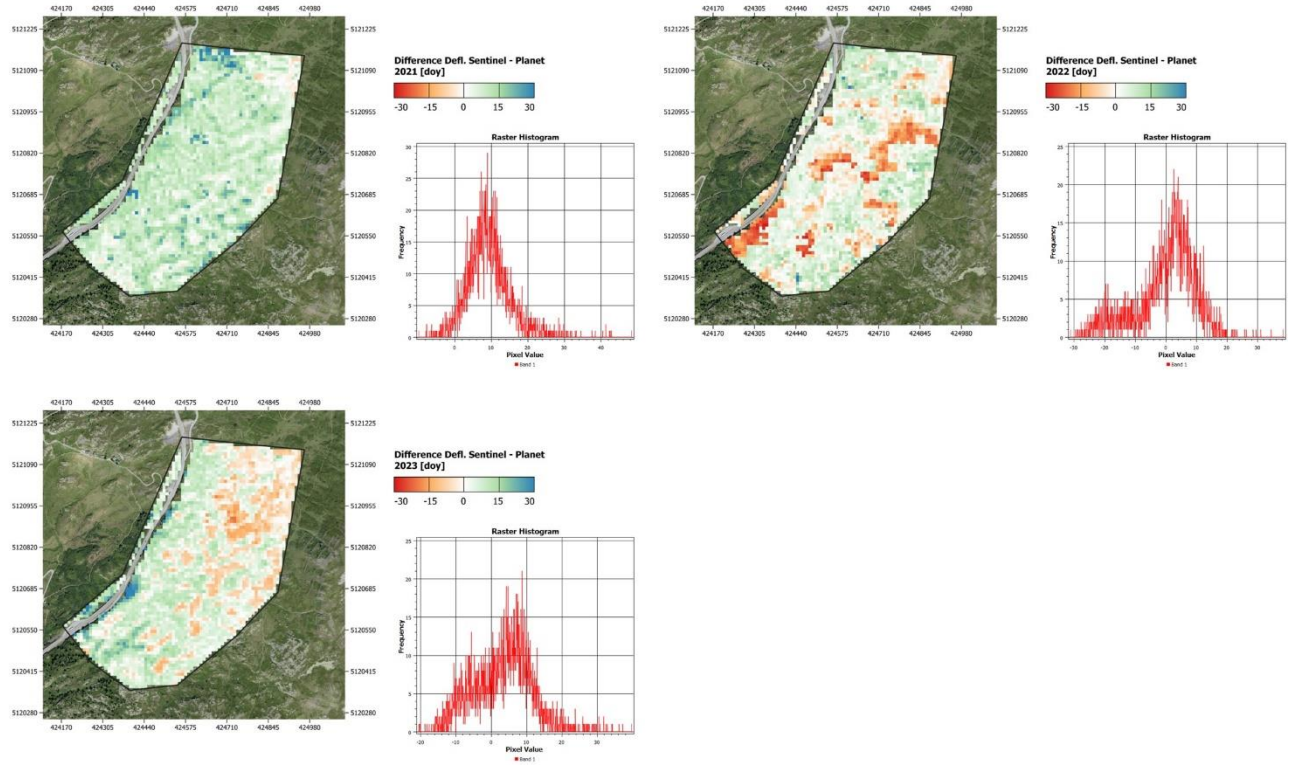

Figure 24 (a), (b) and (c) from top left to bottom left: Difference maps of Sentinel and Planet Start of Deflection for the years 2021, 2022 and 2023. Red indicates a negative difference, meaning that the Planet value was greater than the Sentinel-2 one, while green/blue corresponds to a positive difference and to a smaller Planet value.

In general, the histogram of 2021 has positive values, meaning that Sentinel set the Start of Deflection later in the year than Planet. The peak is located at 8 days and the tail is longer on the right side, suggesting that there are many pixels where the positive difference is more marked. These areas however are not tied to any particular surface feature, but they are the result of a few Sentinel time series having a late and sudden spike, which then leads to a late Start of Deflection. The majority of white pixels (which are related to similar estimations of Deflection) is associated to late starting areas in both Sentinel and Planet maps, meaning the biggest discrepancies are tied to early starting areas, which are usually given a higher Deflection value in the Sentinel-2 images.

As seen in chapter 3, 2021 was a year with higher precipitation and lower winter temperatures than 2022 and 2023, which resulted in a later Start of Deflection. Considering the late Start of Deflection identified by both sensors and the overall positive difference between estimation, it appears that the difference between the two sensors is greater in the case of a late starting year, which is tied to a prolonged snow melt which results in a spread-out period of vegetation activation. This is visible in the histograms of Figure 21 (d) and Figure 23 (a), which show a wider shape than the one of the other years.

Besides having the lowest mean difference value among the three years considered, 2022 has the peak at 4 days with many pixel values between -6 and -30. Meaning that both sensors set the Start of Deflection of the same pixels at similar timestamps, with some exceptions where the value of Sentinel was much smaller than the one of Planet.

This is related to the low precipitation and high temperatures experienced during the winter of 2022 resulting in an early Start of Deflection detected by both Sentinel-2 and SuperDove. This is associated to the temperatures and lack of precipitation which characterized 2022, as the climate conditions favored early snow melting and vegetation growth. Consequently, there was not a prolonged time interval of snow melting and vegetation growth, meaning that there was less room for setting the Start of Deflection at extremely different timestamps.

Therefore, similarly to the connection between a late starting year and a greater discrepancy in the Deflection estimation previously mentioned, the difference map of 2022 suggests a similar relationship between early starting years and Deflection consistency. However, it must be noted that the low value of the 2022 mean difference between Sentinel and Planet is misleading, as it was determined by the areas of extremely early Start of Deflection in the Sentinel image described in chapter 8.1.

Since these areas (visible in red in Figure 24 (b)) were found only in the Sentinel image, they resulted in a great negative value in the difference raster that ultimately shifted the mean difference towards a value close to 0, which a first glance would imply a greater consistency in the performance of the two sensors. If the curve fitting and the relative extraction of the Start of Deflection in the pixel mentioned above had been similar to the neighboring pixels, then the values of Sentinel-2 2022 map in said areas would have been more similar to the ones of Planet. This would result in a slightly greater mean difference value but also to a higher number of pixels shifted towards a difference value of 0, meaning that the consistency of the two sensors is actually higher than the histogram suggests. This indicates that Sentinel and Planet perform similarly in dry and warm years, where snowmelt and vegetation activity start early earlier than usual.

Regarding 2023, the histogram shows a similar shape to the one of 2022, with a peak between 6 and 8 days, a tail in the right part and a medium number of negative values. These are associated to larger Deflection values in the Planet image visible in Figure 25, which are in contrast to the ones of the Sentinel map.

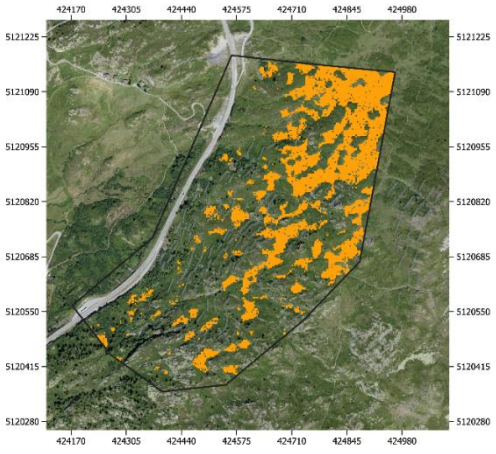

Figure 25: Planet 2023 Start of Deflection map, the orange pixels indicate the location of the second peak, while the rest were set as transparent.

The case of 2023 is further explored in chapter 8.3.1.4, as its characteristics offer a fitting example of the advantages and disadvantages of the different methods.

8.3.1.2. Sentinel-2 – RGB Drone

Figure 26 illustrates the three maps obtained by subtracting the snow melt maps created by Geoformer using the optical drone from Sentinel-2 Start of Deflection maps. The color schema and value interval of the color scale are the same as those used in the Sentinel-Planet Deflection difference analysis.

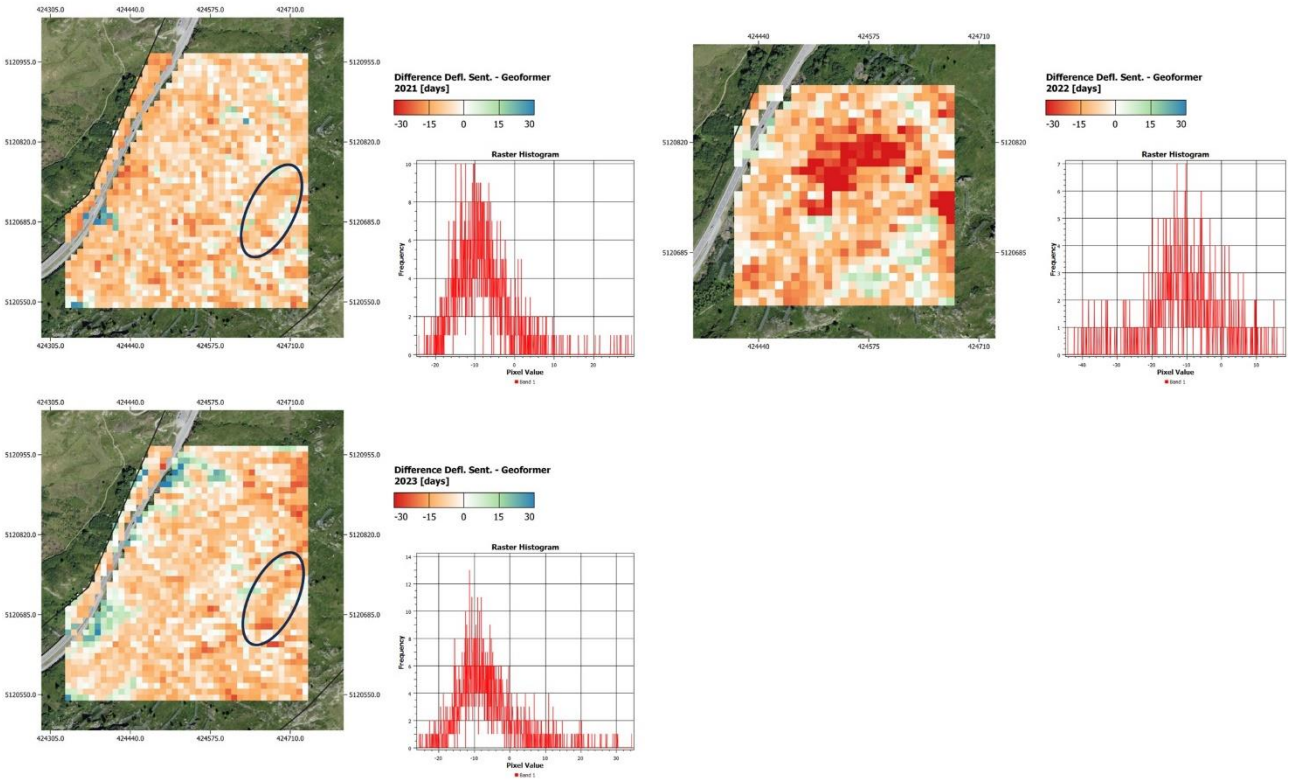

Figure 26 (a), (b) and (c) from top left to bottom left: Difference maps of Sentinel Start of Deflection and Geoformer melt maps for the years 2021, 2022 and 2023. Red indicates a negative difference, meaning that the RGB Drone value was greater than the Sentinel-2 one, while green/blue corresponds to a positive difference and to a smaller RGB Drone value. The black ellipse indicates a region where the difference between the estimations is the same.

The general tendency in all three cases is to have the majority of values on the negative side (red pixels in the images) with a histogram peak at -10 days. The tail is longer on the right side for 2021 and 2023, while for 2022 it extends left. The abundance of negative values suggests that the optical drone method usually sets the snow free day later in the year than the Sentinel derived Start of Deflection. It is not possible to associate any difference value to the topography or a particular surface feature. There are some areas in which the difference is constant over the years (black ellipse in Figure 26 (a) and (b)), however, it is not possible to relate them to anything but the spectral and resolution differences in the two methods.

There are still pixels where the difference is positive, the majority are located around the road with some exceptions inside the study area. There are only two pixels which have a positive difference value in every one of the three years, and they contain a mixture of rocks and grass. However, they are not the only pixels characterized by those features, therefore it is not possible not make any assumption regarding surface cover types and performance of the two methods. 2022 shows a higher number of extreme negative values concentrated in the center part of the image, these are related to the pixels with a particularly low Deflection value in the Sentinel image described in chapter 8.1.

8.3.1.3. SuperDove – RGB Drone

Figure 27 shows the difference maps of Planet Start of Deflection and Geoformer snow melt. The color schema and interval are the same used for the Sentinel-Geoformer comparison, meaning that the colors represent the same relationships as before.

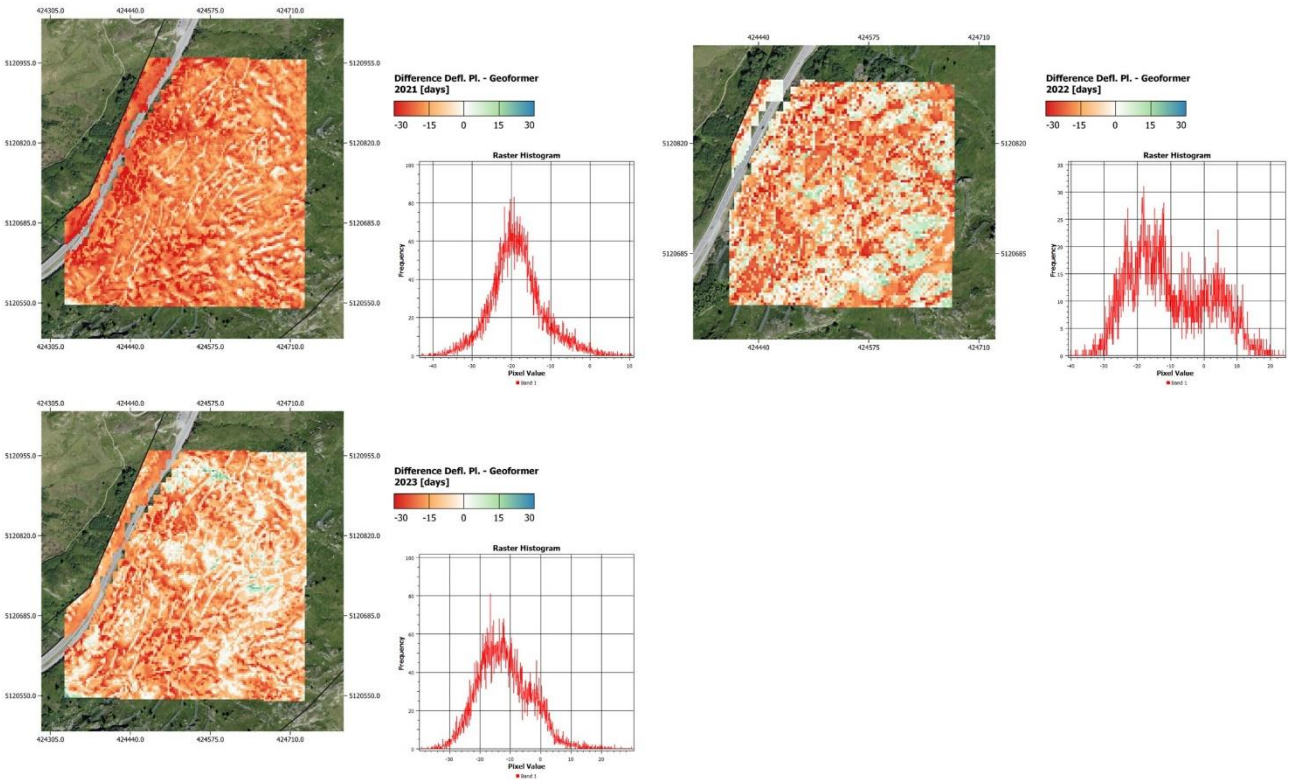

Figure 27 (a), (b) and (c) from top left to bottom left: Difference maps of Planet Start of Deflection and Geoformer melt maps for the years 2021, 2022 and 2023. Red indicates a negative difference, meaning that the RGB Drone value was greater than the SuperDove one, while green/blue corresponds to a positive difference and to a smaller RGB Drone value.

Similarly to what was observed with Sentinel, the tendency of Planet compared to Geoformer is to set the Deflection earlier in the year, resulting in the majority of difference values being on the negative side. As seen above however, the Deflection point set by Planet usually takes place before the Sentinel one, resulting in the negative Planet-Geoformer difference being even greater than the one between Sentinel and Geoformer. This difference is maximal in 2021, as almost every pixel has a negative value (there are some exceptions, as some bare rocks and snow nets have a slightly positive value). In 2022 the number of positive pixels is higher than in 2021 and 2023, meaning that Planet overestimation was more frequent. However, rather the being tied to winter weather, the positive difference value of 2022 is tied to two snowfalls which took place between the different drone surveys performed by Geoformer. The first one happened between the second (29.03.2022) and the third flight (04.04.2022), when snow melt was only visible in very few areas, while the second one occurred between the fifth (22.04.2022) and the sixth flight (28.04.2022), at a moment where the majority of areas had already experienced snow melt. As a consequence, the areas which were snow free before the snowfall events (which covered the entire area), were categorized as “not snow covered for the rest of the year”. This resulted in the first snow-free day of the year being set much earlier, which ultimately led to a positive difference with the Planet Deflection map.

The problem with this kind of situations also concerns the rest of the area, as there are zones where snow has not melted yet which saw their snow cover increase in height following a snowfall event. As a consequence, the first snow-free day is set much later than the one in areas which were snow free before the event, meaning that the snow melt falsely characterizes some pixels are particularly early/late melting.
Contrarily to the optical approach, the LSP workflow was not influenced by the late snowfalls (as the NDVI time series are interpolated), therefore the Deflection values remained unaltered, so that when the extreme drone pixels are subtracted from the Start of Deflection values, the resulting difference will be positive.
Regarding 2023, both the image and the histogram show similarities with 2021, with a prevalence of negative values with some positive exceptions. In this case however, the difference is less marked, as there are more white and green pixels, and the histogram is slightly shifted to the right. The greater number of positive values is not tied to Planet estimations, but on the classification of surface in the drone map. As displayed in Figure 28, some areas are characterized by the presence of trees, which can cast a shadow and reduce the reflectance of the snow underneath. As a result, these areas are set as snow free earlier than in reality, which will ultimately influence the difference map.

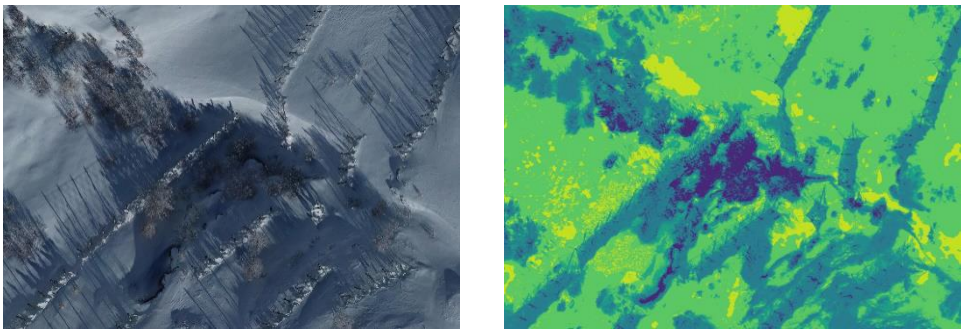

Figure 28 (a) and (b): Orthophoto of a portion of the Chalberweid area and snow melt map created using the optical drone. The colors of the image on the right indicate the moment of snowmelt: blue for early and light green/yellow for a late one.

Overall, the differences between Planet and Geoformer do not seem to be related to early/late starting areas, as was the case with the Sentinel-Planet relationship, on the contrary, they are more the consequence of the reliance on a few RGB drone images.

8.3.1.4. 2023 case focus and double peak identification

The next section covers the comparison between the Start of Deflection maps created using Sentinel-2 and SuperDove and the snow melt map derived from the optical drone, for the year 2023. The goal is to highlight the differences between maps which are useful to assess the performance and advantages of the three methods.

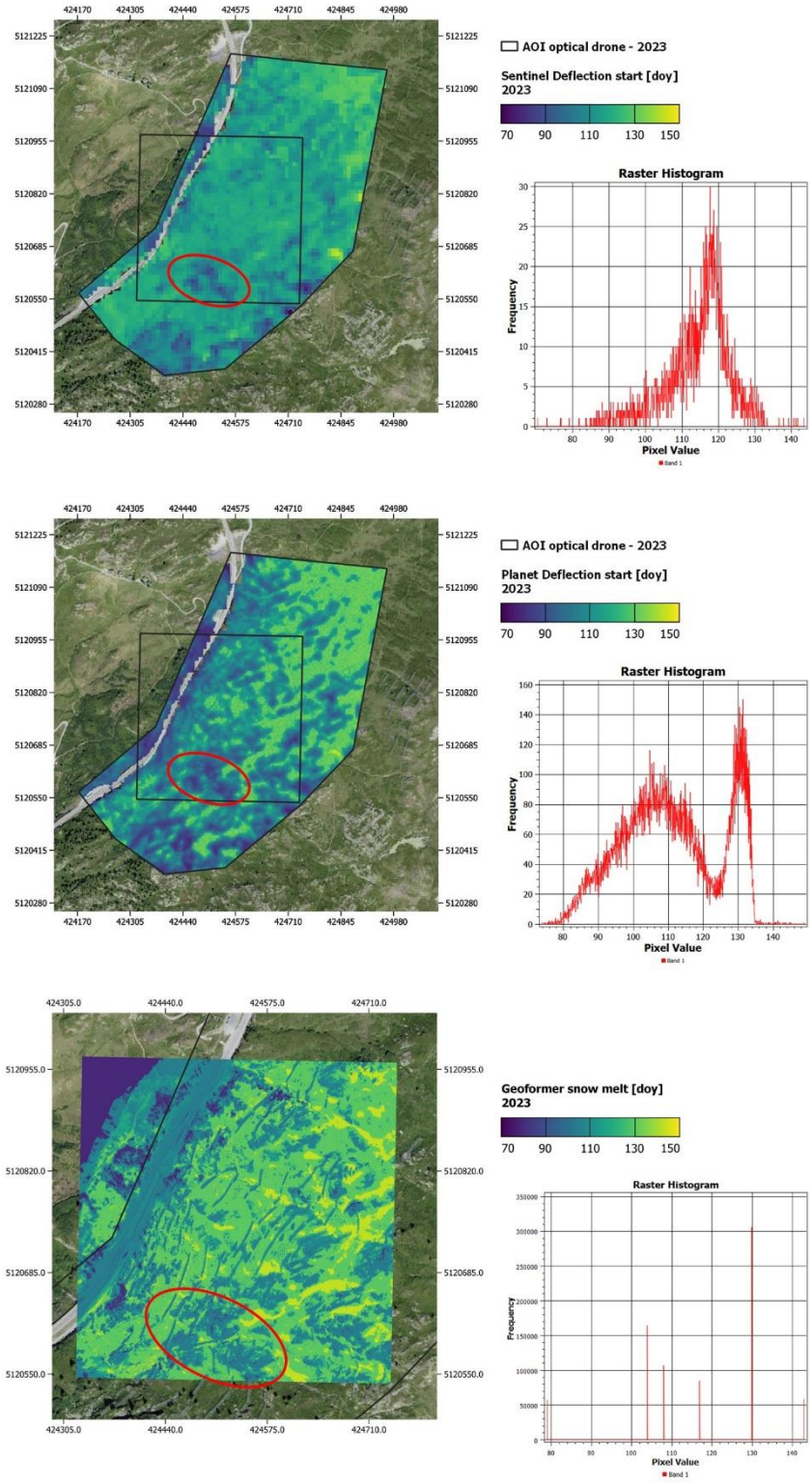

Figure 29 (a), (b) and (c) from top to bottom: Sentinel-2 and SuperDove Start of Deflection map for 2023 and Optical drone 2023 melt map.

Figure 29 (a) shows the Start of Deflection map created using Sentinel NDVI time series. In this case the majority of Deflection values are concentrated between 110 and 125, with some outliers on both sides. Despite the smooth appearance of the map, it is possible to distinguish some early and late starting areas. The central part of the image, however, is too homogeneous and no pattern is therefore identifiable.

The Planet Start of Deflection map, visible in Figure 29 (b), has a similar appearance to the Sentinel one, generally highlighting the same areas as early/late starting. In the case of Planet however, the separation between areas is clearer, it is therefore easier to associate the Start of Deflection to the terrain features. It appears that in 2023 the season started earlier in areas more exposed to wind and sunlight (hilltops and region surrounding the road). On the other hand, where the topography allows for a better snow deposit and conservation (small valleys) the Deflection started later.

The color of the Planet and Sentinel images are more similar on the upper most right part of the study area, where the shade of green of the Sentinel pixels is lighter than the one predominant in the other parts of the image, and almost matches the one of Planet. For the majority of the area however, the Sentinel map has a much smoother appearance than the Planet one, especially in the center part, where the homogeneous appearance does not allow the identification of any pattern.

Figure 29 (c) shows the optical UAV snow cover map. Despite being based on a different approach, i.e., one that does not rely on vegetation activity, the areas highlighted are similar to the ones that can be found on the Planet map (and to a certain measure in the Sentinel one).

The red ellipses found in each of the three images mark an area where the pixels have been consistently identified as early Deflection starting and early melting respectively. The highlighted area in the lower part of the image is characterized by steep rock formations, i.e., surfaces where snow tends to accumulate less, and vegetation struggles to grow (which means a prevalence of low vegetation rather than high standing trees). This means that in this case, the consistency shown between the three methods is tied to the shorter growing phase of the less productive vegetation (Gómez-Mendoza et al., 2008) which grows on steep rock and the smaller snow deposits in the same areas.

Overall, the Planet and Drone maps showed major similarities, mainly in early melting/deflecting areas. The greatest differences are found in the central part of the drone image, where there is a higher number of late starting pixels than in the same part of the Planet image. This is realistically tied to the small number of drone images available, which failed to identify the different melting rates of snow, resulting in the overestimation of the snow melt event which took place around day 130 (Figure 29 (c)).

Comparing the three histograms further allows to highlight the differences between the three methods. Even though the images bear similarities, the histograms show different shapes and distributions, especially when comparing the Drone and the Planet one to Sentinel. The latter follows a slightly left skewed normal distribution with a single peak around day 116. In the case of Planet, the histogram is double peaked, having a first one at day 105 and a second one, more pronounced, around day 132. Lastly, despite not having continuous values, the drone histogram shows the same two peaks as the Planet one, the first at day 104 and the second at

day 130, which ultimately suggests that both the SuperDove and the Phantom 4 were able to identify surface dynamics unobserved by Sentinel. This is observed in the position of the peaks in the histograms of the three images. As seen in Figure 29, the Sentinel one is located between those of Planet and the drone, resulting in an averaging effect that renders the image difficult to interpret. This failure to identify different Start of Deflections is tied to the lower spatial resolution of Sentinel-2, which results in a higher number of mixed pixels (Helfenstein et al., 2022) containing both areas of early and late deflection, which get averaged.
Overall, in 2023 the Planet and Optical Drone maps showed a high consistency, being able to better distinguish early starting zones from late ones. On the other hand, Sentinel-2 failed to do the same, as the lower spatial resolution and the resulting greater number of mixed pixels resulted in a smoothed image.

8.3.2. Differences in pattern identification

Figure 30 shows the average normalized Start of Deflection maps created using Sentinel and Planet data, both in two and three dimensions. The 3D view was obtained by projecting the two maps over the Digital Surface Model created using the images of the third flight performed using the Mavic 3M. The objective is to determine whether the two satellites always identify the same areas as early/late starting, and if the eventual differences/similarities can be related to topography.

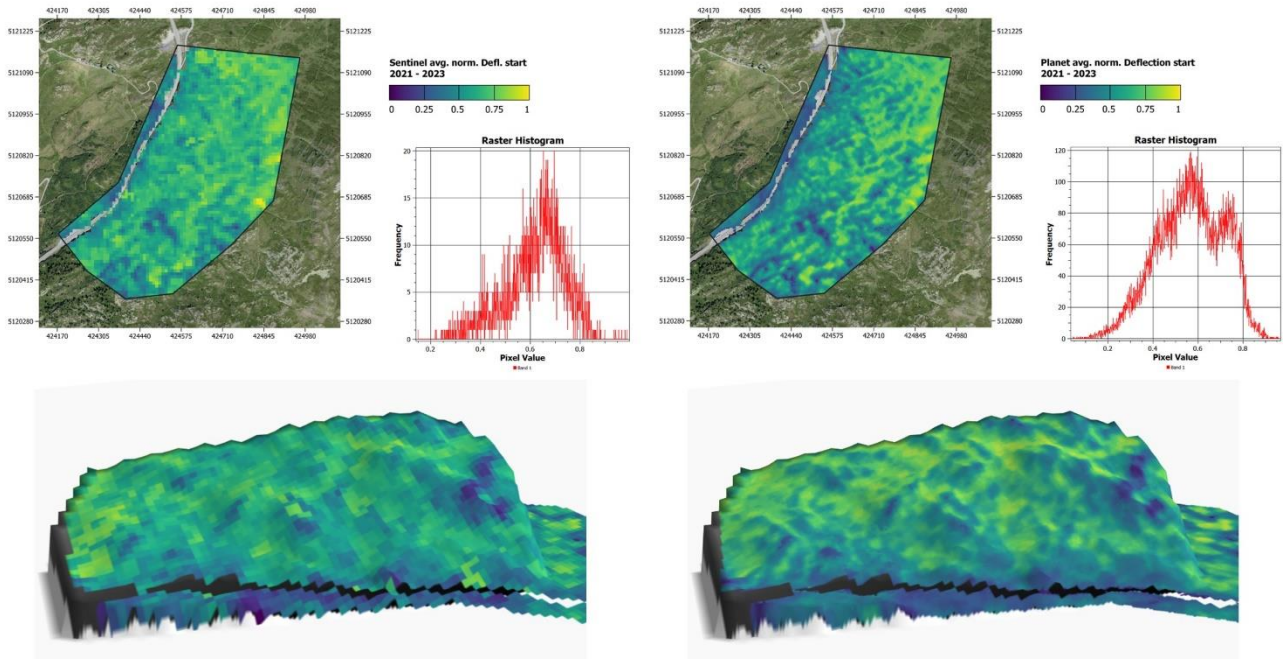

Figure 30 (a), (b), (c) and (d) from top left to bottom right: Average normalized Start of Deflection map for Sentinel and Planet for 2023. The first two images are in 2D while in the second two the raster have been projected over the DSM created using the Mavic 3M. Blue pixels indicate early Deflection zones, while green ones are associated to late deflecting one.

At first glance the two maps appear to be quite different, with Sentinel-2 producing much more inaccurate results than Planet, especially in the center part of the study area, where the terrain is more complex. However, a second look reveals how the classification of pixels was similar, as most areas visible in the Planet image

can be found in the Sentinel one. The best example is visible in the upper right part of the two maps, where the small valley has been characterized as late starting (light green) while the surrounding hills and rock formations as early starting (dark green/blue). The major difference between the two images is related to how distinguishable the different areas are, and how well they can be related to topography. Even though the same areas can be found in both maps, they are much more visible in the Planet image, meaning that the sensor did a better job at separating early and late starting areas. Observing the Planet image reveals that in general, the late Deflecting pixels are found in terrain depressions or in areas where the terrain in less complex, while late starting ones are usually associated to hilltops, rock formations and generally exposed areas.

The disparities between sensors can also be observed in the two histograms shown in Figure 30, which display two very different shapes. The one of Sentinel-2 is slightly left skewed, with a single peak at 0.65/0.70 and with the majority of values between 0.5 and 0.8. On the other hand, the SuperDove one has a wider shape, with the values being mainly located between 0.3 and 0.8 and with two peaks, one at 0.55 and one at 0.75. Based on what was determined in the single year analysis previously described, it can be assumed that on average, Planet better separated pixel with an early Start of Deflection from those with a late one. Similarly to what was observed in chapter 8.3.1.4, the lower spatial resolution of Sentinel-2 resulted in a mixed-pixel-derived averaging effect, which led to an image with a smooth appearance and to a consequent interpretation of Deflection values harder than in the case of Planet.

The inconsistencies can be further explored by calculating the difference between maps, which can illustrate where the biggest differences in average Deflection estimations are located.

Figure 31 illustrates the map obtained by subtracting the average normalized Start of Deflection calculated using Planet from the Sentinel one.

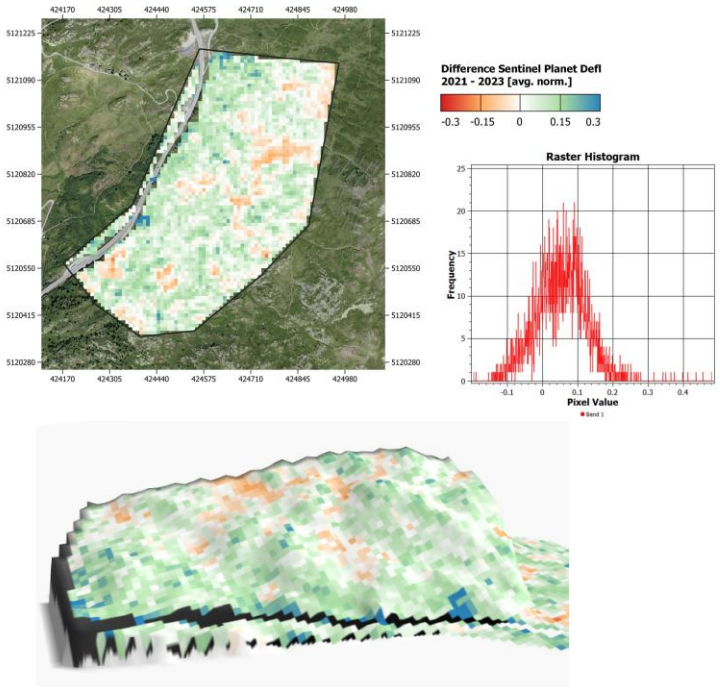

Figure 31 (a) and (b): Map showing the difference between Sentinel and Planet average normalized Start of Deflection. For the 3D view the raster has been projected over the DSM created using the Mavic 3M. Red indicates a negative difference, while green/blue corresponds to a positive one.

The color scheme is the same one first used in chapter 8.3.1, which assigns red and blue to a negative and positive difference respectively. However, contrarily to the single years analysis, a negative difference does not imply that one sensor defined a pixel as an early starting while the other set it as late starting, but it rather indicates a difference in the magnitude of estimations. Considering for example two average values for the same pixel in the Planet and Sentinel images, the first is 0.9 while the second is 0.8, both of which correspond to a late start. In the difference map the pixel will have a value of -0.1, which indicates that on average, the pixel is set later in the Planet image than it is in the Sentinel one. Therefore, a positive or negative value could indicate systematic over and underestimation by the two satellites.

The map was then projected over the DSM created using the Mavic 3M images previously mentioned.

As can be seen in the map and histogram shown in Figure 31, the majority of pixels has a positive value, with some negative exceptions mostly located in the upper right part of the study area. This suggests that for most pixels, the average normalized Deflection calculated with Planet is smaller than the one derived from Sentinel. This is a direct consequence of what was previously observed regarding Sentinel averaging the Deflection values, which resulted in a smoothing effect and the differences shown in Figure 31. It must be noted the during the normalization process, the few outliers present were not excluded, meaning that the pixels with an extreme early Start of Deflection value of Sentinel 2022 image (dark blue pixels in Figure 21 (e)) and the extreme late ones of 2021 (bright yellow in Figure 21 (d)) influenced the final normalized value of every other pixel in the images. This is visible in the bright blue pixels close to the road in Figure 31, which are the consequence of the extremely late 2021 pixels previously mentioned.

It can also be noted that the vast majority of negative values (red in Figure 31) occur in late starting areas, while the few extreme positive ones (blue in Figure 31), excluding the ones tied to the 2021 image, are associated to early starting pixels. Consistently to what was previously observed, the negative difference is tied to late starting areas being identified by Planet but not by Sentinel, which, having smoothed the values, are characterized by smaller normalized values.

8.3.2.1. Differences between average Deflection and Geoformer melt maps

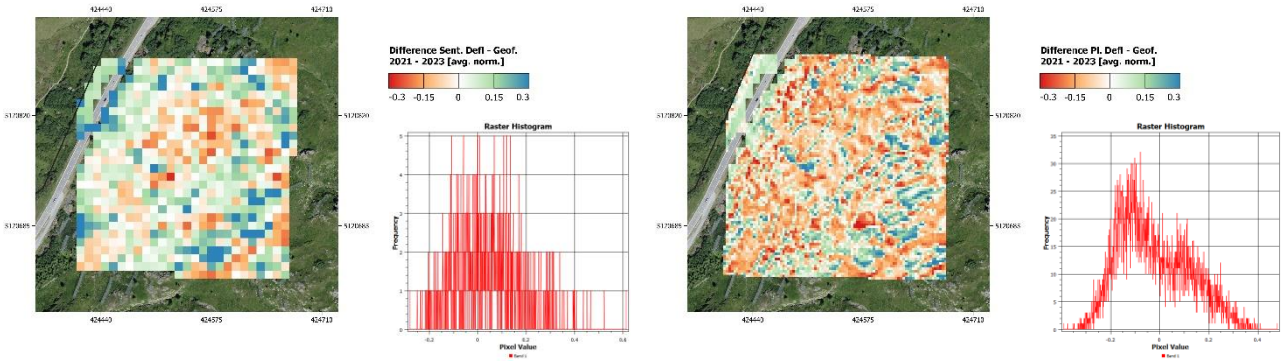

Figure 32 (a) and (b): on the left is the difference between Sentinel average normalized Start of Deflection and Geoformer average normalized melt map, on the right the same difference but between Planet and Geoformer. Red indicates a negative difference, while green/blue corresponds to a positive one.

Even though the two products are based on different principles, the average Start of Deflection maps created using Sentinel and Planet can be compared to the snow melt map obtained with the optical drone, as both offer a qualitative indication of early/late melt/Deflection, rather than a specific number. Figure 32 shows the maps obtained by subtracting the average normalized snow melt map obtained with the UAV from the Satellite-derived average normalized Start of Deflection map.

Figure 32 (a) does not show any particular pattern related to topography or other features, as the positive and negative pixels are mainly determined by the values of the Drone image. This is related to the smooth appearance of the Sentinel map mentioned in the previous chapters, which is a direct consequence of the lower spatial resolution. Therefore, the pixels characterized by a negative difference (red in Figure 32) are associated to a later snow melt in the drone raster, while those with a positive difference are tied to early melting areas.

The greater concentration of positive values around the road is related to Sentinel pixels containing a mixture of snow free (road and its edges) and snow-covered areas (which result in a later Deflection start), while in the case of Geoformer the same road and its proximities are usually marked as not snow-covered already during the first survey.

In the case of the difference between the SuperDove and the optical drone, the different areas are much better distinguishable, which is tied to the higher spatial resolution of the satellite images. Similarly to what was observed for Sentinel, the pixels characterized by a negative difference are located in late starting areas, while the positive values corresponding to early starting ones.

Similarly to what was presented in chapter 8.3.2, even though both methods set the same areas as the ones where snow melts last/where the Deflection starts latest, the resulting difference has a great negative value. This can happen for different reasons. The first one is already mentioned in chapter 8.3.2 and is tied to the normalization process. As visible in Figure 32, the area covered by the drone map is much smaller than the satellite ones, meaning a lower number of pixels and a lower probability of having extremely different snow melt values. This contrasts the much bigger size of the satellite images and the consequent higher probability of having the pixels with the minimum and maximum value outside the common area, which results in the

normalized value located in the drone area being closer to each other. The second reason is tied to the principles on which the two methods are based. The Land Surface Phenology workflow analyzes each pixel individually, meaning that if an area large enough to be identified by the Satellite experiences an increase in vegetation activity (and therefore in NDVI values), then the Deflection value will be calculated. On the other hand, the optical drone method is based on the difference between snow cover images, meaning that a map gets created once there are enough visible differences, i.e., when snow has melted on surfaces big enough. This leads to smaller, early snow free areas not being detected and to snow free doy being much closer to each other than the Start of Deflection values are. The third reason is that the areas highlighted in the two images do not exactly overlap, which can be the result of either the different resolution of the three sensors, a consequence of resampling or simply of differences in the measurements.

Figure 33 shows the average normalized Start of Deflection calculated using Planet (left), the average normalized snow melt derived from the optical UAV resampled to Planet (middle) and the difference raster between the two (right).

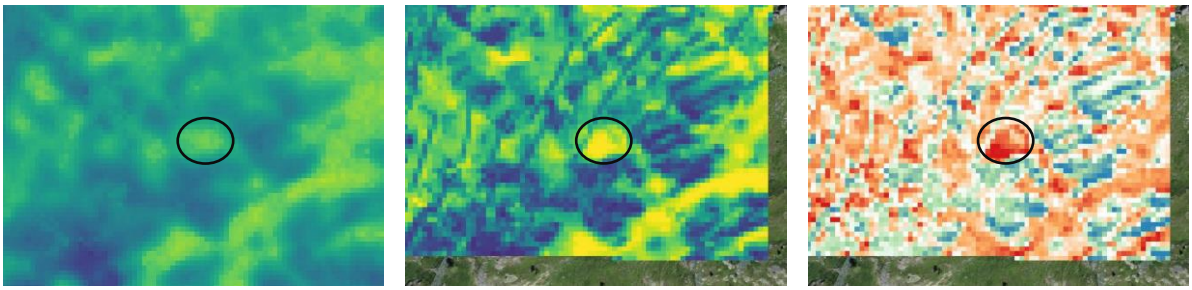

Figure 33 (a), (b) and (c): Closeup of SuperDove average normalized Start of Deflection map, closeup of the Phantom 4 average normalized snow melt map, and difference between the two, where red indicates a negative difference, while green/blue corresponds to a positive one.

The red areas in Figure 33 (c) suggest an inconsistency between the estimation of Planet and the optical drone, with the former setting Start of Deflection values either earlier or later than the snow melt detected by the UAV. Looking at Figure 33 (b) and (c) however, reveals how the areas highlighted by the two methods are the same. This is visible for example in the right part of the two images, with a line of early starting pixels going from the center-right to lower-center area, or in the early starting pixels surrounding the black circle.

In the image displaying the difference between Planet and Geoformer it is possible to clearly see straight blue lines indicating that the Start of Deflection calculated with Planet usually happens much later than the moment of snow free surface set with the optical drone. These lines are associated to snow nets and are easily identifiable in the difference raster due to being visible in the Geoformer images but not in the Planet and Sentinel ones. This is related to the methodology involved in the creation of the maps. Snow nets are clearly distinguishable in RGB drone images, and since the Geoformer approach is based exclusively on RGB products, snow nets will be a noticeable element in the final maps. On the other hand, they are not a dominant feature in Planet images (they are slightly distinguishable in the RGB image but go unnoticed in the NIR band) and are completely undetected in both Sentinel and Landsat images. Since snow nets cast a shadow, the area beneath them results in being set as snow free even though it is not, leading to extremely high differences

compared to the Planet Deflection estimations. It can be noted that snow nets are not visible in the difference image with Sentinel, which is due to the extremely high degree of resampling (5 cm to 10m) of the drone image.

In conclusion, it appears that the two methods highlighted the same areas, however, due to the difference in the normalization area and calculation of Deflection/snowmelt, the Planet map overestimated the value of early starting areas and underestimated the one of late starting pixels compared to the optical UAV.

8.4. NDVI snow maps

In the following chapters, the different snow maps obtained following the process described in chapter 6.2 are described. The first part covers the single day snow cover maps created using the images captured by the Mavic 3M, then, both yearly and average NDVI melt maps for both Sentinel and SuperDove. Finally, every map is compared to the daily snow cover and yearly melt maps created by Geoformer using the optical UAV.

8.4.1. Single day multispectral drone snow cover maps

Figure 34 shows the single day snow cover maps created using the images captured by the Mavic 3M during the flight of April 18th, 2023. The map at the top depicts the classification of surface features in "snow" or "not snow" determined by a threshold NDVI value (Green vertical line in the histogram of Figure 34 (a)), while Figure 34 (b) serves the same purpose but in this case NDVI was calculated using the Red-Edge band instead of the Red one (NDVIe). In the second map, two threshold values were used, as the frequency histogram displayed a second smaller peak after the main one.

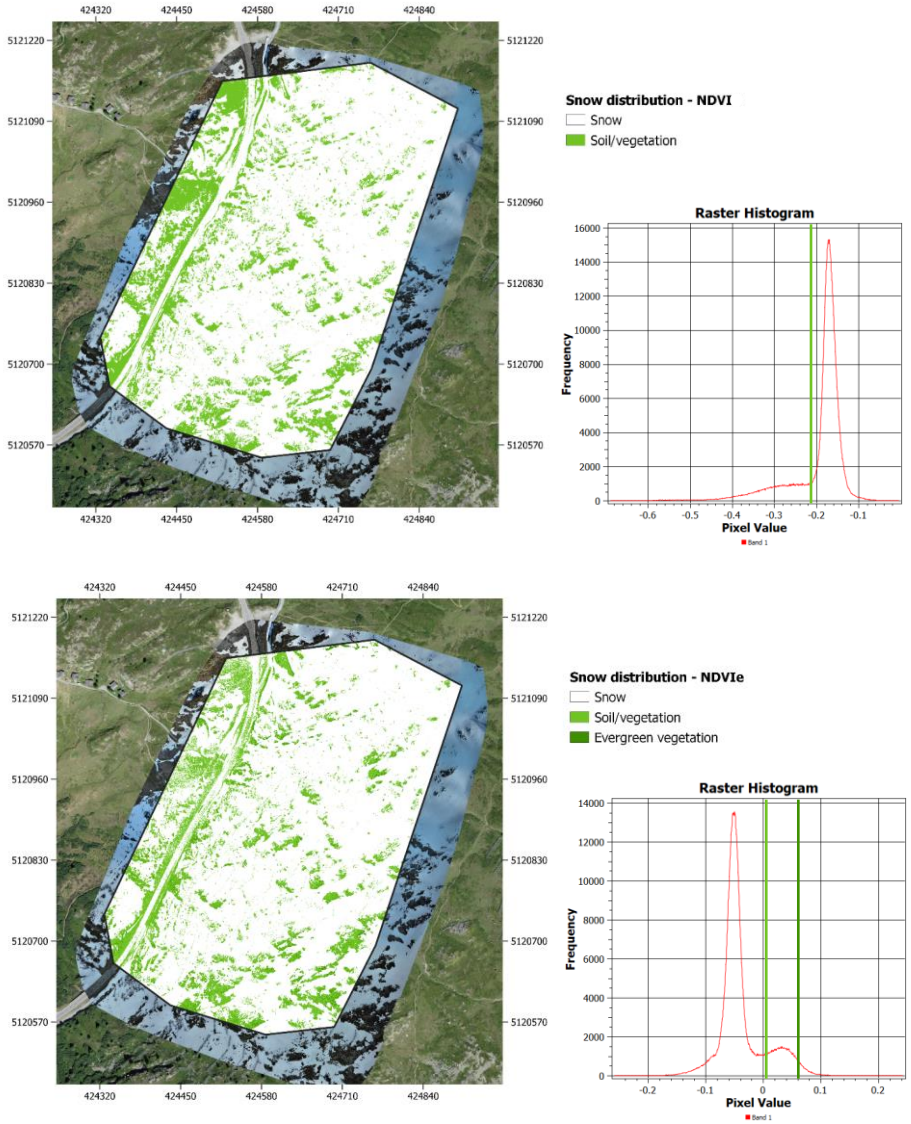

Figure 34 (a) and (b): Snow cover maps created using NDVI images captured during the flight of April 18th, 2023. The image on top is derived from Red-based NDVI, while the one at the bottom is based on NDVI calculated using the Red-Edge channel. In both maps white indicates the presence of snow and green is associated with soil and vegetation

In both images snow pixels are white colored, while every other surface cover type is green. In the NDVIe map however, another shade of green is added. These pixels have a higher NDVIe value and are associated to a higher Red-Edge reflectance, meaning that they contain green vegetation photosynthetically active (Xu et al., 2019).

At first glance the two maps have a similar appearance, having generally highlighted the same areas as snow or not snow. The major differences are found in the areas on the left side of the road and on the vegetation-covered parts of rocks.

The different classification of the roadside portion is shown in Figure 35, which illustrates the aerial view (b) against the NDVI (a) and NDVIe (c) snow cover map. In this area the mixture of bare soil, small rocks and gravel has the same NDVIe value as snow and is therefore classified as such.

Figure 35 (a), (b) and (c): Snow cover map created using Red derived NDVI, aerial view and Red-Edge derived snow cover map.

Regarding the differences observed on rock patches covered by vegetation, the NDVIe map generally better separated these features from snow, while also highlighting perennial vegetation located on top of rocks. This is visible in Figure 36, which shows the snow cover map created sing NDVI (a) and the one derived from NDVIe. This difference in classification is related to the reflectance values of the Red and Red-Edge channel in the case of bare rock, as the low Red value results in an NDVI close to the one of snow. On the contrary, Red-Edge has a higher rock reflectance, close to the one of the NIR channel, meaning that the final NDVIe will have a value close to zero and will be easier to separate from the rest (see Figure 34 (b)).

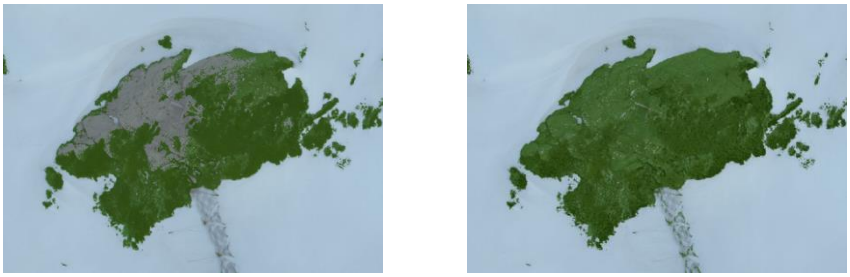

Figure 36 (a) and (b): NDVI and NDVIe snow cover maps visualized over the aerial image.

While displaying a similar accuracy in most areas, the two maps showed some discrepancies where the reflectance differences between the Red and the Red-Edge channel are noticeable. These areas mainly include bare soil mixed with gravel and the vegetation-free parts of rocks. Considering the performance inside the area

where the reforestation project has its focus (therefore excluding the parts surrounding the road), using the Red-Edge edge channel proves to give an advantage in identifying both snow free patches and low active vegetation.

In the next chapter, the two NDVI maps will be compared to a single day snow cover map created using images taken the same day but using the DJI Phantom 4 (optical UAV). The goal is to show if using the NIR channel (and the Red-Edge one) has an advantage over normal RGB imagery.

8.4.1.1. Comparison with RGB snow cover maps

Figure 37 displays a closeup of polygon 01 displaying the aerial view (top-left) and the snow maps created using RGB images (top-right), NDVI (bottom-left) NDVIe (bottom-right). As seen in chapter 8.4.1, the two NDVI maps showed an almost identical classification, with the main exceptions regarding soil mixtures and low vegetation. On the other hand, the RGB map has many differences compared to both the aerial view and the two NDVI maps. The most noticeable ones are the overestimation of snow free areas around the edges of rocks and below snow nets and wooden tripods.

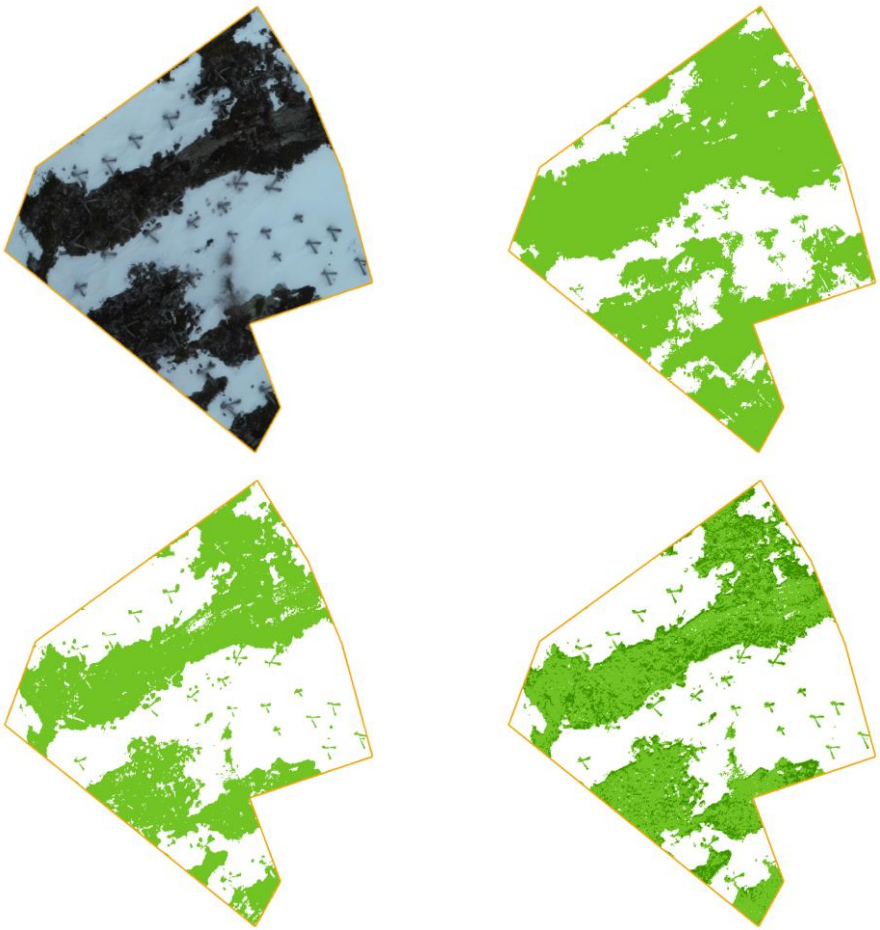

Figure 37 (a), (b), (c) and (d) from top left to bottom right: Closeup of polygon 01 of the aerial map, RGB, NDVI and NDVIe snow cover map. In the snow maps white indicates snow, and green soil/vegetation.

Figure 38 shows the difference between the snow cover maps of April 18th created using the DJI Phantom 4 (optical drone) and the Mavic 3M (multispectral). Areas colored in white are those identified as snow by both methods while the ones in green have consistently been categorized as not-snow (vegetation, bare soil, and the road in the case of the Phantom 4). The pixels set as non-snow by the Phantom 4 and snow by the Mavic 3M are orange colored while for the other way around (Snow Phantom, not-snow Mavic) the color is red.

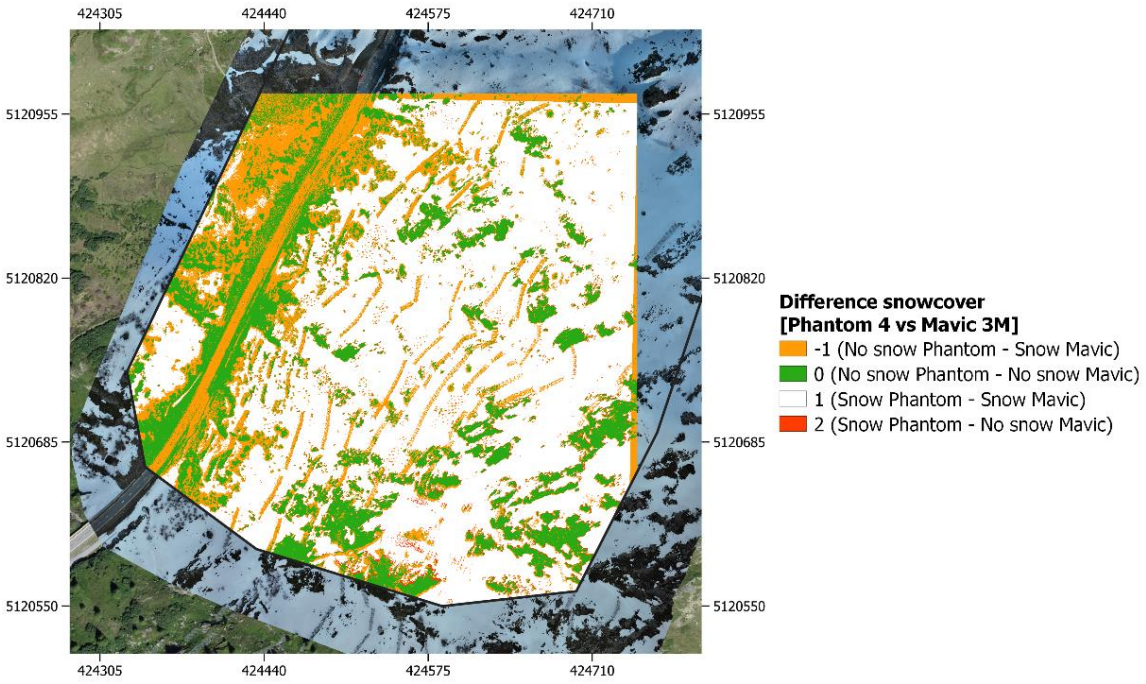

Figure 38: Map showing the difference between the RGB and the NDVIe snow cover maps. Orange pixels are related to snow in the Multispectral drone map but not in the optical one, green indicates soil/vegetation in both maps, white indicates snow in both maps and red is associated to snow in the optical map but not in the multispectral one.

In general, the biggest discrepancies are found at the edges of snow free areas, on the gravel covered areas overlooking the road and lastly along snow nets. As seen both above and in the image below, the optical derived snow cover image often overestimated the extent of snow free areas, especially around small trees and bushes and on the edges of rock patches. On the other hand, the Phantom 4 correctly characterized the road section and the gravel area, meaning that the difference is derived from the Mavic 3M map. Due to the cast shadow and overall lower reflectance, snow nets and the surface below them are marked as not snow in the optical map. On the contrary, the NDVIe image was able to identify the snow below the nets, which led to the inconsistencies shown in the difference image.

There are also two orange sections on the upper and right borders of the image, which are tied to the alignment process necessary to compare the two datasets.

It must be noted that the referencing error experienced during the first flight greatly influences both the accuracy of the NDVIe snow map and of the difference image. This is visible in Figure 39, where the wooden structures are shifted right in the NDVIe image, resulting in what appears to be an inconsistency between the two methods.

Figure 39: closeup of the map shown in Figure 20 highlighting an area of discrepancy between RGB and NDVIe. The color scheme is the same one used in Figure 38.

Finally, there is only a handful of areas identified as not snow by the Infrared drone and as snow by the optical one (red color). These are more prominent in the lower part of the image and are tied to the slight shift in the referencing between the two original maps.

Overall, the two maps showed a better uniformity on the right part of the study area, where the terrain is more sloped, and the surface elements are snow and bare rocks. On the other hand, the greater discrepancies are found in areas where the NDVIe value of soil and gravel resembles the one of snow and in zones where the surface brightness is particularly low, such as around vegetation and below snow nets.

In general, the RGB approach has shown reduced accuracy in areas characterized by low vegetation, where cast shadows decrease snow reflectance. As a result, these parts are indicated as snow-free, when in reality snow is still present. A similar effect can be observed around the wooden structures and snow nets.

In general, creating a snow map using RGB images requires more specific and rare conditions than using NDVI and NDVIe. These are high illumination to be able to better distinguish features, well defined snow-no snow border and the absence of shadow casting elements such as snow nets, wooden tripods, and vegetation. Conditions such as the ones previously mentioned are rarely observed, thus resulting in a decreased accuracy of the analysis, mainly under the form of underestimation of snow cover.

The snow cover map derived from NDVI values showed a more precise distinction between snow and other surface types than the RGB one. However, it lacked accuracy compared to NDVIe, especially in the case of bare rocks, where the calculated NDVI was particularly close to the one of snow.

8.4.2. Sentinel-2 NDVI snow melt maps

Figure 40 shows the results obtained after following the workflow presented in chapter 6.2. The first three images display the snow melt maps created using Sentinel-2 derived NDVI, while the fourth one (Figure 32 (d)) is the average normalized snowmelt for the three years. The color scheme is the same one for all four maps while the value interval is constant only for the first three maps, as the fourth one is normalized between 0 and 1. Similarly to the principle presented in chapter 8.1, the different colors are associated to an early (dark blue) or late (light cyan) event, in this case, rather than vegetation activity, the maps directly display snow melt. Another noticeable difference from the Start of Deflection maps is that values are not continuous, as the maps were created with usually 5-6 images, meaning that a snow melt doy value can be associated to only one of the few used images.

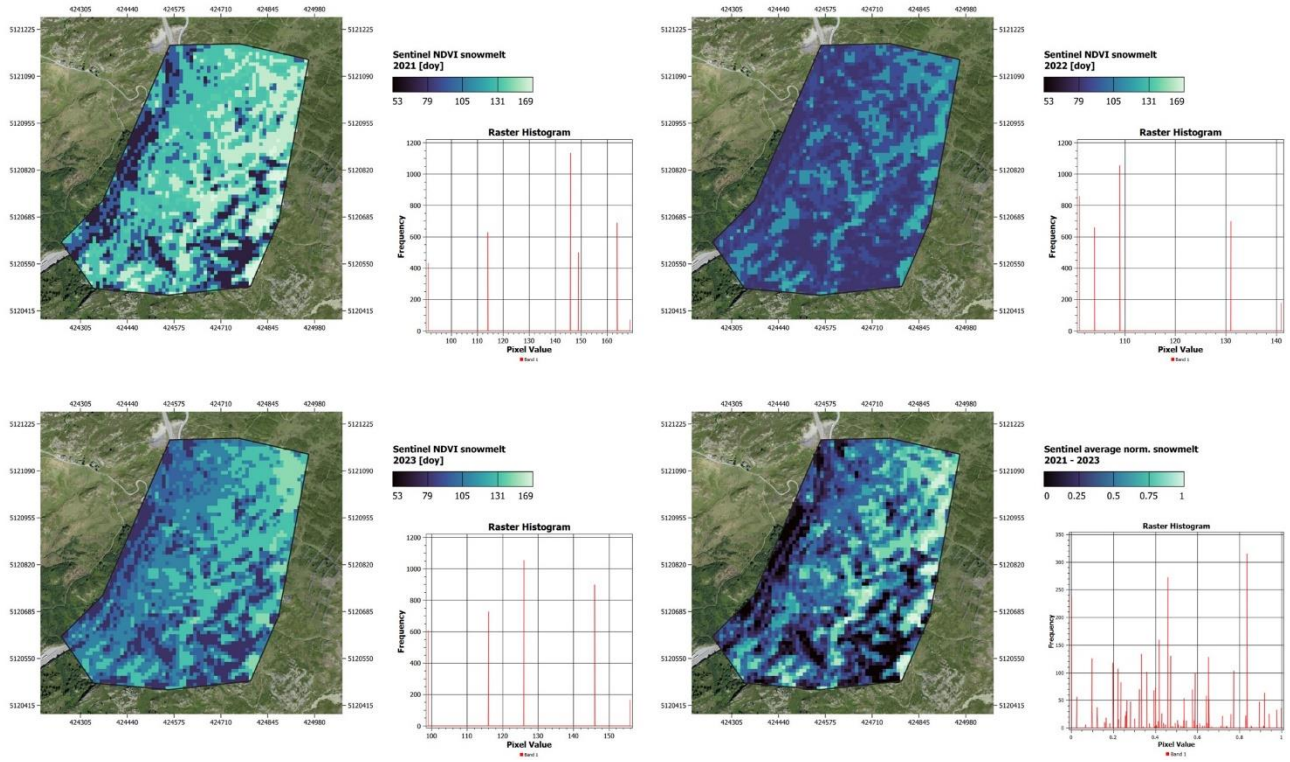

Figure 40 (a), (b), (c) and (d) from top left to bottom right: Sentinel-2 NDVI snow melt map of 2021, 2022 and 2023 with the addition of the average normalized snow melt for the three years. Dark shades of blue indicate an early melting area, while light cyan in associated with late melting.

Overall, the three rasters show continuity to the Start of Deflection maps analyzed in chapter 8.1, as they can be associated to winter weather in the same way. 2021 is characterized by late snowmelt, with the majority of surfaces being snow free after day 146 (associated to lighter shades of cyan) with some minor areas of early melt around the road and on the southern parts of the study area, which are often but not always characterized by bare rocks. The histogram is not as continuous as the Deflection, therefore, it is harder to highlight eventual peaks. In the case of 2021 there appears to be one on day 146, with no other noticeable features. The map of 2022 shows much darker colors than the 2021 one, meaning that snow melt took place noticeably earlier. The pixel values and the histogram indicate that in 2022 the area was completely snow free by day 142, which is

considerably earlier than the 2021 snow melt phase, which, as previously mentioned, saw its main phase around and after day 146. As seen in chapter 3, 2022 was an exceptional year both in terms of high temperatures and low precipitation and the consequent early Start of Deflection determined by the LSP workflow is reflected by early snow melt identified by the NDVI snow maps. 2023 on the other hand, appears to be the middle ground between 2021 and 2022, both visually and in terms of snow melt doy. The map has prevalence on neutral shades of blue, which are in contrast to the light ones of 2021 and the darker of 2022, thus implying that the main phase of the snow melt event took place earlier than in 2021 but later than in 2022. This reflects the weather experienced during the winter of 2023, which was characterized by similar precipitation to 2022 but overall lower temperatures.

Finally, Figure 40 (d) displays the average normalized snow melt derived from the three yearly snow melt maps. Similarly to the other rasters, the different shades of blue are associated with an early or late snow melt. In the case of the average normalized however, the values of the pixel indicate general trends in the melting pattern, meaning that they can give information on where snow usually melts first, independently of the weather experienced during the year.

8.4.3. SuperDove snow melt maps

Figure 41 displays the snow melt maps created using Planet NDVI images. The first three cover the melting process for 2021, 2022 and 2023, while the fourth, averaged normalized one represents in which zones snow usually melts first.

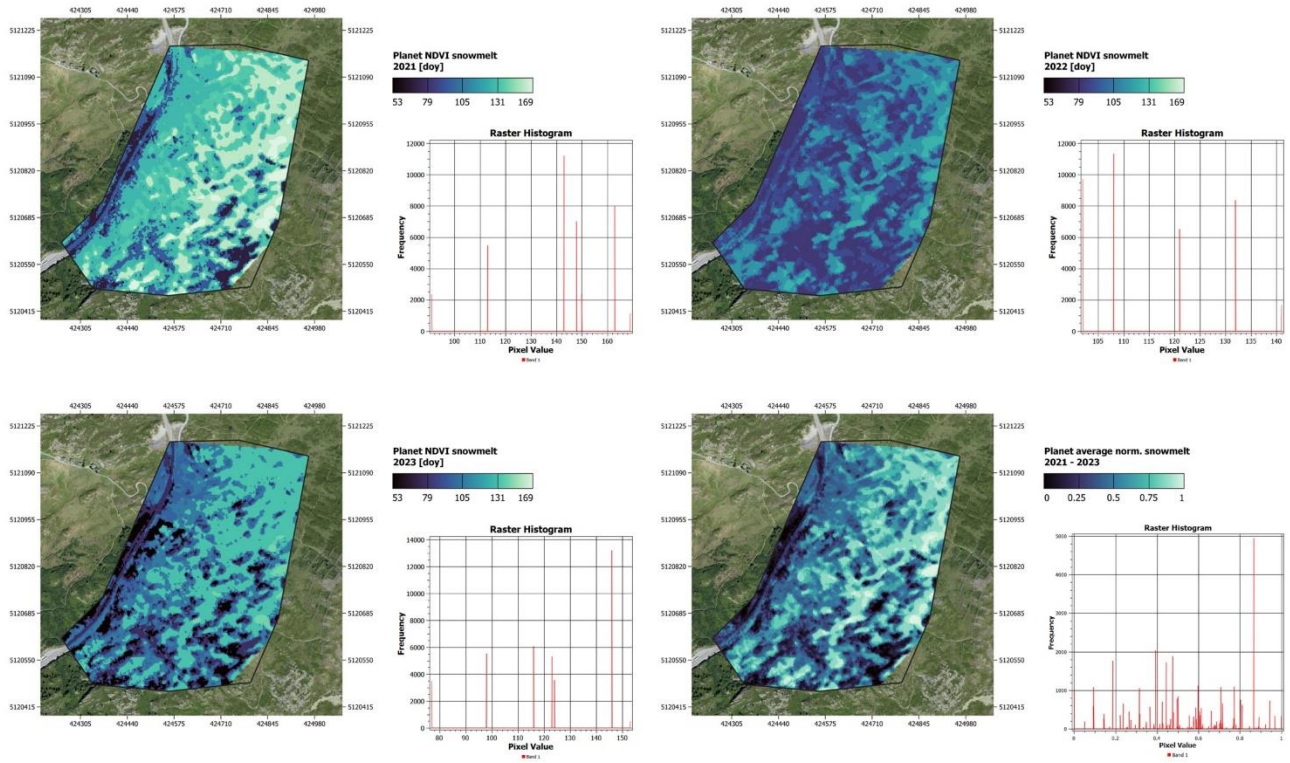

Figure 41 (a), (b), (c) and (d) from top left to bottom right: SuperDove NDVI snow melt map of 2021, 2022 and 2023 with the addition of the average normalized snow melt for the three years. Dark shades of blue indicate an early melting area, while light cyan in associated with late melting.

Overall, the Planet maps have a similar appearance to the Sentinel-2 ones, displaying a prevalence of brighter shades of blue in 2021, associated to a generally late melting, darker colors in 2022, which are related to the exceptionally dry and warm winter, and more neutral shades in 2023, tied to the low precipitation and low temperatures experienced at the beginning of the year.

The average normalized map characterized areas similarly to what seen with Sentinel-2, with the major difference being that the increased spatial resolution led to an easier separation between early and late melting areas and consequently to a better association of snow melt to topography and nature elements. The areas related to an early melting event, dark blue in Figure 41 (d), are the rock formations scattered throughout the whole region, the steep terrain on the left side of the road and the exposed surface on the small hilltops where snow does not tend to accumulate. On the other hand, the areas where snow tends to melt later are characterized by either small valleys and depressions or by a flat and smooth terrain, i.e., surface features that allow a significant snow deposit.

8.5. Comparison between melt maps

8.5.1. Yearly differences

The yearly differences between the two satellite derived NDVI melt maps and the optical drone one are reported in Table 6. Minimum map value, maximum, mean, and standard deviation expressed in days are used to analyze the differences for the years 2021, 2022, and 2023.

Table 6: Minimum, maximum, mean and standard deviation value for the yearly maps showing the differences between Sentinel and Planet NVI melt maps and between the two satellites melt maps and Geoformer's snow melt maps.

		2021	2022	2023
Sentinel - Planet	Minimum	-65.75	-26.69	-32.28
	Maximum	58	35.52	45.02
	Mean	-4.19	-3.40	3.11
	Standard dev.	15.38	6.65	10.86
Sentinel - Geoformer	Minimum	-60.98	-20.20	-28.85
	Maximum	27.72	23.83	43.3
	Mean	-6.69	0.88	2.60
	Standard dev.	18.06	7.52	10.51
Planet - Geoformer	Minimum	-66.22	-29.77	-58.15
	Maximum	39	40.65	67
	Mean	-2.13	3.60	-1.53
	Standard dev.	14.35	9.07	15.78

8.5.1.1. Sentinel-2 – SuperDove

Figure 42 illustrates the maps obtained by subtracting the Planet NDVI snow melt map from the Sentinel one. The color scheme is the same one used in the previous chapter, with red corresponding to an earlier melting in the Sentinel map, and blue indicating a later one.

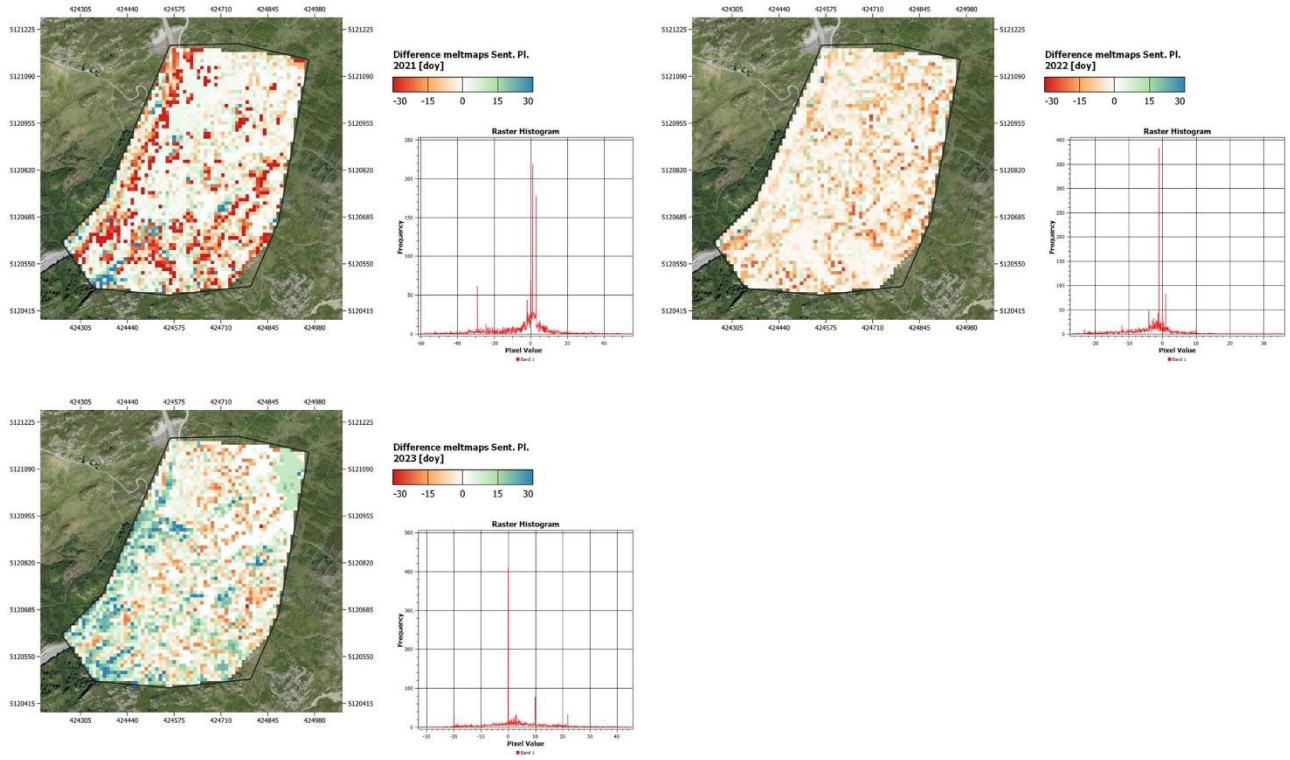

Figure 42 (a), (b) and (c) from top left to bottom left: Difference maps of Sentinel and Planet NDVI snow melt for the years 2021, 2022 and 2023.

While there is a high number of pixels with a value close to 0, the 2021 image has a high number of extreme values on the negative side, meaning that Planet set snow melt later in the year than Sentinel. The relative pixels are not associated to any particular surface feature but are located close to surfaces which both sensors characterized as early melting, i.e., the road and the different rock formations. Sentinel however, set the entire area as uniformly early melting, while Planet still detected some snow covered pixels, resulting in a bigger day of the year melt value. This difference can be related to the different spatial resolution of the two sensors, which allowed Planet to distinguish small snow deposits close to snow free areas.

The few pixels with a positive difference are mainly located in the lower part of the map and are the consequence of the resampling process. After rescaling, the new pixels contain an average of the original information contained in the old, smaller ones, meaning that adjacent pixels with a great difference in melting estimations are averaged. This translates for example in the many neighboring Planet pixels with a value of 113 and 143 being converted to a number between the two, resulting in the difference with Sentinel.

As seen in Figure 24, which displayed the differences in the 2021 Deflection estimations between Sentinel and Planet, the vast majority of values are positive, meaning that Sentinel set the Start of Deflection later in the year than Planet. In the case of NDVI melt maps however, there are more extreme negative pixels rather than

positive ones, suggesting that Sentinel determined the snow melt earlier than Planet. This means that in general, Sentinel-2 tends to identify processes less successfully than Planet, whether it involves vegetation activity or snow melt.

In 2022 the estimations of Sentinel and Planet were more similar to each other, which is highlighted by the lighter shades of blue and red in the image, the minimum and maximum values of the raster, both the smallest ones between the three years, and finally by the high number of pixel close to a difference value of 0. The similarities are already well visible in Figure 40 (b) and Figure 41 (b), both characterized by darker shades of blue and an overall homogeneous appearance. As previously mentioned, this indicates a tight snow melt period associated with the warm and dry winter which characterized 2022. Consequently, since the main snow melt event took place rather quickly, there is less room for mischaracterizing snow cover, resulting in more consistent estimations between sensors. There are still areas where the negative difference is more marked. These are once again the consequence of the resampling process, as the 10 m pixels of the different raster contain the information of different 3 m Planet pixels which originally set snow melt at different time stamps. In contrast to the maps of the other two years, the 2023 image is not dominated by negative values, but instead it is characterized by a higher number of positive pixels, indicating that Sentinel set snow melt later in the year than Planet did. For the vast majority these areas are associated with early melting pixels, which would mean that Sentinel characterized soil, vegetation, or other surface covers as snow. However, as mentioned in the previous paragraph, the differences are tied to the survey days, as in this case the first Planet image used was recorded 22 days earlier than the first Sentinel one, resulting in a much earlier detection. Similarly, the pixels characterized by a difference of 0 are the result of two Planet and Sentinel images being recorded on the same date after a period of 20 days without measurements, meaning that snow had a prolonged period to melt and that the new snow free areas were detected by both sensors.

8.5.1.2. Sentinel-2 – RGB Drone

In Figure 43 are displayed the three maps obtained by subtracting the snow melt map created using the optical UAV from the one obtained from Sentinel-2 images. Due to the much smaller area coverage of the drone surveys, the maps are significantly smaller than what was presented in the previous chapter. This leads to a smaller probability of including areas with particular surface features, such as the rock formation in the lower part of the satellite images and the plateau on the upper right part, both absent from the 2022 map.

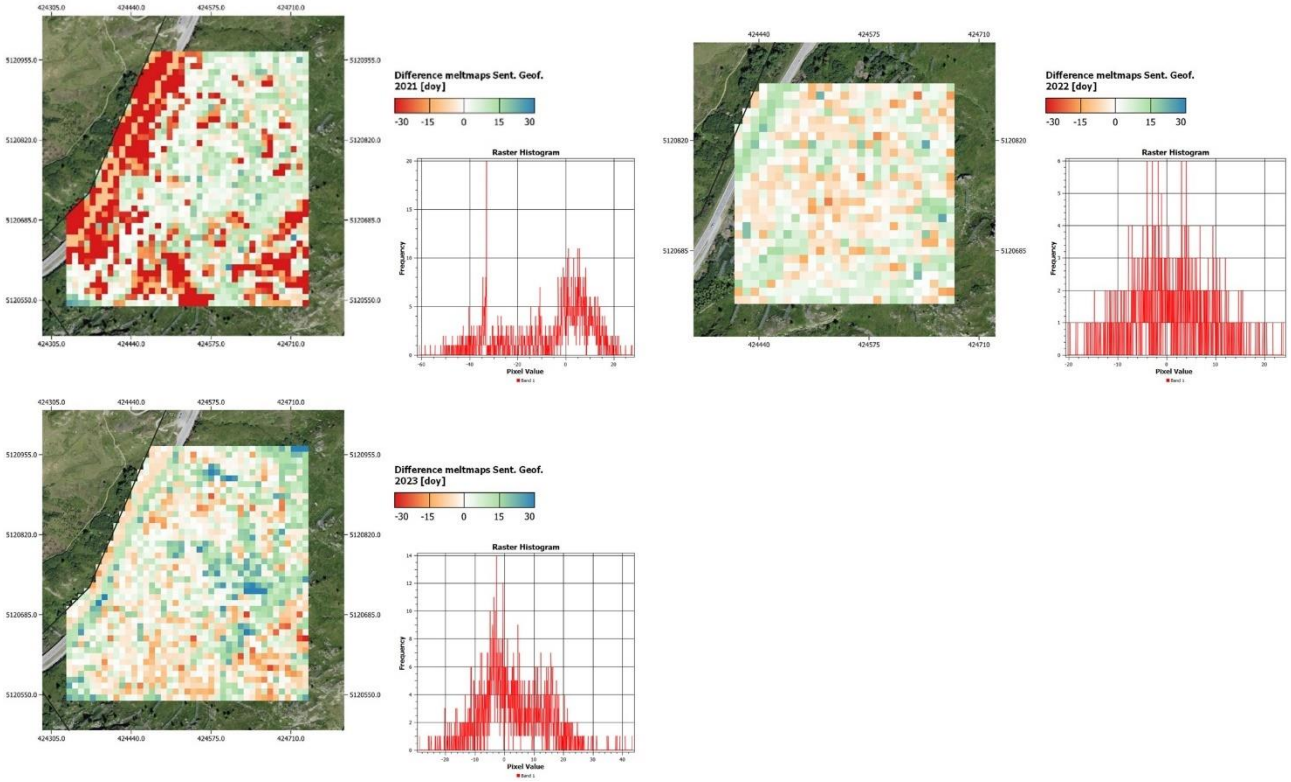

Figure 43 (a), (b) and (c) from top left to bottom left: Difference maps of Sentinel and optical UAV snow melt for the years 2021, 2022 and 2023. Red pixels indicate a negative difference, while green/blue areas correspond to a positive one.

Similarly to what was observed with the Sentinel-SuperDove difference map, the areas of greater discrepancies are located around the road and on the rock formations in the lower part of the image, which are both characterized by early snow melting. In these cases Sentinel estimated the moment of snow melt to have happened earlier in the year than the drone did, which is tied to the first drone survey having taken place later in the year than the date of the first two Sentinel images. This means that when the first drone snow cover map was created, the two satellite images were already used to identify snow free zones, leading to the discrepancies in early melting detection.

Compared to Figure 42 (a) there is also a much higher number of positive values, mainly associated with late melting areas and to Sentinel identifying them later than the drone. This could be related to the lower spatial resolution of Sentinel mixing snow covered and snow free zones resulting in late detection. Similarly to what was observed for early melting however, the difference is related to the date of the used images, as in this case the last drone image was acquired between the penultimate and the last satellite one, resulting in different snow melt characterization.

It appears that in 2021, the two sensors detected snow melt patterns in a similar way, nevertheless, mainly due to the different image acquisition time, there are differences regarding the values of the single pixels, which can reach a value of -60 days in the steep areas surrounding the road.

Similarly to what was observed in the previous chapter, in 2022 Sentinel and the optical drone had a more similar classification than in 2021. In this case the consistency seems to be even higher, as the map has the lowest minimum and maximum value out of all 9, a mean of 0.88 and the second lowest standard deviation, just behind the difference map of Sentinel-Planet 2022. In this case the negative and positive differences are not related to early and late melting areas, as the results are once more tied to the resampling. Compared to Planet, which changes from a resolution of 3 m to 10 m, the drone images have an initial resolution of 5 cm, meaning that the pixels in the final, rescaled map will contain much more diverse information. As a result, the different day of the year values are averaged, and the distinction between early and late melting areas is made more subtle. It must also be considered that the area of the 2022 drone map is particularly small, which, as previously mentioned, leads to a smaller probability of having discrepancies with the satellite data.

Similarly to what was observed in the case of Sentinel-Planet, the 2023 Sentinel-Drone map has a higher number of pixels with a positive difference compared to the previous two years. This suggests a later snow melt identification by Sentinel, which is once again a consequence of the Drone map being created using earlier acquired images. As a result, even though both methods defined similar areas as early melting, the overall later identification by Sentinel results in a negative difference. There are also many areas with a negative value, indicating where the melting was identified earlier by Sentinel. These pixels are mainly found in the lower part of the image and are the same ones also visible in Figure 43 (a), meaning that in general, Sentinel sets snow melting on steep rocks formation earlier in the year than sensors with a higher spatial resolution, be it Planet or the optical drone.

8.5.1.3. SuperDove – RGB Drone

The maps showing the difference between Planet and the optical drone snow melt estimations are displayed in Figure 44.

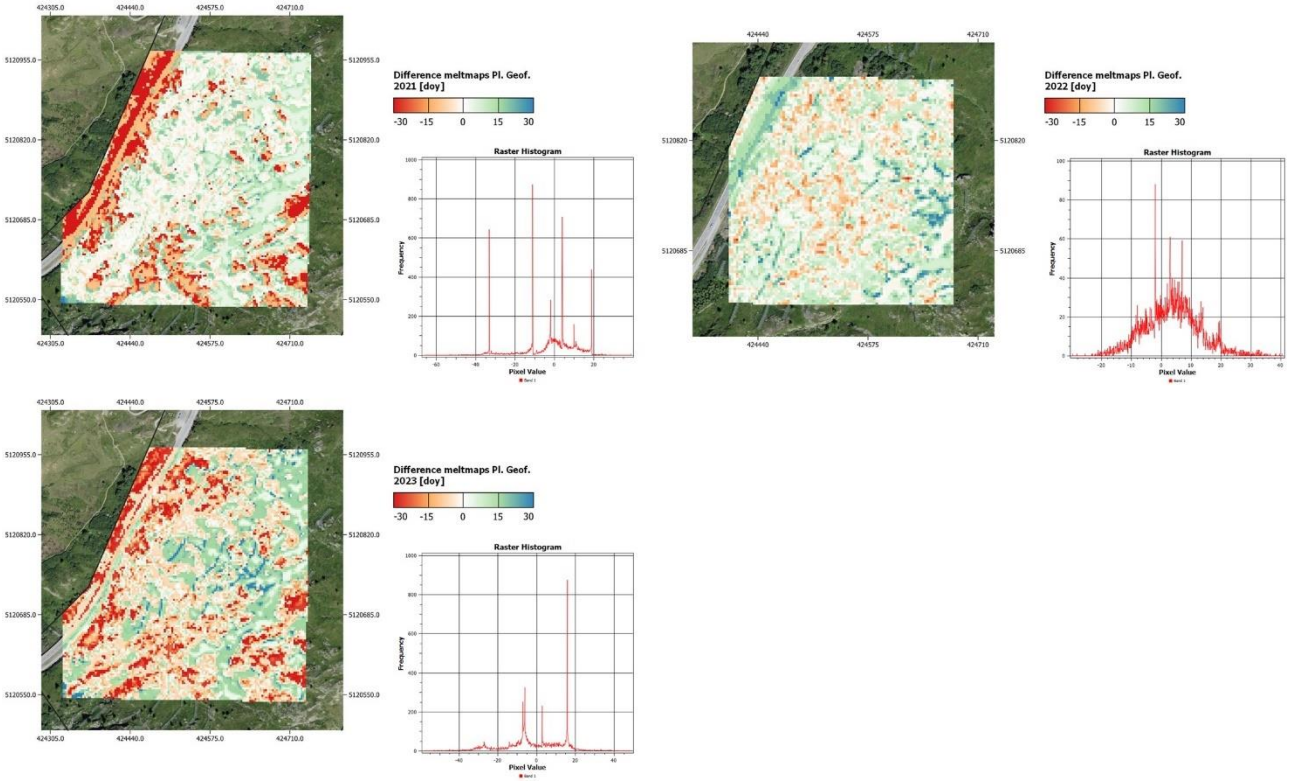

Figure 44 (a), (b) and (c) from top left to bottom left: Difference maps of Planet and optical UAV snow melt for the years 2021, 2022 and 2023. Red pixels indicate a negative difference, while green/blue areas correspond to a positive one.

The 2021 Planet-optical drone difference map highlights the same areas observed in Figure 43 (a), meaning that the surroundings of the road and the rock formations are characterized by a negative difference, while the rest of the image by a positive one. Similarly to the Sentinel case, both the negative and positive values are the result of the different acquisition dates of the images, rather than a difference in sensor spectral and spatial resolution. There is a noticeable difference in pixels located on the right side of the road, as there are less extreme negative ones, meaning a greater consistency between Planet and the optical drone. These areas are visible in Figure 42 (a) and, considering their similarities in the Planet and drone snow melt map, suggest that the Sentinel estimation was set too early in the year.

The consistency of the 2022 estimation is also visible in the Planet – drone difference map, as the areas highlighted in Figure 43 (b) can be easily found in Figure 44 (b). The most noticeable difference is found in the higher spatial resolution, which allows to better distinguish the different areas and to confirm that the positive and negative differences are not related to early/late melting areas or to any particular surface feature. In this case too, the higher similarity between maps can be related to the weather of winter 2022, which resulted in a reduced period of snowmelt.

The 2023 map displays almost the exact same pattern as the 2021 one, meaning that the same areas are characterized by negative and positive differences. The most noticeable differences are the darker shades of green, associated to a later Planet estimation, and the higher frequency of moderate negative values, tied to a slightly earlier Planet snow melt. Regarding the first difference, the green pixels are associated to an important snow melt event which took place under cloudy conditions approximately between day 120 and 140. Since the only drone image acquired during that interval is dated day 130, and the only cloud free Planet image available was recorded at day 146, it can be affirmed that the sensors characterized the snow melt event at different development stages. As a result, Planet observed the same snow free areas, which by that time also grew in size, 16 days later than the drone, leading to the positive difference.

The negative difference pixels are once again tied to areas characterized by rocks, meaning an early melt detection for both sensors, which in the case of Planet was further anticipated by the lower spatial resolution not allowing the detection of smaller patches of snow.

8.5.2. Differences in pattern identification

Figure 45 shows the average normalized melt maps of the different sensors created using the single year snow maps of 2021, 2022 and 2023. The color scheme is the same as the one first presented in chapter 8.4.2, which associates an early snow melt to darker shades of blue and late melting one to light cyan and white. All three datasets have been normalized between 0 and 1, meaning that the three histograms have the same value interval. Normalizing and averaging the data also allows to better identify melting pattern, having reduced the

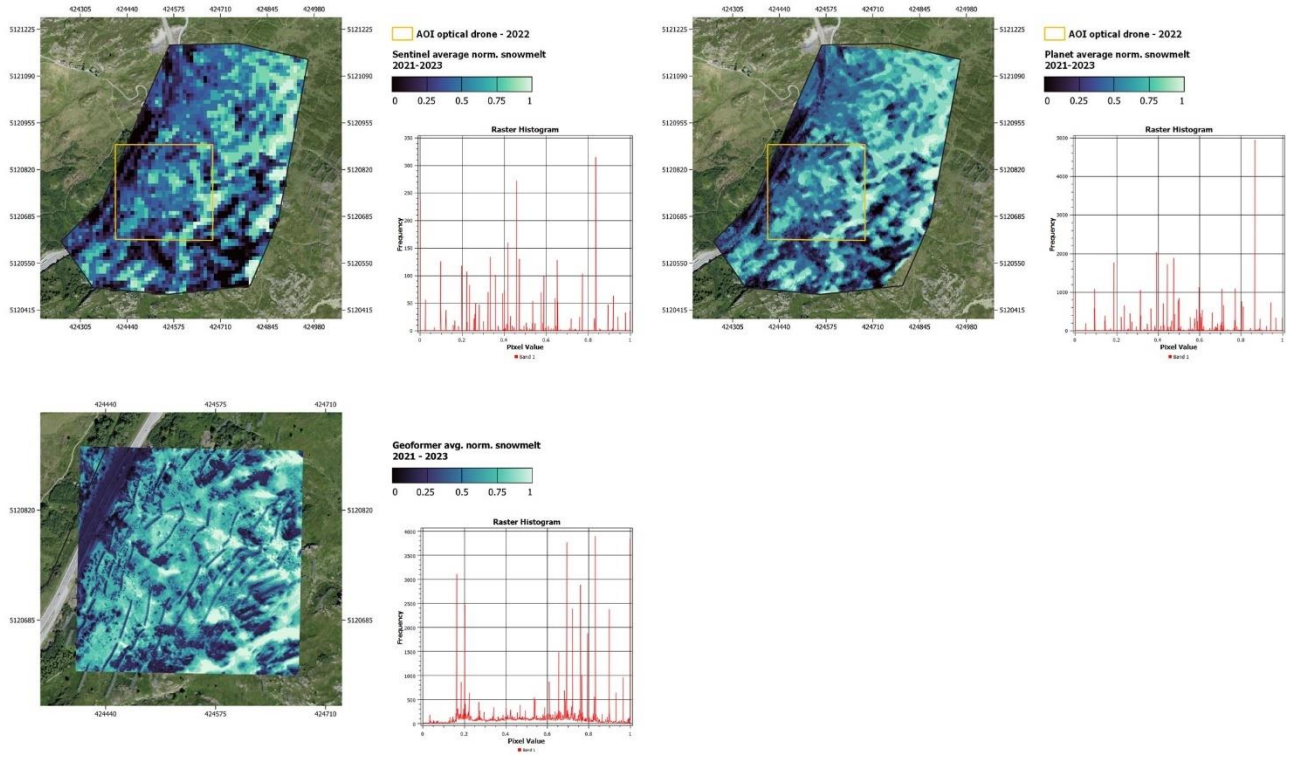

Figure 45 (a), (b) and (c) from top left to bottom left: average normalized NDVI melt map for Sentinel and Planet, average normalized melt map created using the optical drone. The orange square in the first and second image indicates the area coverage of the optical drone. Dark shades of blue indicate an early melting area, while light cyan in associated with late melting.

impact of extreme years such as 2022. The orange square in Figure 45 (a) and (b) indicates the area covered by the RGB drone and should be helpful to identify any recurring pattern between the three images.

The first point to notice after comparing the three maps are the striking similarities regarding which areas are characterized as early melting and which ones as late, especially noticeable between Sentinel and Planet. As a matter of fact, the Sentinel-2 map is an almost exact, lower resolution copy of the Planet image, with the only major difference being the more discrete borders between the different early and late melting areas. This is reflected by the shapes of the two histograms in Figure 45 (a) and (b). The first one coincides with the Sentinel image and shows two distinct peaks, the first slightly after 0.45, corresponding to the blue pixels mostly located in the left part of the image, and the second close to 0.85, being associated to light cyan and the late melting areas in the upper right part of the image. On the other hand, the Planet histogram has only one peak located near 0.85, related to the same late melting areas visible in the Sentinel image, while the rest of values are more easily distributed. This means that the Planet image has a smaller prevalence of specific values and a better distinction between similar melting patterns, which Sentinel did not identify. This difference is related to the lower spatial resolution of Sentinel-2, which resulted in not being able to distinguish small differences in melting patterns and the relative homogenization of average melt values. On the other hand, the higher resolution of Planet allows to identify less noticeable melt dynamics and to create a more precise average melt map.

In the case of the drone maps the visual comparison is more complicated, both due to the different size of the image and to the higher degree of differentiation between the highlighted areas. It is still possible to identify recurring patterns, such as the one visible in the diagonal series of light cyan pixels in the lower right part of the drone area, which for all three sensors is associated with late melting. In general however, the drone map is characterized by brighter shades of blue associated with a late melting. This point can be explained by considering the particular shape of the histogram of the drone image. Contrarily to the one of the satellite images, it is characterized by two distinct regions, the first associated with particularly early melting pixels and the second to late starting ones, with very few values in between.

The discrepancies can be further explored by calculating the difference between the three maps. Figure 46 (a) was obtained by subtracting the Planet average normalized melt map from the Sentinel one, Figure 46 (b) shows the differences between Sentinel and the drone, while Figure 46 (c) between Planet and the drone.

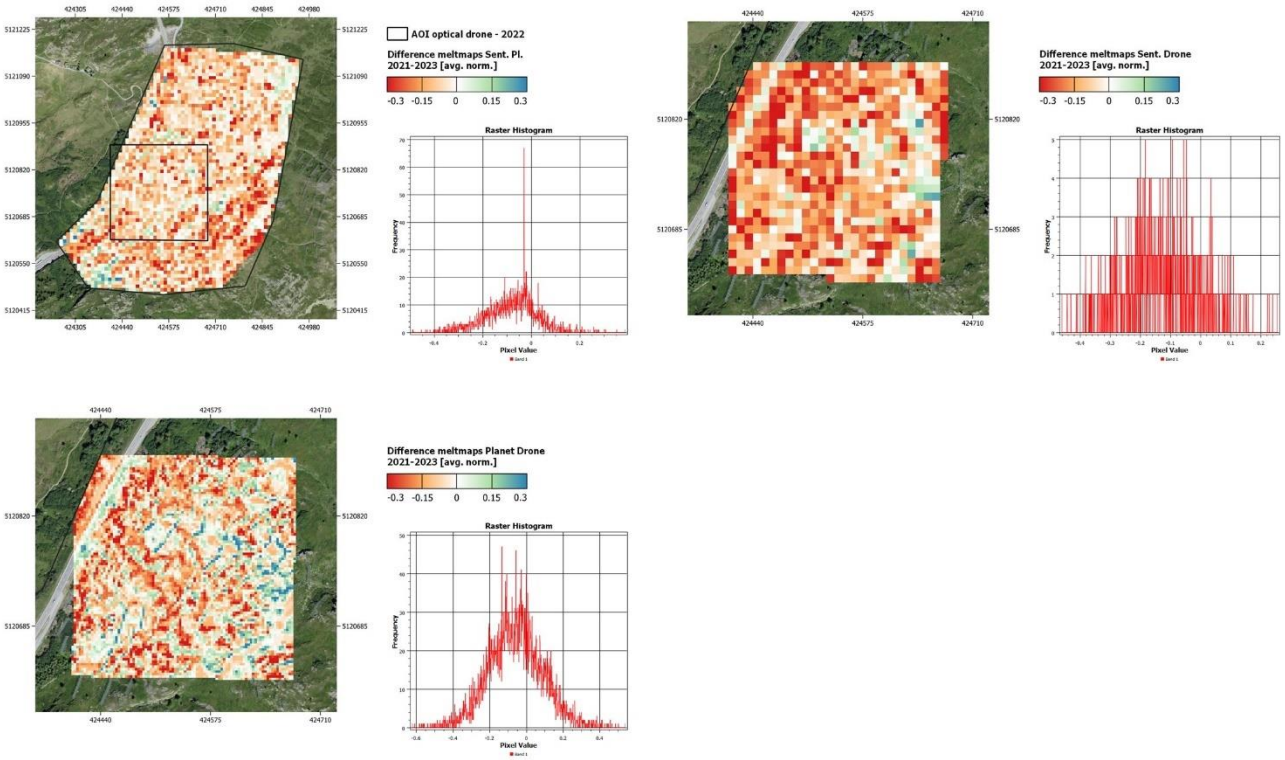

Figure 46 (a), (b) and (c) from top left to bottom left: Difference map between Sentinel and Planet, between Sentinel and the optical drone and finally between Planet and the drone. Red pixels indicate a negative difference, while green/blue areas correspond to a positive one.

The Sentinel-Planet difference map displays a predominance of red pixels, meaning that in these cases the average normalized snow melt has a lower value in the Sentinel image than in the Planet one. These pixels are located where there is a transition between early and late melting areas, which as previously mentioned, is better characterized in the Planet map. As a result, the early melting Sentinel pixels correspond to medium-early Planet one, leading to a negative difference.

Regarding areas with a positive difference, the vast majority is tied to late melting zones, in particular the upper right part of the image, which both sensors characterized as the latest melting. The earlier Planet estimation at the base of the positive difference is the result of the last measurement of 2023, which took place on day 153, 3 days earlier than the Sentinel one. As a result, this small difference in acquisition time led to a slightly smaller average normalized value. This suggests that estimations are also influenced by the small number of years available, as with just three years the weight of each one is much more noticeable than in the case of a 10 year analysis.

It can also be noticed that for most pixels in which the difference between layers is minimal, corresponding to a value of 0 and to colors close to white, are the ones where snow melts later. These areas are easily identifiable

in the NDVI images of both sensors, as the last patches of snow usually stand out from the other surface features and can therefore lead to more precise snow cover maps.

Contrarily to the Sentinel-Planet map, the difference image of Sentinel and the optical drone is characterized by a much greater number of negative values, with just a handful of positive ones. The most marked negative difference is found on the steep area on the right side of the road which, as visible in Figure 45 (a) and (c), is characterized by Sentinel as the earliest melting one, while the optical drone identifies snow melt as usually happening later in the year. As previously mentioned, the discrepancies in these areas are tied to the combination of low resolution and smaller snow deposits, which led to a snow free categorization by Sentinel. The other negative pixels are not related to any particular surface feature but are the result of the time between the first and the rest of the drone surveys previously mentioned, which resulted in the majority of the normalized drone pixels to have similarly high values. This is also noticeable considering the few difference values close to 0, which are associated to the last melting areas in the Sentinel image and therefore have a similar normalized value in the drone map.

Similarly to the Sentinel case, the Planet-drone difference map is dominated by negative pixels, which can be explained by the same factors cited in the previous paragraph. On the other hand, there is also a larger number of positive pixels, which are associated to late melting areas being better characterized in the Planet image than in the Sentinel one. There is also a noticeable number of positive values tied to snow nets, which, even after resampling to match Planet spatial resolution, remained a dominant feature in the Drone image. As seen in chapter 8.4.1.1, the shadow of snow nets results in the area below them to be classified as snow free even though snow is still present, leading to a final estimation which sees them as extremely early melting areas and therefore to a positive difference when compared to the Planet map.

Even though the difference images suggest major discrepancies between the three sensors, the appearances of the normalized average maps in Figure 45 highlight a general consistency in the estimations of where early and late melting areas are located. These similarities, however, are only visible at higher scales, meaning that a comparison focused on smaller areas reveals the limitations of Sentinel, and partially of Planet, in high precision melt pattern identification. It must also be noted that even though using the drone resolves the resolution issue, there are still limitations regarding reduced area coverage, the need to travel to the study area and the small number of available images. Therefore, it can be affirmed that Planet is able to offer a compromise between the high resolution of the drone, and the extended area coverage and image availability of Sentinel.

8.6. Snow depth map

Figure 47 shows the snow depth map created using the DSMs of the first and second flight of the multispectral drone. Having subtracted the second, almost completely snow free DSM from the first, snow covered one, the colors represent snow height at the moment of the first. The color scheme is the same one used in the other chapters, meaning that blue corresponds to a positive difference between the two layers, red to a negative one, and 0 to perfect consistency.

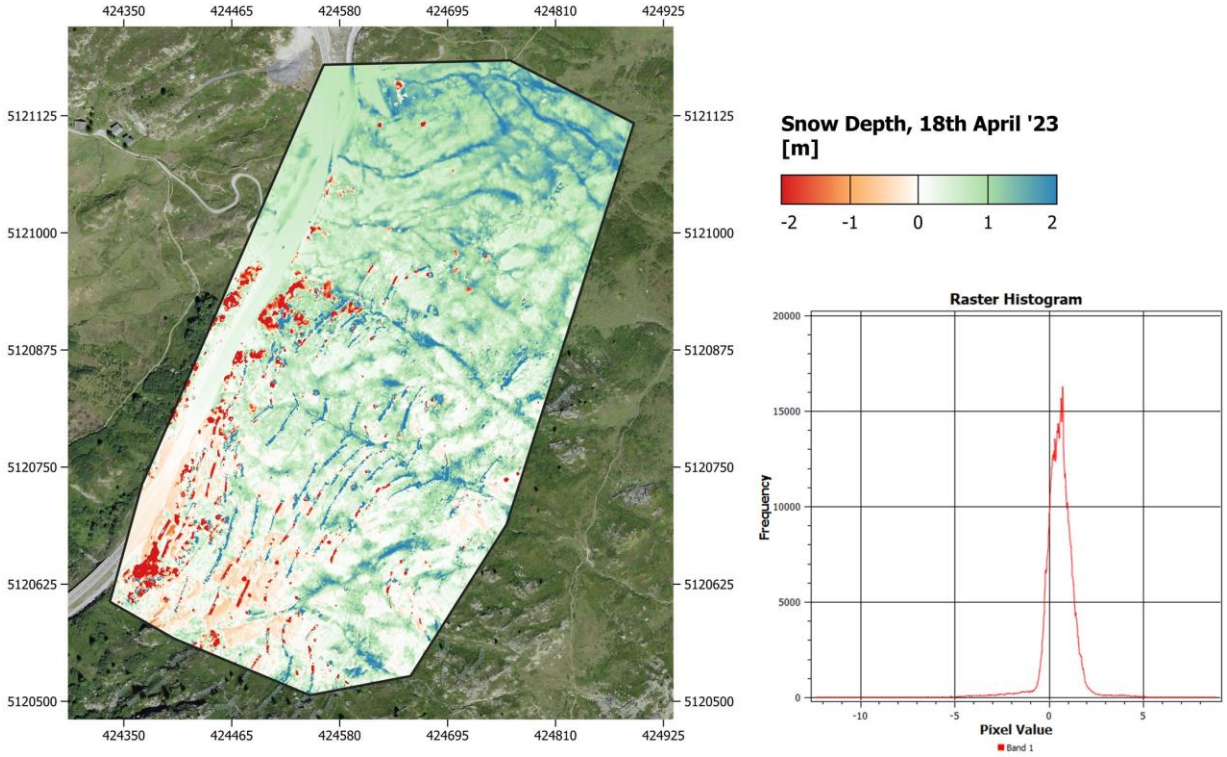

Figure 47: snow depth map derived from the DSMs of the first (snow covered) and second (snow free) flight of the multispectral drone. Blue indicates a positive difference, meaning that the first DSM has a greater height value, red areas are associated to a higher second DSM. Blue pixels are tied to larger snow deposit, white one to surfaces already snow free during the first flight and red ones are tied to trees and a referencing error.

The first noticeable characteristic of the image is the presence of negative pixels, which in some cases reach a value of almost -12 m, meaning that during the second flight the same area was 12 m higher compared to the position during the first survey. Considering that such big differences are possible only in the case of extreme events such as avalanches or landslides, it can be assumed that the extreme negative values are the result of an acquisition or processing error tied to one of the two flights. In this case the issue is tied to trees and their different growth stages, as during the first flight the canopy was not developed enough to be included in the point cloud and consequently, they appear flat in the DSM. On the other hand, at the moment of the second flight vegetation was more developed, which resulted in a better representation in both the point cloud and the DSM, and which ultimately led to the extremely high negative differences. The other red pixels correspond to snow nets and are the result of the referencing error encountered during the first flight mentioned in chapter 8.4.1.1. As due to the positioning shifts experienced in the second and third sector, the location of the snow nets is not consistent, resulting in both over- and underestimation errors in the difference raster, visible in

Figure 48. Similar issues are also visible in the lower left part of the map, characterized by slightly negative values which are the result of height overestimation in the second DSM.

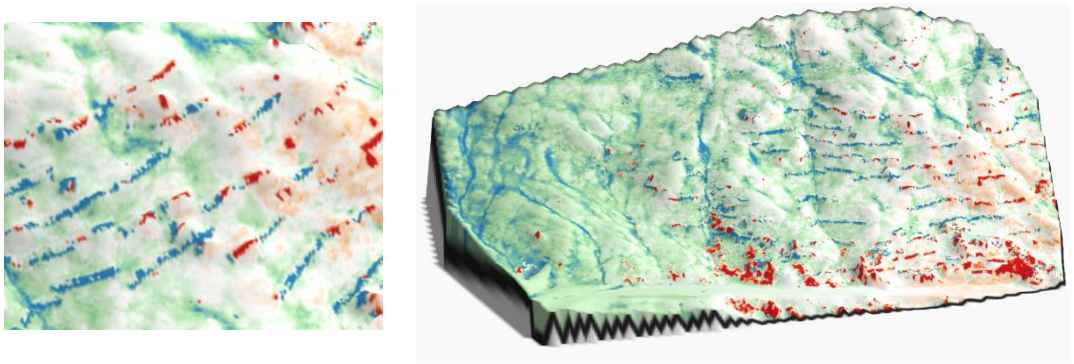

Figure 48 (a) and (b): closeup of 3D snow height map with focus on positive and negative values associated with snow nets, and snow depth map projected over the DSM of the third flight.

Being created using a DSM, Figure 48 also allows to investigate the relationship between snow deposits and topography, and therefore to assess the reliability of the snow depth map. It appears that snow tends to accumulate more in terrain depressions, such as the ones visible in the left and upper right part of the map. On the other hand, the lowest height values are found on hilltops and rock formations, i.e., where snow deposits tend to be smaller due to the exposition to wind or surface complexity. White areas are associated to a constant height between the two DSMs and correspond to the surfaces already snow free during the first flight visible in Figure 34. An assessment of the accuracy of the map can be derived from the values of the road, as contrarily to vegetation, and marginally to terrain, it should have a constant elevation in the DSMs, meaning that in the difference raster it should always have a value of 0. Therefore, the different values of the road section in the snow height map give a measure on the impact of the georeferencing error. This disparity spans from a minimum of -20 cm to a maximum of 75 cm, indicating the lack of referencing consistency between datasets. Another factor that determines the accuracy of snow depth estimation is the characteristics of the snow free DSM. This is visible in Figure 49, which displays a closeup of the same area during the second and third flight. The area visible in Figure 49 (a) has better conditions for generating a DSM as close as possible to a DTM (Digital Terrain Model), as vegetation is not as developed as it is at the moment of the third flight. However, there are areas where snow is still present, thus causing an underestimation of snow depth. On the other hand, despite the absence of snow, vegetation was much more developed during the third flight, meaning a greater height value in the DSM which is closer to the snow height and result in an underestimation of snow depth.

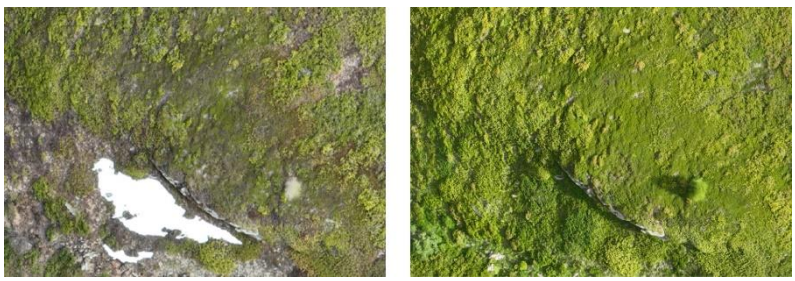

Figure 49 (a) and (b): closeup of the same area during the second and third flight showing the different development stages of vegetation.

9. Discussion

The next section discusses the used data, pre-processing, applied methods and final results.

9.1. Data

9.1.1. Satellite images

Sentinel-2 imagery from 2018 to 2023 was used to produce NDVI time series of the Chalberweid area, profiting from its high spectral, spatial, and temporal resolution (Drusch et al., 2012), which allow for an increased capability in vegetation monitoring and phenology estimation (Misra et al., 2020). The Level-2A data used in this Thesis was obtained through the correction of visible atmospheric effects in Top-of-Atmosphere products by the Sentinel-2 atmospheric correction (Sen2Cor) processor (Li et al., 2018).
Considering the surface features of the study area, it can be affirmed that the high performance of Sen2Cor when dealing with the classes of cloud high probability pixels, not-vegetated and snow (Main-Knorn et al., 2017) lead to high quality and reliable images. The major drawback of Sentinel-2 is the spatial resolution of 10 m, which, even though is considered to be high, leads to a higher number of mixed pixels (Helfenstein et al., 2022) and consequently to a less precise distinction between surface features.

The availability of usable Planet images was limited to just 2021, 2022 and 2023, as the older images produced by previous sensors in the PlanetScope constellation were not characterized by a high enough quality. Moreover, an eventual matching of older and newer data would lead to a loss of quality in the more recent images (Frazier and Hemingway, 2021). The surface reflectance is derived from top of atmosphere (TOA) reflectance is calculated with coefficients provided with the Planet Radiance products and on average is almost identical to the one of Sentinel-2 (Tu et al., 2022).
The major known limitations are the lack of correction of the effects of haze and thin cirrus clouds (Planet Team, 2022), and the underestimation of index values for vegetated surfaces (Tu et al., 2022). Furthermore, the Planet sensors showed a reduced ability in acquiring surface reflectance values within a 5% reflectance variation at a 95% confidence level (CL), which is a typical characteristic of constellation-based data. This contrasts to the performance of images obtained through a single satellite, which show a consistent 5% variation at a 95% CL (Tu et al., 2022).
An issue encountered during data selection related to the Planet product is the lack of usable images over a significant period, as it was the case in 2021. From the 24th of April to the 20th of May, all the images available for download were either completely cloud covered, had major areas of missing data or were full of artefacts.

Despite the issues mentioned above, the reflectance data of Sentinel-2 and SuperDove shows a strong linear correlation for all spectrally overlapping bands, with a relative mean error close to zero on average when considering all surface covers (Tu et al., 2022). This resulted in a high consistency between NDVI estimations and consequently to similar estimations of phenology and snow cover.

9.1.2. Drone images

Even though the accuracy of the Mavic 3M cameras has not been tested yet, the use of multispectral, low-budget UAVs for the generation of vegetation indices such as NDVI has proven to give estimations (Raeva et al., 2019). The major issue encountered was related to the RTK problems encountered during the first, which resulted in a limited accuracy of the single channel images and consequently of the snow cover map. These errors can be solved with Post-processing Kinematic (PPK), however, the existing workflows focus on RGB channels, as the correction of the NIR channel does not exist, and there are no plans to implement it. Another possible solution in these cases could be complementing RTK with a small number Ground Control Points (GCPs), thus reducing the eventual inaccuracies of position estimations (Forlani et al., 2018).

Despite the inaccurate georeferencing in the lower part of the study area, the NDVI and NDVIe snow cover maps showed a greater precision in distinguishing snow from other surface features than the RGB ones, which were characterized by extensive snow underestimation. Another point regarding the RGB drone is that the advantage of having an extremely high spatial resolution is counterbalanced by the poor accuracies of the snow cover maps caused by the influence of low reflectance areas. Therefore, the use of a multispectral drone represents an upgrade over an optical one, both in terms of vegetation sensitivity and snow cover estimation, which ultimately lead to reliable high resolution maps.

9.2. Study area

The complexity of the study site played a significant role in determining the performance of each method. In the case of Chalberweid, the area is characterized by a continuous alternance of trees, bare rocks, snow nets, hilltops, and valleys, i.e., features with different spectral signatures or physical properties. Consequently, a higher spatial resolution leads to having less pixels being located on the boundaries between features, reducing the number of mixed pixels, hence resulting in a higher accuracy of reflectance and NDVI estimations (Woodcock and Strahler, 1987).

Therefore, the degree of heterogeneity of a surface can determine if the higher spatial resolution of SuperDove offers an advantage over Sentinel-2. If a study has to be conducted over an extensive surface which is composed by either tree clusters or bare soil, then the difference in resolution between Sentinel-2 and SuperDove would not be the deciding factor. On the other hand, if there is a greater variation of surface features, such as in the Chalberweid case, then the 3m resolution of Planet provides an edge over the 10m one of Sentinel-2.

9.3. Data consistency

The main sources of discrepancies highlighted during the analysis of Start of Deflection and NDVI melt maps are tied to the extent of the raster and the normalization process. If the extent of the images to compare is not the same, there is the possibility that one of them does not contain particular areas useful for the analysis. This can be seen in the case of the optical drone maps, which cover only the central part of the study area, therefore

excluding the lower part characterized by rocks and small valleys, and the upper part, which is usually theater of late snow melt. When possible, the images to be compared should be clipped to the same extent at the beginning of the analysis, thus analyzing the same pixels which results in a more accurate comparison. In this case however, the number of rasters will be extremely high, as each comparison requires a different image size.

A direct consequence of image size was encountered during data normalization and is tied to the range of pixels values, which, for areas with similar surface features, is usually wider for large surfaces and narrower for smaller ones. Therefore, when comparing the pixels found in both the drone and the satellite images, the ones associated with the UAV were much more heterogeneous than the satellite ones, being the consequence of the extreme early and late melting surfaces being outside the common area. Moreover, as the technique used for normalization is based on minimum and maximum raster value, it is highly susceptible to outliers. As the LSP algorithm works at a pixel level, the presence of one extreme early or late Deflecting area determines the minimum or maximum value, which will then be the 0 or 1 in the normalized raster. On the other hand, both the drone and the NDVI melt approach are based on the detection of snow free surfaces, meaning that the influence of single pixels is reduced to almost being none. These differences explain the more homogenous appearances of the average normalized Start of Deflection maps visible in Figure 30, opposed to the more extreme colors shown in the NDVI melt maps in Figure 40 (d) and Figure 41 (d).

9.4. Land Surface Phenology for snow dynamics characterization

The use of double logistic fitting and third derivate calculation has been recognized as successfully able to analyze NDVI time series and extract different phenological metrics (Busetto et al., 2010). However, the relationship between snow melt and start of vegetation activity can vary between plant species and in relation with topography (Gehrmann et al., 2017), leading to difficulties in identifying a rule which allows to relate them to each other. In this Thesis the day of the year where vegetation activity can serve as a proxy for determining snow melt has been set at the moment where the fitted curve starts ascending. This choice was made under the assumption that vegetation remains inactive in winter under snow (Kappen, 1993), which means that the moment just after snow melt corresponds to a plant activation and a relative spike in the fitted NDVI curve. However, after comparing the different Start of Deflection date to both the snow cover maps and RGB Planet images, it appears that the beginning of the greening phase was set too early for a correspondence to snow cover. An improvement in the estimations would be obtained by setting the Start of Deflection slightly later, which in this case would correspond to the first local maximum of the second derivative.

After the first processing of Sentinel-2 2023 images done at the end of November 2023, more than half of pixels did not allow for the LSP algorithm to work properly, resulting in invalid data and rendering the Start of Deflection map useless. The issue was tied to the low number of snow covered images encompassing the last months of the year, which led to the algorithm not being able to fit the time series. This was resolved by

extending the time interval considered when determining the different phenological metrics, thus allowing the creation of the second plateau of low NDVI values located after the end of season.

Overall, the Sentinel-2 Start of Deflection maps showed a direct dependance on temperature and precipitation, being mainly determined by a combination of both. The consistency between the estimations of Sentinel-2 and SuperDove for 2021, 2022, and 2023, allows to affirm that the Planet maps show the same climate dependance previously mentioned. Due to the similarities in spectral characteristics, the major inconsistencies between the estimations of the two sensors can be tied to spatial resolution. In the case of Sentinel-2 the greater pixel size renders the association of map features to topography quite difficult, being however able to generally distinguish the different early and late deflecting pixels. It falls short in the case of complex topography, where high spatial resolution is required to create a Deflection map which strongly correlates to the terrain. Moreover, it was observed how the higher number of mixed pixels led to an averaging of both standard and normalized Start of Deflection values. To this matter, the highest spatial resolution of SuperDove resulted in a lower number of mixed pixels, which allowed clearer NDVI estimations and a better association of Deflection estimations to surface features (Woodcock & Strahler, 1987).

The best assessment of the precision of the LSP method would be a comparison with a snow melt map created using multispectral drone images acquired every 3 to 5 days during the melt period. If that was to be the case however, the drone surveys would need a full day just for covering the same area as the satellite map, meaning a larger amount of resources needed in the form of time and cost of batteries.

9.5. NDVI and snow melt pattern identification

NDVI was added to the snow cover analysis after evaluating the precision of the multispectral drone NDVI snow maps. It was tested as a high resolution alternative to NDSI, as the SWIR band necessary for its calculation has a spatial resolution of 20 m in the case of Sentinel-2 and is not provided in the Planet data.

Considering the maps shown in Figure 40 (d) and Figure 41 (d), it can be argued that when using NDVI to identify snow melt, Sentinel and Planet show similar performances, with the higher resolution of the latter offering a significant advantage in detecting smaller early and late melting areas. It was also observed that Sentinel-2 usually sets snow melting on rocks earlier than the sensor with the higher spatial resolution, whether Planet or drone. This is tied to snow deposits on rocks being smaller and overall less noticeable than on flatter terrain. As consequence, the higher resolution of the drone, and partially of SuperDove, allows the detection of smaller patches of snow, while on the other hand, these deposits are not dominant in the Sentinel-2 image and the pixel is characterized as being snow free.

While NDVI has proven to be an acceptable substitute for NDSI in snow cover estimation, the analysis of snow melt does not offer a reliable estimation about the exact day an area turns snow free. In fact, the results of the snow melt analysis are strictly dependent on the available images. The scenes captured by the three sensors, i.e., Sentinel-2, SuperDove and the optical drone were not acquired at the same time, meaning that

they documented snow cover at different development stages. Therefore, it is possible that the snow identified by one sensor has melted in the next available images of the other two, meaning that they will characterize that area differently, one as later melting and the other two as early. Moreover, it can happen that the main melt event takes place when there are not usable images, whether it is due to the presence of clouds or simply because of missing data. In this case the difference in snow cover extension between two consequent images would be massive, resulting in not being able to determine where snow melt happened first.
Another issue is tied to the choice of the first image to be used for the creation of the melt map, as instead of a pixel level analysis such as the LSP one, the NDVI snow detection method is based on the distinctions between snow covered and snow free surfaces visible to the naked eye. As a result the small, first melting areas stay undetected until they are large enough to be noticed, leading to an overestimation of snow free doy.
During the analysis it was also noticed that in 2021 and 2023 optical drone analysis the time interval between the first and second image used was 21 and 24 days respectively, which are in contrast to the time interval between acquisitions during the main melting event, which is usually between 5 and 10 days. As consequence, the majority of normalized values was set close to one, with very little variability between each other, as visible in Figure 45 (c). These extremely high normalized value led to the differences with Sentinel and Planet average normalized melt maps mentioned in chapter 8.5.2.

In general using NDVI for estimating snow cover and its melt patterns did not give particularly accurate results, especially regarding exact day values. However, the average normalized maps closely resemble the ones created using LSP, meaning that they could be used as a less precise, simpler, and less in need of resources alternative.

9.6. Snow depth map

The main issues regarding snow depth estimations are tied to the referencing problems encountered during the first and second flight, and the relative inaccuracies of the DSMs generated. This resulted in the lower part of the study area being characterized by negative estimations of snow depth, mainly associated with trees and surfaces where snow tends to accumulate less, such as rocks and hilltops. In order to obtain a DSM that represents the terrain as precisely as possible, the area should be snow free, with vegetation still undeveloped, so that there would not be any underestimation of snow height. For this Thesis the ideal time to generate a DSM would therefore be in-between the second and the third flight, slightly closer to the second, so that snow is not present anymore and vegetation has not had enough time to grow and influence measurements. In this case the second DSM was chosen over the third as the advantage of having lower and less developed vegetation exceeded the drawback related to the few patches of snow still present. The areas highlighted are consistent with the ones identified in the Start of Deflection and NDVI snow melt analysis, being hilltops and rocks as surfaces with low deposits, and valleys and secluded areas characterized by greater snow depth.
After considering the extreme negative values of trees and rocks, and the inconsistency in road elevation, it can be affirmed that the snow depth map shown in Figure 47 does not provide a reliable snow height estimation and it is limited to being a qualitative tool indicating where snow tends to accumulate more.

9.7. Advantages and disadvantages of each method

The next part covers the advantages and disadvantages of the different sensors and techniques previously described. The analysis considers the performance of the Start of Deflection maps crated using Sentinel-2 and SuperDove, the NDVI snow melt maps derived from the same two satellites, the single day snow cover map calculated with the multispectral drone, and the snow melt map created by the engineering firm using the optical drone.

Table 7: Table of advantages and disadvantages of the used methods.

	Advantages	Disadvantages
Sentinel-2 LSP	• Moderate correspondence between map features and topography • Interpolation of NDVI time series allows continuous Deflection values • Images are freely accessible	• Moderate spatial resolution • Averaging effect on melt patterns • Long processing • Data needs to cover the entire year (images from Jan. to Dec.)
SuperDove LSP	• High spatial resolution • Maps clearly relate to topography • Interpolation of NDVI time series allows continuous Deflection values	• Long processing • Data needs to cover the entire year (images from Jan. to Dec.) • Images are available only through a subscription plan
Sentinel-2 NDVI snow melt map	• Quick processing • Moderate accuracy of melt pattern • Images are freely accessible	• Low accuracy of absolute values • Highly susceptible to images availability • Moderate spatial resolution
SuperDove NDVI snow melt map	• High spatial resolution • Quick processing • Melt patterns are consistent with early/late Deflection areas	• Low accuracy of absolute values • Highly susceptible to images availability • Images are available only through a subscription plan
Multispectral drone snow cover map	• Extremely high spatial resolution • Low cost • High accuracy • Control over acquisition date and time	• Limited area coverage • Ground based • Highly susceptible to images availability
Optical drone snow melt map	• Extremely high spatial resolution • Low cost • Moderate accuracy • Control over acquisition date and time	• Limited area coverage • Ground based • Highly dependent on scene illumination • Highly susceptible to choice of survey day

The yearly Start of Deflection maps created using Sentinel-2 NDVI time series showed a consistency with the climate of each respective year. The image of 2021 displayed a predominance of late deflecting pixels, which reflected the wet and cold start of the year. 2022 had a greater number of early starting pixels, reflecting the dry and hot months which characterized the winter period. Finally, as the beginning of 2023 saw low precipitation but also low temperatures, the Start of Deflection map was more heterogeneous, having a majority of early starting pixels, with some exceptions of late starting ones. Relating the areas with different Deflection values to surface features is not always possible, as in extreme years, the maps tend to have a homogenous appearance, rendering the association of Deflection and snow melt to topography rather complicated. This indicates that, excluding extreme years, using Sentinel-2 allows to determine Start of Deflection values that reflect the yearly climate and are associable with large scale features such as rock deposits or flat, extended areas. The major drawback is represented by the relatively low spatial resolution, which results in the inability to identify smaller features and often leads to an averaging of the deflection values. This effect was particularly visible in the average normalized map displaying the different melt patterns, which shows a weaker distinction between early and late deflecting areas, thus limiting interpretation related to topography and other features.

On the other hand, while the SuperDove yearly Start of Deflection maps showed the same relation to climate as the Sentinel-2 images, the higher spatial resolution of the Planet product led to an improved separation between early/late areas and a better identification of smaller features, such as single rocks, hilltops, and terrain depressions. This is yet more visible in the average normalized image which, contrarily to the one of Sentinel-2, clearly identifies early and late pixels, resulting in a better association of Deflection values to topography.

Similarly to the phenology images, the appearance of the yearly NDVI snow melt maps created using Sentinel-2 and SuperDove showed to be dependent on the winter climate, as in both cases they were characterized by late melting pixels in 2021, early melting in 2022, and a combination of both in 2023. The similarities are also visible in the average normalized images, as in both cases the pattern identified resemble those found in the average normalized Deflection maps. The main differences reside in the detailed appearance of the products, as the NDVI melt maps lack the differentiation between sub-areas, characteristic of the Deflection images. This is tied to the few images used for the creation of the melt maps, which result in pixels having one out of the few values available. Moreover, the melt values indicated in the NDVI maps are strictly dependent on the date of the chosen images, meaning that the value cannot be considered a precise estimation. As a result, the NDVI maps failed to precisely estimate the moment of snow melt. However, considering that the average patterns are consistent with the ones of the Deflection maps, they can still be used as a rough estimate of melt patterns.

While the optical drone approach follows the same principle as the NDVI melt maps, the higher spatial resolution allows for a more precise classification of surfaces. However, it is still limited by the number of images used and by the lower area coverage when compared to satellites. Moreover, the single days maps have displayed a limited accuracy in quantifying snow cover, which, due to the presence of shadows cast by vegetation and snow nets, is often underestimated. To this matter, the use of a multispectral drone and the

relative calculation of NDVI produced a more accurate single day snow cover map, thus representing an improvement for UAV-based, single day snow cover maps.

Defining an objectively better method is not an easy task, as each one proved to have very different advantages and drawbacks, resulting in the definition of the better approach being extremely situational. Due to the interpolation of the NDVI time series, the Start of Deflection analysis produced continuous estimations, which allow a more precise characterizations of surfaces and are less influenced by missing or unusable images. On the other hand, the LSP workflow was the most demanding method in terms of images required, data preparation, processing, and analysis. The differences in spatial resolution between Sentinel-2 and SuperDove are noticeable at smaller scales, as the latter better separated the different pixels resulting in an easier association to surface features. Overall, the SuperDove-based LSP approach would be the preferred method in the case of large, often cloud covered areas, where the focus of the analysis is the quality of estimates rather than obtaining the highest possible spatial resolution.

Compared to LSP, the snow cover and melt estimation based on NDVI maps represents a downgrade in terms of accuracy. However, considering the similarities in pattern identification and that the differences mainly impact small scale areas, this method could be used as a more general and approachable estimate that LSP, as it sacrifices some accuracy in favor of a much simpler and more accessible workflow. One other aspect of the NDVI method to be considered is related to the images used, as the estimations become increasingly accurate the more scenes are used. Similarly to the case of Deflection, the differences between Sentinel-2 and SuperDove are visible at smaller scales, meaning that the latter would be the better choice for more complex areas, where the separation between different features is crucial.

The UAV approach should be preferred when the high spatial resolution of the final maps is a fundamental aspect, however, the limited area coverage makes it useful only in case of small surfaces. Similarly to the NDVI melt maps, this method is dependent on the availability of images, meaning that the absolute estimation of snow melt doy lack the accuracy of the LSP ones. In general, the use of an optical drone should be avoided, as the high spatial resolution is counterbalanced by the low accuracy of snow cover estimations. Therefore, a multispectral UAV should be the preferred option, as it did not show any disadvantage compared to the RGB one.

10. Conclusion and Recommendations

The purpose of this Thesis was to analyze different melt-out timing estimations of satellite-based observations and compare them both between each other and to ground-based products. The main objective of the work was determining the advantages and disadvantages of the different methods in detecting early spring vegetation season start and snow melt in a high alpine region, in terms of both applicability and reliability.

This was done through the use of phenology metrics extracted from NDVI time series acquired from Sentinel-2 and SuperDove, the creation of NDVI based snow melt maps derived from the previously mentioned sensors, snow melt maps generated from an RGB drone, a single day snow cover map and a single day snow depth map created using a multispectral UAV.

It is found that satellite approaches relying on phenology metrics produced similar, yet more precise estimations of snow melt patterns as NDVI- and ground-based methods. The main advantage of Land Surface Phenology relies in the continuity of estimations, not being impacted by few unavailable images, extensive area coverage and not needing to travel to the study area. The drawbacks are tied to the greater number of images needed, longer data preparation and processing, and in the case of Sentinel-2 low spatial resolution compared to SuperDove. The advantage of using NDVI as the sole component in the creation of snow cover and snow melt maps is the workflow simplicity and the few images required. On the other hand, the estimations are less precise, while also being highly susceptible to the date of image acquisition and to missing data.

The RGB drone has the benefit of extremely high spatial resolution, which however is counterbalanced by the limited area covered and relative inaccuracy of the snow melt maps caused by the sensitivity to shadows. To this matter, the multispectral UAV solves the problem of snow underestimation by using NDVI values rather than pixels brightness to identify snow, resulting in a much more precise surface characterization.

Both satellite-based approaches identified similar melting patterns and could be used to effectively identify areas where snow melts first and where last. However, the absolute estimates showed many differences being tied to the discrete values of the NDVI melt maps and their dependence on the image acquisition date. Therefore, these estimates should be taken with caution, as the area can be misclassified if not enough attention is directed towards the selection of images. In this case the best results would be obtained by having a high number of consequent images, all covering the main melting phase. The drone maps should be used in areas where having an extremely high spatial resolution is crucial, in any other case, the performance of the SuperDove phenology approach makes it the better choice.

11. References

Acharya, T.D. and Yang, I. (2015) Exploring Landsat 8, International Journal of IT, Engineering and Applied Sciences Research.
http://earthobservatory.nasa.gov/IOTD/

Alex, E.C., Hari, S. and Ramesh, K. V (2017) 'Quantification and understanding the observed changes in land cover patterns in Bangalore', Article ID: IJCIET_08_04_067 International Journal of Civil Engineering and Technology, 12(4), pp. 597–603.
http://www.iaeme.com/IJCIET/index.asp597http://www.iaeme.com/IJCIET/issues.asp?JType=IJCIET&VType=8&IType=4http://www.iaeme.com/IJCIET/issues.asp?JType=IJCIET&VType=8&IType=4http://www.iaeme.com/IJCIET/index.asp598

Asam, S. et al. (2018) 'Relationship between spatiotemporal variations of climate, snow cover and plant phenology over the Alps-An Earth observation-based analysis', Remote Sensing, 10(11).
https://doi.org/10.3390/rs10111757

Awasthi, S. and Varade, D. (2021) 'Recent advances in the remote sensing of alpine snow: a review', GIScience and Remote Sensing. Taylor and Francis Ltd., pp. 852–888.
https://doi.org/10.1080/15481603.2021.1946938

Barbeito, I. et al. (2012) 'Factors driving mortality and growth at treeline: A 30-year experiment of 92 000 conifers', Ecology, 93(2), pp. 389–401.
https://doi.org/10.1890/11-0384.1

Bashir, F. and Rasul, G. (2010) Estimation of Average Snow Cover over Northern Pakistan, Pakistan Journal of Meteorology.

Busetto, L. et al. (2010) 'Remote sensing of larch phenological cycle and analysis of relationships with climate in the Alpine region', Global Change Biology, 16(9), pp. 2504–2517.
https://doi.org/10.1111/j.1365-2486.2010.02189.x

Caparros-Santiago, J.A., Rodriguez-Galiano, V. and Dash, J. (2021) 'Land surface phenology as indicator of global terrestrial ecosystem dynamics: A systematic review', ISPRS Journal of Photogrammetry and Remote Sensing. Elsevier B.V., pp. 330–347.
https://doi.org/10.1016/j.isprsjprs.2020.11.019

Chaudhry, M.H. et al. (2021) 'Assessment of dsm based on radiometric transformation of uav data', Sensors, 21(5), pp. 1–19.
https://doi.org/10.3390/s21051649

Che, T. et al. (2008) 'Snow depth derived from passive microwave remote-sensing data in China', Annals of Glaciology, 49, pp. 145–154.
https://doi.org/10.3189/172756408787814690

D'allestro, P. and Parente, C. (2015) GIS application for NDVI calculation using Landsat 8 OLI images, International Journal of Applied Engineering Research.

Deems, J.S., Painter, T.H. and Finnegan, D.C. (2013) 'Lidar measurement of snow depth: A review', Journal of Glaciology, pp. 467–479.
https://doi.org/10.3189/2013JoG12J154

Dietz, A.J. et al. (2012) 'Remote sensing of snow - a review of available methods', International Journal of Remote Sensing. Taylor and Francis Ltd., pp. 4094–4134.
https://doi.org/10.1080/01431161.2011.640964

Drusch, M. et al. (2012) 'Sentinel-2: ESA's Optical High-Resolution Mission for GMES Operational Services', Remote Sensing of Environment, 120, pp. 25–36.
https://doi.org/10.1016/j.rse.2011.11.026

Fawcett, D., Bennie, J. and Anderson, K. (2021) 'Monitoring spring phenology of individual tree crowns using drone-acquired NDVI data', Remote Sensing in Ecology and Conservation, 7(2), pp. 227–244.
https://doi.org/10.1002/rse2.184

Forlani, G. et al. (2018) 'Quality assessment of DSMs produced from UAV flights georeferenced with on-board RTK positioning', Remote Sensing, 10(2).
https://doi.org/10.3390/rs10020311

Frazier, A.E. and Hemingway, B.L. (2021) 'A technical review of planet smallsat data: Practical considerations for processing and using planetscope imagery', Remote Sensing, 13(19).
https://doi.org/10.3390/rs13193930

Gehrmann, F. et al. (2017) 'Phenological responses to small-scale spatial variation in snowmelt timing reveal compensatory and conservative strategies in subarctic-alpine plants', Plant Ecology and Diversity, 10(5–6), pp. 453–468.
https://doi.org/10.1080/17550874.2018.1428693

Giacona, F. et al. (2021) 'Upslope migration of snow avalanches in a warming climate', Proceedings of the National Academy of Sciences, 118(44).
https://doi.org/10.1073/pnas.2107306118/-/DCSupplemental

Gómez-Mendoza, L. et al. (2008) 'Assessing onset and length of greening period in six vegetation types in Oaxaca, Mexico, using NDVI-precipitation relationships', International Journal of Biometeorology, 52(6), pp. 511–520.
https://doi.org/10.1007/s00484-008-0147-6

Hall, D.K. and Riggs, G.A. (2011) 'Normalized-difference snow index (NDSI)', Encyclopedia of snow, ice and glaciers, pp. 779–780.

Harder, P. et al. (2016) 'Accuracy of snow depth estimation in mountain and prairie environments by an unmanned aerial vehicle', The Cryosphere, 10(6), pp. 2559–2571.
https://doi.org/10.5194/tc-10-2559-2016

Helfenstein, I.S. et al. (2022) 'Assessing biodiversity from space: Impact of spatial and spectral resolution on trait-based functional diversity', Remote Sensing of Environment, 275.
https://doi.org/10.1016/j.rse.2022.113024

Henebry, G.M. and De Beurs, K.M. (2013) 'Remote sensing of land surface phenology: A prospectus', in Phenology: An Integrative Environmental Science. Springer Netherlands, pp. 385–411.
https://doi.org/10.1007/978-94-007-6925-0_21

Hervás, J. (2003) 'Recommendations to Deal with Snow Avalanches in Europe', European Commission Joint Research Centre [Preprint].

Horler, D.N.H., Dockray, M. and Barber, J. (1983) 'The red edge of plant leaf reflectance', International Journal of Remote Sensing, 4(2), pp. 273–288.
https://doi.org/10.1080/01431168308948546

Huang, S. et al. (2021) 'A commentary review on the use of normalized difference vegetation index (NDVI) in the era of popular remote sensing', Journal of Forestry Research. Northeast Forestry University.
https://doi.org/10.1007/s11676-020-01155-1

Inglada, J. et al. (2016) 'Improved early crop type identification by joint use of high temporal resolution sar and optical image time series', Remote Sensing, 8(5).
https://doi.org/10.3390/rs8050362

Jiménez-Jiménez, S.I. et al. (2021) 'Digital terrain models generated with low-cost UAV photogrammetry: Methodology and accuracy', ISPRS International Journal of Geo-Information, 10(5).
https://doi.org/10.3390/ijgi10050285

Jones, H.G. (1999) 'The ecology of snow-covered systems: A brief overview of nutrient cycling and life in the cold', Hydrological Processes, 13(14–15), pp. 2135–2147.
https://doi.org/10.1002/(sici)1099-1085(199910)13:14/15<2135::aid-hyp862>3.0.co;2-y

Julien, Y. and Sobrino, J.A. (2009) 'Global land surface phenology trends from GIMMS database', International Journal of Remote Sensing, 30(13), pp. 3495–3513.
https://doi.org/10.1080/01431160802562255

Kappen, L. (1993) Plant Activity under Snow and Ice, with Particular Reference to Lichens.

Kaufmann, R.K. et al. (2003) 'The effect of vegetation on surface temperature: A statistical analysis of NDVI and climate data', Geophysical Research Letters, 30(22).
https://doi.org/10.1029/2003GL018251

Kern, S. and Ozsoy-Çiçek, B. (2016) 'Satellite remote sensing of snow depth on Antarctic sea ice: An inter-comparison of two empirical approaches', Remote Sensing, 8(6).
https://doi.org/10.3390/rs8060450

Lendzioch, T., Langhammer, J. and Jenicek, M. (2019) 'Estimating snow depth and leaf area index based on UAV digital photogrammetry', Sensors, 19(5).
https://doi.org/10.3390/s19051027

Li, Y. et al. (2018) 'Evaluation of Sentinel-2A Surface Reflectance Derived Using Sen2Cor in North America', IEEE Journal of Selected Topics in Applied Earth Observations and Remote Sensing, 11(6), pp. 1997–2021.
https://doi.org/10.1109/JSTARS.2018.2835823

Mahajan, U. and Bundel, R.B. (2016) Drones for Normalized Difference Vegetation Index (NDVI), to Estimate Crop Health for Precision Agriculture: A Cheaper Alternative for Spatial Satellite Sensors.

Main-Knorn, M. et al. (2017) 'Sen2Cor for Sentinel-2', in. SPIE-Intl Soc Optical Eng, p. 3.
https://doi.org/10.1117/12.2278218

Martínez-Carricondo, P. et al. (2018) 'Assessment of UAV-photogrammetric mapping accuracy based on variation of ground control points', International Journal of Applied Earth Observation and Geoinformation, 72, pp. 1–10.
https://doi.org/10.1016/j.jag.2018.05.015

Masek, J.G. et al. (2020) 'Landsat 9: Empowering open science and applications through continuity', Remote Sensing of Environment, 248.
https://doi.org/10.1016/j.rse.2020.111968

Meneses-Tovar, C.L. (2011) 'NDVI as indicator of degradation.', Unasylva, 62(238), pp. 39–46.

Misra, G., Cawkwell, F. and Wingler, A. (2020) 'Status of phenological research using sentinel-2 data: A review', Remote Sensing, 12(17).
https://doi.org/10.3390/RS12172760

Nguyen, Q.L. et al. (2020) 'Flight Height of UAV and Its Influence on the Precise Digital Elevation Model of Complex Terrain', Inzynieria Mineralna, 2020(1), pp. 179–186.
https://doi.org/10.29227/IM-2020-01-27

Notti, D. et al. (2018) 'Potential and limitations of open satellite data for flood mapping', Remote Sensing, 10(11). https://doi.org/10.3390/rs10111673

Orengo, H.A. et al. (2021) 'New developments in drone-based automated surface survey: Towards a functional and effective survey system', Archaeological Prospection, 28(4), pp. 519–526. https://doi.org/10.1002/arp.1822

Peshawa, J.M.A. and Rezhna, H.F. (2014) Data Normalization and Standardization: A Technical Report, Machine Learning Technical Reports. https://docs.google.com/document/d/1x0A1nUz1WWtMCZb5oVzF0SVMY7a_58KQulqQVT8LaVA/edit#

Phiri, D. et al. (2020) 'Sentinel-2 data for land cover/use mapping: A review', Remote Sensing. MDPI AG. https://doi.org/10.3390/rs12142291

Piao, S. et al. (2019) 'Plant phenology and global climate change: Current progresses and challenges', Global Change Biology. Blackwell Publishing Ltd, pp. 1922–1940. https://doi.org/10.1111/gcb.14619

Planet Team (2022) 'Planet imagery product specifications.', Planet Labs Inc [Preprint].

Poghosyan, A. and Golkar, A. (2017) 'CubeSat evolution: Analyzing CubeSat capabilities for conducting science missions', Progress in Aerospace Sciences. Elsevier Ltd, pp. 59–83. https://doi.org/10.1016/j.paerosci.2016.11.002

Qi, Y. et al. (2021) 'Relationship between vegetation phenology and snow cover changes during 2001–2018 in the Qilian Mountains', Ecological Indicators, 133. https://doi.org/10.1016/j.ecolind.2021.108351.

Qiao, C. et al. (2021) 'Vegetation phenology in the Qilian mountains and its response to temperature from 1982 to 2014', Remote Sensing, 13(2), pp. 1–20. https://doi.org/10.3390/rs13020286

Raeva, P.L., Šedina, J. and Dlesk, A. (2019) 'Monitoring of crop fields using multispectral and thermal imagery from UAV', European Journal of Remote Sensing, 52(sup1), pp. 192–201. https://doi.org/10.1080/22797254.2018.1527661

Ren, J., Campbell, J.B. and Shao, Y. (2017) 'Estimation of sos and eos for midwestern us corn and soybean crops', Remote Sensing, 9(7). https://doi.org/10.3390/RS9070722

Revuelto, J. et al. (2022) 'Intermediate snowpack melt-out dates guarantee the highest seasonal grasslands greening in the Pyrenees', Scientific Reports, 12(1). https://doi.org/10.1038/s41598-022-22391-x

Richardson, A.D. et al. (2013) 'Climate change, phenology, and phenological control of vegetation feedbacks to the climate system', Agricultural and Forest Meteorology, pp. 156–173. https://doi.org/10.1016/j.agrformet.2012.09.012

Rosnell, T. and Honkavaara, E. (2012) 'Point cloud generation from aerial image data acquired by a quadrocopter type micro unmanned aerial vehicle and a digital still camera', Sensors, 12(1), pp. 453–480. https://doi.org/10.3390/s120100453

Schuster, C., Förster, M. and Kleinschmit, B. (2012) 'Testing the red edge channel for improving land-use classifications based on high-resolution multi-spectral satellite data', International Journal of Remote Sensing, 33(17), pp. 5583–5599. https://doi.org/10.1080/01431161.2012.666812

Shoab, M., Singh, V.K. and Ravibabu, M. V. (2022) 'High-Precise True Digital Orthoimage Generation and Accuracy Assessment based on UAV Images', Journal of the Indian Society of Remote Sensing, 50(4), pp. 613–622. https://doi.org/10.1007/s12524-021-01364-z

Singh, D. and Singh, B. (2020) 'Investigating the impact of data normalization on classification performance', Applied Soft Computing, 97. https://doi.org/10.1016/j.asoc.2019.105524

Singh, D. and Singh, B. (2022) 'Feature wise normalization: An effective way of normalizing data', Pattern Recognition, 122. https://doi.org/10.1016/j.patcog.2021.108307

Taddia, Y., Stecchi, F. and Pellegrinelli, A. (2019) 'Using dji phantom 4 rtk drone for topographic mapping of coastal areas', in International Archives of the Photogrammetry, Remote Sensing and Spatial Information Sciences - ISPRS Archives. International Society for Photogrammetry and Remote Sensing, pp. 625–630. https://doi.org/10.5194/isprs-archives-XLII-2-W13-625-2019

Tan, B. et al. (2011) 'An Enhanced TIMESAT Algorithm for Estimating Vegetation Phenology Metrics From MODIS Data', IEEE Journal of Selected Topics in Applied Earth Observations and Remote Sensing, 4(2), pp. 361–371. https://doi.org/10.1109/JSTARS.2010.2075916

Teich, M. et al. (2014) 'Computational snow avalanche simulation in forested terrain', Natural Hazards and Earth System Sciences, 14(8), pp. 2233–2248. https://doi.org/10.5194/nhess-14-2233-2014

Tsai, Y.L.S. et al. (2019) 'Remote sensing of snow cover using spaceborne SAR: A review', Remote Sensing. MDPI AG. https://doi.org/10.3390/rs11121456

Tsai, Y.-L.S. et al. (2019) 'Wet and Dry Snow Detection Using Sentinel-1 SAR Data for Mountainous Areas with a Machine Learning Technique', Remote Sensing, 11(8). https://doi.org/10.3390/rs11080895

Tu, Y.H. et al. (2022) 'The radiometric accuracy of the 8-band multi-spectral surface reflectance from the planet SuperDove constellation', International Journal of Applied Earth Observation and Geoinformation, 114. https://doi.org/10.1016/j.jag.2022.103035

Um, I. et al. (2020) 'Configuring RTK-GPS Architecture for System Redundancy in Multi-Drone Operations', IEEE Access, 8, pp. 76228–76242. https://doi.org/10.1109/ACCESS.2020.2989276

USGS (2013) 'Landsat 8: U.S. Geological Survey Fact Sheet 2013–3060'. http://earthexplorer.usgs.gov

Vaiopoulos, A.D. and Karantzalos, K. (2016) 'Pansharpening on the narrow VNIR and SWIR spectral bands of Sentinel-2', in International Archives of the Photogrammetry, Remote Sensing and Spatial Information Sciences - ISPRS Archives. International Society for Photogrammetry and Remote Sensing, pp. 723–730. https://doi.org/10.5194/isprsarchives-XLI-B7-723-2016

Van Valen, L. (1975) 'Life, Death, and Energy of a Tree', in Biotropica, pp. 259-269.

Vorobiova, N. and Chernov, A. (2017) 'Curve fitting of MODIS NDVI time series in the task of early crops identification by satellite images', in Procedia Engineering. Elsevier Ltd, pp. 184–195. https://doi.org/10.1016/j.proeng.2017.09.596

Wang, G. et al. (2022) ‘Characterization of NDSI Variation: Implications for Snow Cover Mapping’, IEEE Transactions on Geoscience and Remote Sensing, 60.
https://doi.org/10.1109/TGRS.2022.3165986

Wang, H., Dai, J. and Ge, Q. (2014) ‘Comparison of satellite and ground-based phenology in China’s temperate monsoon area’, Advances in Meteorology, 2014.
https://doi.org/10.1155/2014/474876

Wang, Q. et al. (2016) ‘Fusion of Sentinel-2 images’, Remote Sensing of Environment, 187, pp. 241–252.
https://doi.org/10.1016/j.rse.2016.10.030

Wicaksono, P. et al. (2023) ‘Seagrass ecosystem biodiversity mapping in part of Rote Island using multi-generation PlanetScope imagery’, Carbon Footprints, 2(4).
https://doi.org/10.20517/cf.2023.9

Woodcock, C.E. and Strahler, A.H. (1987) The Factor of Scale in Remote Sensing, REMOTE SENSING OF ENVIRONMENT.

Xu, N. et al. (2019) ‘Analysis of vegetation red edge with different illuminated/shaded canopy proportions and to construct normalized difference canopy shadow index’, Remote Sensing, 11(10).
https://doi.org/10.3390/rs11101192

Yang, X. et al. (2012) ‘Regional-scale phenology modeling based on meteorological records and remote sensing observations’, Journal of Geophysical Research: Biogeosciences, 117(3).
https://doi.org/10.1029/2012JG001977

Yu, J.J. et al. (2020) ‘Determining the optimal number of ground control points for varying study sites through accuracy evaluation of unmanned aerial system-based 3d point clouds and digital surface models’, Drones, 4(3), pp. 1–19.
https://doi.org/10.3390/drones4030049

Yunfei, B. et al. (2008) ‘Classification of LIDAR point cloud and generation of DTM from LIDAR height and intensity data in forested area’, The International Archives of the Photogrammetry, Remote Sensing and Spatial Information Sciences [Preprint].

Zanaga, D. et al. (2022) ‘ESA WorldCover 10 m 2021 v200’.
https://doi.org/10.5281/ZENODO.7254221

Zeng, H. and Jia, G. (2013) ‘Impacts of snow cover on vegetation phenology in the arctic from satellite data’, Advances in Atmospheric Sciences, 30(5), pp. 1421–1432.
https://doi.org/10.1007/s00376-012-2173-x

Zhang, X. et al. (2002) Monitoring vegetation phenology using MODIS.

11.1. Table of figures

12. Appendix

A. Fitting of NDVI time series of Sentinel-2 and SuperDove. The 9 Planet pixels cover approximately the same area as the Sentinel-2 one.

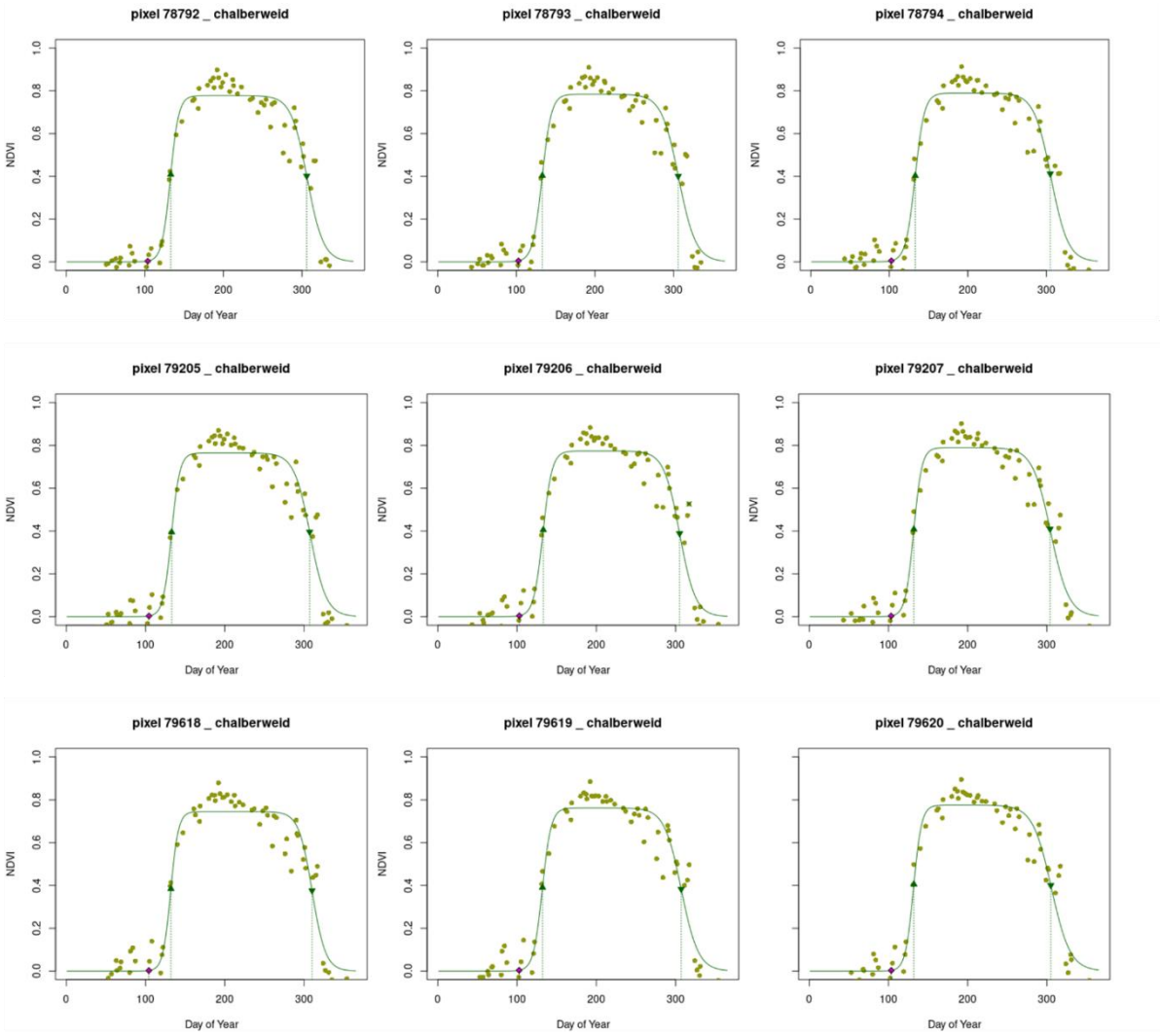

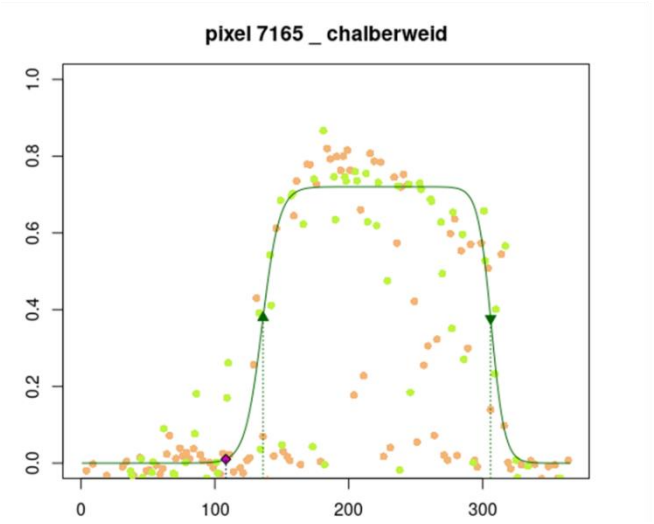

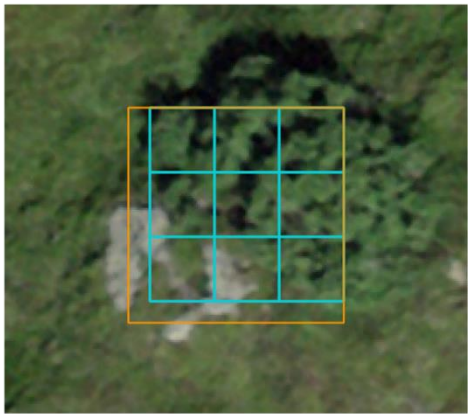

B. From top left to bottom right: Average Normalized Start of Deflection map for Sentinel-2 and SuperDove. Average Normalized snow melt map for Sentinel-2 and SuperDove. Average Normalized RGB drone melt map. Multispectral drone snow depth map.

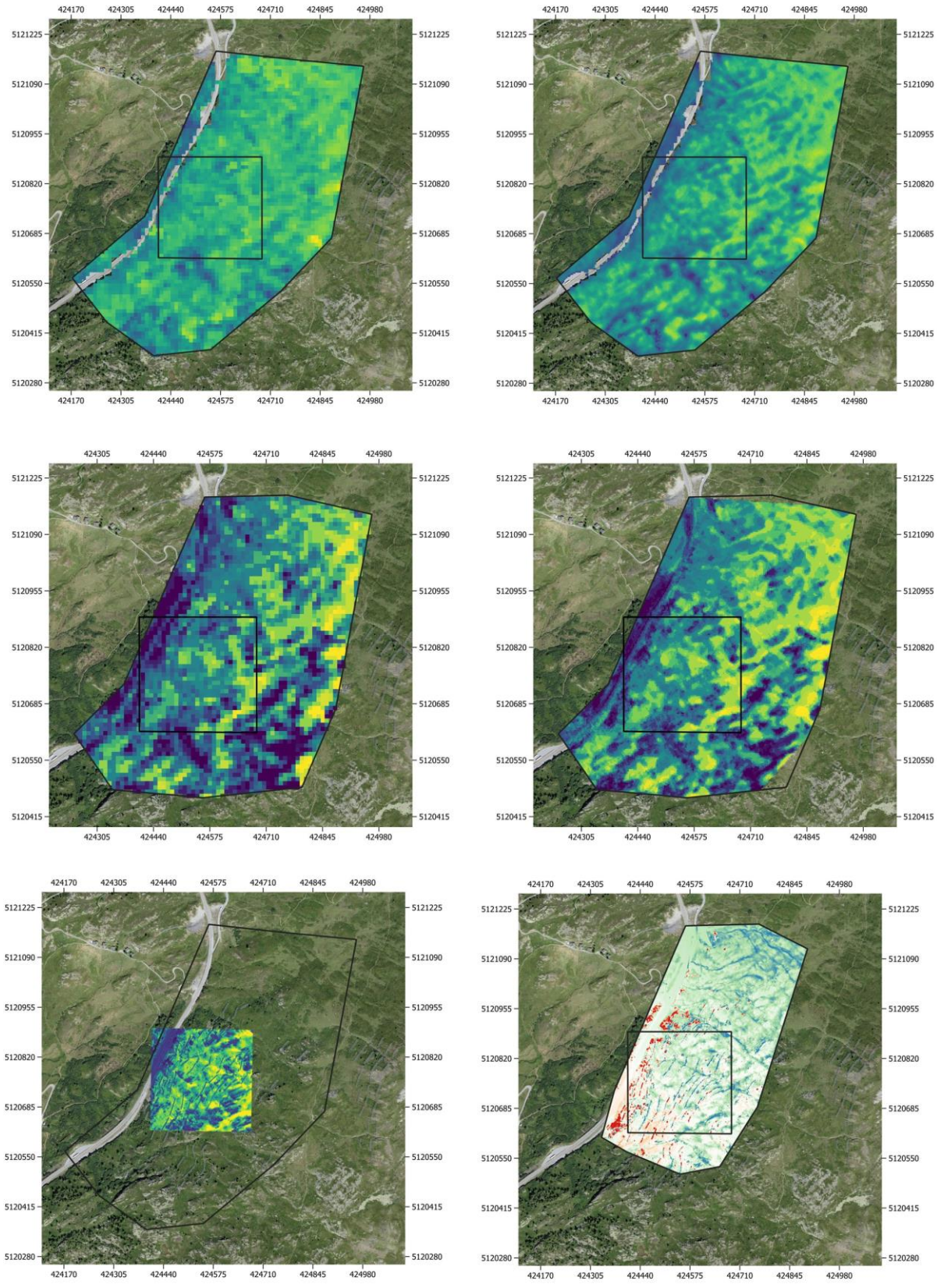

13. Personal declaration

“I hereby declare that the submitted thesis is the result of my own, independent work. All external sources are explicitly acknowledged in the Thesis”

Zürich, 30.01.2024